Mechanism of transcranial focused ultrasound regulating the neuronal activity of the retrosplenial cortex

Cheng Wu

Thesis submitted for the degree of Doctor of Philosophy

University of Edinburgh

2022

Declaration

I declare that the dissertation submitted is my research work and research results under the guidance of my supervisor. The paper does not contain research published or written by others and does not contain material used for degrees or certificates in educational institutions, except where it is expressly noted and acknowledged. My colleagues' contribution to this research has been clearly stated and acknowledged in the paper.

Cheng Wu
2022

Acknowledgements

This thesis is completed under the careful guidance of my supervisors, Prof. Xiang-Yao Li and Prof. John Menzies. In the past seven years (starting from my senior year in college), they have set an excellent example for me. Their love and dedication to scientific research have made me admire them for a lifetime. When I encounter difficulties, they are always very kind to encourage me, tell me not to give up, and solve one problem after another with me. Thanks to my thesis committee chair Prof. Mike Shipston, he gives me lots of precious suggestions on my project and thesis.

I want to thank Dr. Li Liu, who has given me much help in daily life and scientific research. She often takes her rest time to guide my experiments without any complaints. Thanks to Dr. Yong-Jie Wang, who encouraged us and told us to analyze the reasons and solve the problems when we encountered difficulties. There is another goddess that I want to thank most that is Dr. Li Sun. She is like a sister to us. After entering postgraduate school, Dr. Sun teaches me to do experiments with patience. She is very lively and enthusiastic about both scientific research and life. She often cooks a big meal at home and invites us to have dinner. I feel like I am back home.

Thanks to Jing-Hua Wang. We make progress together and always support each other. Thanks to Yan-Na Lian, Yun-Ya Qiu, Li-Zhen Xu, Xiao-Wen Cao, Shu-Xia Zhang, Du Zheng, Xian-Yi Lin, Xiang-Yang Mei, Chao-Jin Huang, Zi-Yue Wang, Wen-Dong Zhang, and Tao Sheng. Thanks for your help in my study and life.

Finally, I want to thank my family for their support, which has helped me get to where I am today. My parents are the dignitaries in my life; they always encourage and support me. No matter what decisions I make, they always believe in me.

I want to express my sincere thanks to all the experts who reviewed and defended the thesis.

Abstract

Non-invasive neuromodulation is crucial in fundamental research and clinical treatment. Among those non-invasive neuromodulations, transcranial focused ultrasound (tFUS) can penetrate the skull to focus energy on a specific brain region, temporarily affecting brain function. Compared with traditional neuromodulation methods, such as transcranial direct current stimulation and transcranial magnetic stimulation, tFUS has become a novel method for regulating neuronal activity by means of its non-invasion, reversibility, and accuracy. However, how tFUS regulates neuronal activity and cellular properties in response to tFUS remains unknown.

To investigate how tFUS regulates neuronal activity, I used behavioural tests, real-time fluorescence quantitative polymerase chain reaction, immunofluorescent staining, chemical genetics, and multi-channel in vivo recording to explore whether tFUS affected neuronal activity in the pain-related brain region, retrosplenial cortex (RSC). Moreover, tFUS significantly increased paw withdrawal threshold (PWT) and prolonged thermal withdrawal latency (TWL) both in naïve and neuropathic mice. tFUS also significantly increased mRNA and protein expression levels of early growth factor response 1 (Egr1). These tFUS-activated Egr1 cells were mainly neurons. Through multi-channel in vivo recording, it was found that the spike rate of pyramidal neurons and interneurons decreased remarkably under tFUS. A greater proportion of spike rate in pyramidal neurons and interneurons showed a decrease rather than an increase in activity after tFUS.

Subsequently, Egr1 positive cells activated by tFUS were specifically inhibited by the targeted recombination in the active population system (TRAP), and then the effect of tFUS on PWT and TWL was inhibited. These results suggested that Egr1 was an essential marker of tFUS responsive neurons in RSC. Subsequently, I performed transcriptome sequencing based on Egr1-GFP cells activated by tFUS. Transient receptor potential cation channel subfamily C member 4 (Trpc4) was selected according to the transcriptome sequencing data. Combined with calcium imaging, patch-clamp recording, and short hairpin ribonucleic acid (shRNA) interference, it was found that tFUS could activate Trpc4, which could be blocked by ML204, an inhibitor of Trpc4. In vivo, with specific inhibition of Trpc4 expression in RSC, the proportion of decreased neuronal activity induced by tFUS was significantly down-regulated. At the same time, the regulation of PWT and TWL by tFUS was also inhibited. The above results showed that Trpc4 was an important factor in regulating Egr1 response to tFUS, thus regulating RSC and further regulating the somatosensory threshold of mice.

To further explore the characteristics of tFUS responsive cells, I used single-cell RNA sequencing (scRNA-seq) to map the single-cell transcriptome expression of RSC. It was also identified tFUS-induced cell type-dependent transcriptome and functional changes in RSC. Subsequently, *Egr1* was used as a marker to identify tFUS-activated cell types and populations. Then, it was found that *Egr1* was highly expressed in neurons, endothelial cells (EC), and vascular smooth muscle cells (vSMC). These cells acted as tFUS-sensitive cells. Further analysis of cellular communication pathways between tFUS-sensitive cells and other cells revealed multiple signal pathways, which suggested that tFUS-

sensitive cells received or transmitted information to other cell types, causing changes in the transcriptome.

In conclusion, this study found that Trpc4 was a key factor regulating Egr1 response to tFUS. In addition, it provided transcriptome expression atlas and cellular communication pathways of tFUS-sensitive cells by scRNA-seq. These results provided a basis for the cellular and molecular mechanisms of tFUS neuromodulation, which supported ultrasonic neuromodulation in basic neuroscience research and clinical applications.

Keywords: tFUS, RSC, scRNA-seq, Egr1, Trpc4

Lay summary

Transcranial focused ultrasound (tFUS) can penetrate the skull and focus energy on specific brain regions, temporarily affecting brain function. Therefore, tFUS is a novel approach to regulating neuronal activity by being a non-invasive, reversible, and accurate neuromodulation approach. However, how tFUS regulates neuronal activity and cell properties in response to tFUS remains unclear.

To investigate how tFUS regulates neuronal activity, I used different experimental methods to investigate whether tFUS affects neuronal activity in a brain region associated with pain, the retrosplenial cortex (RSC). tFUS significantly increased pain threshold both in naïve and neuropathic pain mice. The early growth factor response 1 (Egr1) mRNA and protein expression levels were also increased. The Egr1 cells activated by tFUS were mainly neurons. It was also found that pyramidal neurons and interneurons' activity decreased remarkably under tFUS. A greater proportion of spike rate in pyramidal neurons and interneurons showed a decrease rather than an increase in activity after tFUS.

Then, tFUS-activated Egr1-positive cells were specifically inhibited, inhibiting the effect of tFUS on the pain threshold. These results suggest that Egr1 was an important marker of tFUS response neurons. Subsequently, transcriptome sequencing was performed based on tFUS-activated Egr1-GFP cells. The transient receptor potential cationic channel C member 4 (Trpc4) was selected based on transcriptome sequencing data. It was found that tFUS activates Trpc4, blocked by ML204, an inhibitor of Trpc4. In vivo, by specifically inhibiting Trpc4 expression in RSC, the tFUS-induced effects on neurons were significantly down-regulated. tFUS also inhibited the regulation of the pain threshold. These results suggest that Trpc4 is a critical factor in regulating the tFUS response of Egr1, RSC, and thus sensory threshold in mice.

To further explore the characteristics of tFUS reactive cells, I mapped the single-cell transcriptome expression of RSC. It was also found that cell type-dependent transcriptome and functional changes in tFUS-induced RSC. Subsequently, Egr1 was used as a marker to identify tFUS-activated cell types and populations. Then, it was found that Egr1 was highly expressed in different cell types. These cells acted as tFUS-sensitive cells. It was further found that tFUS sensitive cells received or transmitted information to other cells by analyzing cell-to-cell communication between tFUS sensitive and insensitive cells, leading to changes in the transcriptome.

All in all, this study proposed that Egr1 was a critical molecular marker in response to tFUS. It was found that Trpc4 was a key factor regulating Egr1 response to tFUS. In addition, I provided a transcriptome expression atlas and cellular communication pathways of tFUS-sensitive cells. These results provided a basis for the cellular and molecular mechanisms of tFUS neuromodulation, which supported ultrasonic neuromodulation in basic neuroscience research and clinical applications.

List of abbreviations

Abbreviation	Full name
AAV	Adeno-associated virus
Astro	Astrocyte
ACSF	Artificial cerebrospinal flud
AMPAR	Amino-3-hydroxy-5-methyl-4-isoxazolepropionic acid receptor
ACC	Anterior cingulate cortex
AP	Anteroposterior
AP^2	Action potential
AW	Action wave
BP	Biological process
BBB	Blood-brain barrier
BDNF	Brain-derived neurotrophic factor
CPN	Common peroneal nerve ligation
CNO	Clozapine N-oxide
Cre	Cyclization recombination enzyme
CC	Cellular component
CIB	Calcium imaging buffer
COP	Differentiation-committed oligodendrocyte precursor
Cdh23	B6 (v)-cdh23v-2J/J
Cre	Cyclization recombination enzyme
Ctrl	Control
DRG	Dorsal root ganglion
DEG	Differentially expressed gene

DV	Dorsoventral
EEG	Electroencephalogram
Egr1	Early growth response 1
EPM	Elevated plus-maze
EC	Endothelial cell
EMG	Electromyography
FMRI	Functional magnetic resonance imaging
GO	Gene Ontology
GABA	Gamma-aminobutyric acid
Gabra1	Gamma-aminobutyric acid type A receptor alpha1 subunit
GFP	Green fluorescent protein
HIFU	High-intensity focused ultrasound
IC_{50}	Half maximal inhibitory concentration
INS	Infrared neural stimulation
IN	Interneuron
IEG	Immediate-early gene
IP.	Intraperitoneal injection
I_{SPTA}	Spatial-peak, temporal-averaged intensity
KD	Knock down
LFP	Local field potential
LoxP	Locus of X-over P1
Mac	Macrophage
MC	Microglia cluster
ML	Mediolateral

MOL	Mature oligodendrocyte
MF	Molecular function
M1	Primary motor cortex
M2	Secondary motor cortex
NFOL	Newly formed oligodendrocyte
Neu	Neuron
NeuN	Neuronal nuclei
NOR	Novel object recognition
OFT	Open-field test
OPC	Oligodendrocyte precursor cell
Oligo	Oligodendrocyte
Peri/Pcy	Pericyte
PCA	Principal component analysis
PN	Pyramidal neuron
PWT	Paw withdrawal threshold
qPCR	Real-time fluorescence quantitative polymerase chain reaction
RSC	Retrosplenial cortex
scRNA-seq	Single-cell RNA sequencing
SEA	Singular enrichment analysis
S.E.M.	Standard error of the mean
shRNA	Short hairpin ribonucleic acid
SingleR	Single-cell recognition of cell types
SPF	Specific pathogen Free
tFUS	Transcranial focused ultrasound
t-SNE	*t*-Distributed stochastic neighbour

	embedding
TWL	Thermal withdrawal latency
TRAP	Targeted recombination in the active population
Trpc4	Transient receptor potential cation channel subfamily C member 4
UCA	Ultrasound contrast agent
UMIs	Unique molecular identifiers
UMAP	Uniform manifold approximation and projection
vSMC	Vascular smooth muscle cell
WT	Wild type
4-TM	4-Hydroxytamoxifen

Contents

Chapter 1 Introduction

Ultrasound is a sound pressure wave whose frequency exceeds the range of human hearing. Focused ultrasound (FUS) is a non-invasive way to deliver mechanical force to cells through sound pressure waves. Depending on specific pulse parameters, it can lead to various biological effects, including thermal and mechanical effects (Haar, 2009). FUS can focus on solid structures. Moreover, it transmits over a long distance with minimal loss in soft biological tissue (O'Brien, 2007), and its spatial resolution is equivalent to the wavelength of the driving frequency. Since the focus is achieved through the phase length interference of incident waves, the focus can be formed inside the tissue without affecting the cells close to the ultrasonic probe in the propagation path.

In the 1950s, high-intensity focused ultrasound (HIFU) was first used to treat brain disease (W. J. FRY et al., 1955). This method has been applied in the clinical treatment of various neurological diseases. Using HIFU to target tissues, symptoms were significantly improved in chronic pain, brain tumours, movement disorders, and psychiatric diseases (Legon et al., 2014; Martin et al., 2014; T. R. Wang et al., 2015). regions (Airan et al., 2017).

Compared with HIFU, transcranial-focused ultrasound (tFUS) can penetrate the skull and focus on specific brain regions to regulate neuronal activity (Baek et al., 2017; Fini & Tyler, 2017; Khraiche et al., 2008; Tufail et al., 2010). In recent years, neuromodulation methods mainly include deep brain stimulation (DBS), transcranial magnetic stimulation (TMS), and transcranial direct current stimulation (tDCS), which have been widely used in the clinical treatment of various brain diseases, including tremor, depression, epilepsy, schizophrenia, pain and tinnitus (Hallett, 2000; Nitsche et al., 2008; Perlmutter & Mink, 2006). However, deep brain stimulation and other invasive methods require high-risk surgery and high cost; transcranial stimulation, tDCS, and other non-invasive stimulation methods often fail to activate the target brain region accurately. The emergence of tFUS has primarily solved the above problems. This method has been gradually used to study neural regulation in rodents, non-human primates, and humans.

In order to know more about ultrasonic neuromodulation, this review mainly focuses on the background and prospects of ultrasonic neuromodulation.

1.1 Development of ultrasonic neuromodulation

The research on nervous system regulation by ultrasound can be traced back to 1929. When ultrasound was passed through the salt solution, it could make the heart and leg muscles of isolated frogs contract in the solution, which was also the earliest proof that ultrasonic stimulation could affect the activity of nerve cells (Harvey, 1929). Then, in 1958, ultrasound stimulated the lateral geniculate nucleus in cats, which could affect neural activity responding to light (F. J. FRY et al., 1958). These studies suggest that ultrasound can influence the activity of neurons. Subsequently, many studies have found that ultrasonic stimulation can affect compound action potential and field potential (Bachtold et al., 1998; Mihran et al., 1990; Tsui et al., 2005). The above research shows that ultrasonic stimulation can affect electrophysiological activity but does not prove whether ultrasound can directly stimulate neurons or trigger an action potential.

Until half a century later, it was found that ultrasound could cause nerve impulses by activating sodium and calcium ion channels (Tyler et al., 2008), which is the first demonstration that ultrasound directly stimulates action potentials and synaptic transmission in the brain circuits. Then, pulsed ultrasound was used for transcranial stimulation. For example, the rodents' thalamus (*Transcranial focused ultrasound to the thalamus is associated with reduced extracellular GABA levels in rats.*, 2012), activity of neural circuits in the hippocampus (Scarcelli et al., 2014), locomotor somatosensory and visual cortexes in rabbits (S.-S. Yoo et al., 2011), the primary motor somatosensory and primary visual cortexes of sheep (W. Lee, Lee, et al., 2016), all of which can be activated by tFUS. The cells in the corresponding brain regions can respond to ultrasonic stimulation.

Ultrasonic stimulation has been gradually applied in non-human primates. By stimulating the visual-motor cortex of awake non-human primates, ultrasound changed eye activity (Deffieux et al., 2013). Later, when ultrasound stimulated the monkeys' visual cortex, 40% of the neurons showed marked changes in activity, and a half showed temporary increases in activity (Wattiez et al., 2017).

In addition to the visual cortex, the anterior cingulate cortex was reversibly stimulated by ultrasound, which impaired decision-making processes in macaques (Fouragnan et al., 2019).

Ultrasonic stimulation has also been gradually applied in human experiments. Studies have found that ultrasound acting on the primary visual cortex can control human vision (Nitsche et al., 2008). In addition, the primary somatosensory cortex (Mueller et al., 2014), the primary motor cortex (Legon, Bansal, et al., 2018), prefrontal cortex (Hameroff et al., 2013) and thalamus (Legon, Ai, et al., 2018) were regulated by ultrasound. Thus, the development of ultrasonic neuromodulation is being gradually advanced and will likely become a tool for clinical and basic neuroscience research in the coming years. With the development of ultrasonic neuromodulation, we will be able to target and regulate the activity of neural circuits better non-invasively.

1.2 Ultrasonic neuromodulation in animal studies

1.2.1 Ultrasonic neuromodulation in the central nervous system (CNS)

As early as 1953, there was evidence that ultrasound enhanced the excitability of neural tissue (MAZOUE et al., 1953). On the other hand, when ultrasound was applied to the lateral geniculate nucleus in cats, electrophysiological responses in the primary visual cortex were locally suppressed (F. J. FRY et al., 1958). Shorter ultrasound pulses also had inhibitory effects, including temporary pupil dilation in cats (Ballantine et al., n.d.) and depolarization propagation in rats (Koroleva et al., 1986).

Subsequently, a series of in vitro experiments combined with electrophysiological techniques demonstrated that ultrasound could regulate the activity of neurons. In hippocampal slice experiments, ultrasonic stimulation could change the local field potential (LFP) of nerve fibres, and the effect of ultrasonic pulse in different areas was also different, which had excitatory and inhibitory effects (Mihran et al., 1990; Rinaldi et al., 1991; TAKAGI et al., 1960). Also found in isolated hippocampal slices, ultrasonic stimulation excited neurons and enhanced firing rates (Khraiche et al., 2008). Furthermore, whole-cell current clamp recording showed ultrasound-induced action potential in excitatory neurons, vesicle secretion, and synaptic transmission in hippocampal CA1 (Tyler et al., 2008). In multi-channel recording experiments, ultrasonic stimulation increased the firing activity of hippocampal neurons (Choi et al., 2013; H.-B. Kim et al., 2017).

Ultrasonic stimulation could also produce subcellular responses. Ultrasound triggered sodium and calcium voltage-gated ion channels (Tyler et al., 2008). In the study of Xenopus laevis oocytes, ultrasonic stimulation increased the current carried by the two-pore domain potassium channel and voltage-gated sodium channel (Kubanek et al., 2016). Later in nematode studies, a MEC-4 expression in haptic receptor neurons forms the pore-channel protein subunit was necessary for nematode response to ultrasound (Kubanek et al., 2018).

Piezo1, a mechanically sensitive channel, has also been activated by ultrasonic stimulation of specific parameters(Prieto et al., 2018).

With the technical development of ultrasonic neuromodulation, it has also been applied to in-vivo experiments, further proving the neural regulation effect of ultrasound. In the motor cortex, ultrasonic stimulation could induce neuronal activity, which further caused changes in motor behaviour (Tufail et al., 2010), and tetrodotoxin blocked this activity induced by ultrasound. According to the electromyography (EMG) recording, the motor cortex response was generated with the beginning of ultrasonic stimulation rather than offset by ultrasonic stimulation. The effect of ultrasound was enhanced with the increase of the ultrasonic intensity and duration. The induced motor response was not a phenomenon with or without, which meant that the greater intensity and duration of the stimulus increased the likelihood that the motor response would occur without affecting the duration or intensity of the response (King et al., 2013). Subsequently, studies have explored the neural regulation effects of ultrasound at different frequencies on the motor cortex of mice, both lower and higher than 1 MHz. Meanwhile, it has been found that ultrasound at a frequency of 2.9 MHz could also effectively generate a motor response. It has also been confirmed that ultrasound needed greater intensity to achieve the same effect (P. P. Ye et al., 2016). When ultrasound frequency was up to 5 MHz, the motor cortex could still successfully regulate neurons. Meanwhile, it was found that the stimulation area of 5 MHz was smaller than the stimulation area of 1 MHz, and the adequate time of 5 MHz ultrasonic stimulation was smaller than the adequate time of 1 MHz (G.-F. Li et al., 2016). Ketamine could inhibit this motor response and calcium ions' transient potential in motor cortex neurons induced by ultrasonic stimulation (S. Han et al., 2018).

The somatosensory cortex receives sensory signals from all over the body and neurons sensitive to skin, pain, and visual or auditory stimuli. When the somatosensory motor cortex of rabbits was stimulated by ultrasound, electroencephalogram (EEG) recordings and functional magnetic resonance imaging showed that ultrasound could both stimulate neuronal activity and inhibit it (S.-S. Yoo et al., 2011). When the somatosensory cortex of mice was stimulated by ultrasound, excitatory neurons in the cortex were activated. The effect of ultrasound was consistent with that of optogenetics, but the interneurons were not included (Moore et al., 2015). Subsequently, the duration and spatial distribution of sensory-induced responses in the somatosensory cortex were observed in calcium responses to ultrasound stimulation using voltage-sensitive dyes and GCaMP6f mice (Fisher & Gumenchuk, 2018).

1.2.2 Ultrasonic neuromodulation in the peripheral nervous system (PNS)

The ultrasonic neuromodulation is studied synchronously in the PNS. Similar to the reversible effects of ultrasonic stimulation initially found in the CNS, ultrasound targeting ventral nerves in crayfish in vitro increased the spikes. It subsequently reversibly inhibited the spontaneous activity of the nerves (Fry et al., 1950). Then, ultrasound acting on the myelinated sciatic nerve could inhibit or enhance the compound action potential induced by electrical stimulation (Mihran et al., 1990).

Ultrasound could inhibit the PNS. The axons of earthworms were stimulated in vivo by ultrasound of 825 kHz. When sufficient pulse energy was applied, the function of axons decreased due to a kind of non-cavitation effect of ultrasound, suggesting that the change of permeability through the ion channel may cause this change (Wahab et al., 2012). This ultrasound inhibition of peripheral nerve function was also found in cats' saphenous nerves. Different nerve fibres were inhibited by ultrasound. The C-fibers of the saphenous nerve were the most sensitive and inhibited to the greatest extent; the A-fiber with the largest saphenous nerve was the least sensitive. The inhibition of ultrasound on nerve fibres was reversible, but this effect was irreversible with increased ultrasound intensity (YOUNG & HENNEMAN, 1961). It found that compound muscle action potential (CMAP) decreased with the change of ultrasonic intensity and exposure time in the sciatic nerve of rats stimulated by 5.7 MHz ultrasound, and the amplitude of CAMP returned to the baseline value at 28 days of ultrasonic stimulation. However, in the highest intensity ultrasound stimulation group, CAMP, there was still no recovery amplitude, which proved that the ultrasound stimulation could produce from the biological effects of the partial block to complete block; this showed that the ultrasound can be used as an alternative clinical methods to induce nerve conduction block, also suggested it as a potential new treatment for severe cramps and pain (Foley et al., 2008). Ultrasound also enhances the PNS. Continuous ultrasound could enhance the action potential amplitude, which was still reversible, but eventually presented irreversible inhibition (Lele, 1963). Action potentials of 0.1-4.2 W/cm^2 were induced by ultrasound on the skin touch, pressure, and vibration receptors in cats, and the receptors' potential increased with the enhancement of ultrasound intensity. The same phenomenon was also found in the auditory vagus nerve of frogs (Leonid R Gavrilov et al., 1977).

Ultrasound can treat diseases in PNS. Muscle contractions were observed when the mice were sonically stimulated between the sciatic nerves and after stimulation. After the sciatic nerve was severed, the downstream effect of ultrasonic stimulation disappeared (Downs et al., 2018). After the sciatic nerve was severed, the expression of BDNF mRNA was higher than that of the control group by ultrasound treatment, promoting nerve regeneration and functional recovery after peripheral nerve compression injury (Downs et al., 2018).

In summary, ultrasound stimulation could be used as a targeted, safe, and non-invasive alternative to conventional PNS stimulation for the clinical treatment of peripheral nerve diseases.

1.3 Ultrasonic neuromodulation progress in human trials

Ultrasonic neuromodulation has been used in human studies. Ultrasound is different from other stimuli, such as thermal, mechanical, and electrical stimulation, as when ultrasound acts on the surface or deep tissue, which can induce a change of feeling. The ultrasonic depth and volume stimulation are controlled by changing the ultrasonic focus and carrier frequency so that ultrasound can produce the effect in small volume tissue. It leads to precise and focused energy deposition and relatively specific induction of feeling (Dickey et al., 2012). Sensations of touch, heat, cold, itch, and pain have been induced by different parameters of ultrasound (L. Gavrilov, 2008; L R Gavrilov et al., 1996). Studies on ultrasound neuromodulation gradually increase in human PNS and CNS.

Ultrasound can modulate the PNS in human beings. Ultrasound acting on human hands' median nerve, ulnar nerve, and radial nerve, the sensation of fingers, palms, and forearms were detected. With the increase of ultrasonic intensity, subjects' tactile sensation changed, then changed temperature perception, and finally induced pain sensation. It was seen that different parameters of ultrasonic stimulation could produce different peripheral sensory changes, but continuous ultrasound could not induce peripheral somatosensory changes; only pulse ultrasound could induce those changes (Leonid R Gavrilov et al., 1977; W. Lee et al., 2014). Subsequently, the S-shaped response rate curve was presented with the increase in ultrasonic intensity, and the subjects' response was correlated with the density of mechanical receptors. Like other ways of neuromodulation, ultrasound stimulation of human fingertips could also induce action potentials and observe the changes in blood oxygen saturation levels (Legon et al., 2012). These findings suggested that focused ultrasound may provide a new approach for the study and diagnosis of peripheral nerve injury, dysfunction, and disease.

With the technical development of ultrasonic stimulation, it has also been used in the CNS of humans. When focused ultrasound stimulated the posterior frontal cortex of chronic pain patients, the subjective mood of patients was improved, and the pain symptoms were improved but not very significant (Hameroff et al., 2013). In the human primary sensory cortex, somatosensory evoked potential and EEG changed with ultrasonic regulation (H. Kim et al., 2015; Mueller et al., 2014). Later, the optical illusion perception changed after ultrasonic stimulation in the human primary visual cortex. Functional magnetic resonance imaging illustrated that the primary visual cortex's visual pathways and cognitive processes were activated, and the visual evoked potentials were regulated (W. Lee, Kim, et al., 2016). In addition, both the thalamus (Legon, Ai, et al., 2018) and primary motor cortex (Legon, Bansal, et al., 2018) were regulated by ultrasound to cause the activities of corresponding brain regions and change behaviour.

Ultrasonic stimulation has a safe neurophysiological effect on brain function and is a promising non-invasive therapy for regulating conscious and unconscious mental states and disorders in humans.

1. Introduction

The study of ultrasonic neuromodulation dates back to 1929, when ultrasound passed through a salt solution, and the muscle nerve fibres of isolated frogs were excited in the solution (Harvey, 1929). The first time ultrasound was used to cauterize brain tissue in the 1950s (W. J. FRY et al., 1955); this type of treatment, also known as high-intensity focused ultrasound (HIFU) technology, has been used in the clinical treatment of a variety of neurological diseases, such as chronic pain, essential tremor, dystonia, and brain tumours, which could significantly relieve symptoms (Legon et al., 2014; Martin et al., 2014; T. R. Wang et al., 2015).

In addition, low-intensity focused ultrasound combined with an ultrasound contrast agent (UCA) could open the blood-brain barrier (BBB) and be used for local delivery of drugs to the brain (Hynynen et al., 2005), which was used to treat Parkinson's disease (PD) (Gasca-Salas et al., 2021), Alzheimer's disease (AD) (Lipsman et al., 2018) and amyotrophic lateral sclerosis (ALS) (Abrahao et al., 2019). Therefore, it could be used for drug delivery to achieve neuropharmacological regulation of specific brain regions (Airan et al., 2017). Low-intensity ultrasonic stimulation could also regulate neurons without UCA (Khraiche et al., 2008; Tufail et al., 2010).

Ultrasound-related technologies have made significant progress in recent years, and focused ultrasound is a powerful tool for basic and clinical neuroscience research. tFUS could penetrate the skull and focus on specific brain regions to regulate neuronal activity (Baek et al., 2017; Fini & Tyler, 2017).

However, the mechanism of ultrasonic neuromodulation remains controversial. Nerve impulses were earlier thought to be electrical signals; the excitation was caused by the depolarization of cell membranes beyond the threshold potential. However, it was now recognized that nerve impulses were a combination of electrical, mechanical, chemical, and conformational changes that excited cells rather than caused by a single signal. Focused ultrasound might be involved in the aforementioned processes that induced nerve impulses. There were five potential mechanisms for ultrasonic neuromodulation: capacitive current generated by cell membrane displacement; activation of mechanosensitive channels; ultrasonic cavitation effect; action wave, and thermal effect (Kamimura et al., 2020). Ultrasonic stimulation might trigger an action potential through these mechanisms. However, the underlying mechanisms of tFUS neuronal regulation remain unclear. Therefore, exploring the mechanism of tFUS plays a crucial role in whether ultrasonic neuromodulation can be widely applied to basic scientific research and clinical treatment.

1.4 Mechanisms of ultrasound neuromodulation

Ultrasound neuromodulation technology has been gradually applied to various fields of neuroscience, but its underlying mechanism is still controversial. In the early years, the nerve impulse was an electrical signal excited by the cell membrane's depolarization beyond the threshold potential. However, now it is recognized that nerve impulse is a combination of an electrical signal, mechanical, chemical, and conformational changes of excited cells. Excitatory and inhibitory nerve impulses respond to electrical, chemical, mechanical, and thermal stimuli.

This introduction summarizes five possible mechanisms: capacitance current due to cell membrane displacement; activation of mechanosensitive channels; cavitation effect, action wave, and thermal effect. Through these potential mechanisms, ultrasonic stimulation may trigger an action potential. The research on the neural regulation mechanism of ultrasound can help us better use ultrasound to regulate the activity of neurons.

1.4.1 Capacitance current due to cell membrane displacement

The first potential mechanism ultrasound regulates neuronal activity is thought to be caused by membrane capacitance produced by cell membrane displacement. Initially, models of the propagation of nerve impulses in neurons assumed that the capacitance of cell membranes was fixed (Hodgkin & Huxley, 1952). Subsequent studies have shown that changes in membrane properties (thickness of the membrane, curvature, and conformational state of lipids in the membrane) led to changes in capacitance, which might induce excitation of nerve impulses (Heimburg, 2012; Mosgaard et al., 2015; Petrov, 2002; Shapiro et al., 2012, 2017; Taylor et al., 2017). After that, studies have found that ultrasonic radiation could cause the lipid membrane's oscillation and displacement, resulting in changes in membrane area and capacitance (Prieto et al., 2013), which triggered nerve impulses. If the disturbance caused by the ultrasonic stimulation was strong enough to compress the force, the resulting current was excitatory; if the disturbance was expansive, the resulting current was inhibitory. This finding matched the fact that ultrasound could excite and inhibit neuronal activity.

1.4.2 Activation of mechanosensitive channels

The second potential mechanism of ultrasonic regulation is activating mechanosensitive ion channels. The activity of ion channels was regulated by changing the conformation of channel proteins and the conformation states of surrounding lipids and other macromolecules (Perozo et al., 2002; Seeger et al., 2010). Many mechanosensitive ion channels have been found to respond to ultrasonic stimulation (Brohawn, 2015; Morris, 2011). At present, the ion channels that were regulated by ultrasound have been found, including the two-hole potassium ion channel family (Kubanek et al., 2016), TREK-1 (KCNK2), TREK-2 (KCNK10), and TRAAK (KCNK4); $Na_{V1.5}$ (Scn5a) (Kubanek et al., 2016), Piezo1 (Liao et al., 2019; Prieto et al., 2018), MscL1 (J. Ye et al., 2018), TRPA1 (Duque et al., 2022; Oh et al., 2019), TRP4 (Ibsen et al., 2015), MEC4 (Kubanek et al., 2018) and MEC6 (Zhou et al., 2022). Because mechanosensitive channels were transmembrane proteins that responded to mechanical forces or pressures, conformational changes caused by ultrasound-induced tissue compression, tension, or shear forces might increase the probability of channel opening, which further led to ion permeability, depolarization, and subsequent activation of ion channels, generating action potentials (Baek et al., 2017). The above findings suggested that mechanical forces applied by ultrasound acted on ion channels to alter neuronal activity.

1.4.3 Ultrasonic cavitation effect

The ability of ultrasound to modulate brain function may also result from acoustic cavitation within the cell bilayer membrane (Krasovitski et al., 2011; Plaksin et al., 2014). Acoustic transport opened a hole, or other transports were activated by acoustic stimulation, distinct from ion channels in the cell membrane. Ultrasound could pass through physical pores created in the bilayer, which provided a new pathway for ion transport, driven by ion concentration gradients on the cell membrane. The possibility of forming holes in the membrane was related to the membrane's compressibility and specific heat capacity (Blicher et al., 2009; Wunderlich et al., 2009). The specific heat capacity had a local peak during the phase transition, so if the ultrasonic disturbance could push the phase transition of the membrane to a local peak, the hole formation rate would increase (Tata & Dunn, 1992). Even without the formation of holes, the permeability of the cell membrane would change with varying conformation, which would affect the hydrophobic core in the solvent environment (Koynova & Caffrey, 1995; L. Yang & Kindt, 2015). Therefore, if the conformational state of the membrane was changed by ultrasonic stimulation, the membrane permeability was also changed, which drove the change of ionic current (Tata & Dunn, 1992).

Ultrasound cavitation could also temporarily open the blood-brain barrier (BBB), enhancing BBB permeability (Chu et al., 2015). This process required the injection of microbubbles to enhance the holes formed by ultrasound. Microbubbles are small spheres between 1 and 10 μm in size filled with inert gases or perfluorocarbons in a lipid or protein capsid. In the energy field of low-frequency ultrasound, microbubbles could continue to compress and stretch, oscillate symmetrically and expand. In this process, annular forces were generated around the microbubbles, temporarily opening the BBB by mechanical stretching blood vessels. FUS combined with microbubbles to open the BBB has been used to target drug delivery to specific brain regions, treating glioma (Treat et al., 2007), Alzheimer's disease (Jordão et al., 2010), and Parkinson's syndrome (Samiotaki et al., 2015) in animal models, providing a feasible plan for the treatment of CNS-relating diseases. However, this effect may disrupt the BBB, and its safety is questionable.

1.4.4 Action wave

The communication between neurons is transmitted along the axon through action potential (AP^2), which is related to the action wave (AW) propagating along the axon or plasma membrane (El Hady & Machta, 2014). AW was a mechanical wave driven by electrical changes in AP^2, much like a speaker used charge separation to drive sound waves. AW could also respond to mechanical stimuli and generate coupling potentials in neurons, which were the basis for AW to generate nerve impulses and biological signals. Therefore, if ultrasonic stimulation was coupled to AW of the axon (Fichtl et al., 2016), a corresponding electrochemical reaction could be induced, and nerve impulses could be generated.

1.4.5 Thermal effect

In addition to the biological effects caused by mechanical forces, ultrasonic stimulation can also cause a rise in the subject's temperature, which may also lead to the thermo-neural regulation of ultrasound (Blackmore et al., 2019). Infrared neural stimulation (INS) regulated the nervous system through heat generation by incident ultrasonic wave (Chernov & Roe, 2014); a simple 1-millisecond infrared pulse was used to depolarize the cell membrane of neurons and generate an action potential. The mechanism of action was transient local heating caused by water's absorption of infrared light (Wells et al., 2007). INS has been used in the nervous system to study the connection between vision and somatosensation; it acted on specific functional domains and affected behavioural changes in non-human primates during waking states (Chernov & Roe, 2014). HIFU with sound intensity over 200 W/cm^2 transmitted continuous waves to tissues, rapidly heating tissues locally, and was widely used in tissue burning therapy. However, lower intensity ultrasound (0.5-100 W/cm^2) was unlikely to produce thermal effects. However, it could still produce significant mechanobiological effects on cells and tissues, especially in pulse mode, further reducing the probability of tissue heating (Baek et al., 2017). Therefore, the principle of the thermal effect of ultrasonic neural regulation needs further study to clarify its mechanism.

1.5 Project goals

Impairment of somatosensory pathways could cause neuropathic pain, affecting 7% to 10% of the world's population (Dahlhamer et al., 2018). Still, treatments for neuropathic pain were not specific and often ineffective (Finnerup et al., 2015). Commonly used opioids would cause life-threatening side effects, hence the urgent need for improved and patient-specific treatments in neuropathic pain (Meacham et al., 2017).

Ultrasonic stimulation was a potential candidate to alleviate pain. Ultrasonic stimulation was sufficient to induce sensory changes; for example, it caused photophysics perception in the primary visual cortex (W. Lee, Kim, et al., 2016), and it led to tactile changes in the primary and secondary somatosensory cortices (W. Lee, Chung, et al., 2016; W. Lee, Kim, et al., 2016). Ultrasound could also regulate impaired somatosensory pathways. The application of ultrasound on dorsal root ganglion desensitized pain sensation in rats with nerve injury, suggesting that tFUS had a relieving effect on neuropathic pain (Hellman, Maietta, Byraju, Linda Park, et al., 2020; Hellman, Maietta, Byraju, Park, et al., 2020). Ultrasound applied to the forehead of the brain of patients with chronic pain significantly improved the subjective mood, with a slight improvement in the visual analogue scale of pain reporting (Hameroff et al., 2013). Ultrasound applied to the right anterior thalamus in healthy individuals could remarkably reduce the sensitivity to heat pain (Badran et al., 2020). These results suggested that tFUS could relieve and treat pain by acting on pain-related sites.

Several ultrasonic parameters will affect the ultrasound neuromodulation outcomes (G. Li et al., 2019). Figure 1.5.1 shows a typical pulse ultrasonic waveform model. According to the equation of ultrasonic intensity (G. Li et al., 2019), the amplitude of sound pressure, duration of ultrasonic stimulation T_3, duration of stimulus repetition T_4, and duty cycle (T_1/T_2 and T_3/T_4) closely affect the ultrasonic stimulation intensity. Also, it is reported that different pulse repetition frequencies ($1/T_2$) vary the stimulus effects.

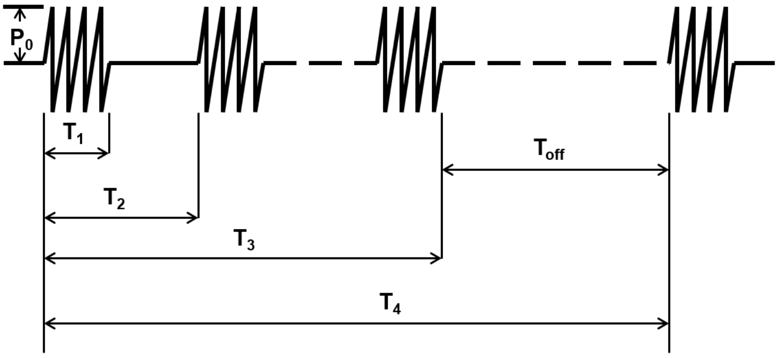

Figure 1.5.1 Pulse ultrasonic parameter pattern.

P_0, the amplitude of sound pressure; T_1, duration of the sustained pulse; T_2, pulse repetition period; T_3, duration of ultrasonic stimulation; T_4, duration of stimulus repetition; T_{off}, stop time of ultrasonic stimulation.

1. Introduction

Pain is the unpleasant sensory and emotional experience caused by actual or potential tissue damage. When pain occurs, it may be acute, persistent, or chronic (Basbaum et al., 2009). Among those different types of pain, chronic pain seems useless and afflicts patients for a long time, which changes the peripheral and central pain neural circuits. In the peripheral nervous system, one of the main changes is the enhanced sensitivity of peripheral nerve terminals to sensory stimuli; the other is the transmission of sensory signals to the spinal cord. In the central nervous system, chronic pain mainly results from altered spinal cord excitability and higher brain pain centers, enhancing the responses to sensory input (Colvin & Colvin, 2012). The retrosplenial cortex (RSC) processes noxious information and responds to nociceptive stimuli in pain neural circuity (Figure 1.5.2) (Da Silva & Seminowicz, 2019; Quintero, 2013; Sikes et al., 2008). In the RSC of rabbits, 12% of neurons responded to visceral nociceptive stimulation, and 23% responded to cutaneous nociceptive stimulation, which first reported the nociceptive activity in RSC (Sikes et al., 2008). In chronic pain rats, 30% of brain activity in RSC showed pain-induced changes detected by regional cerebral blood flow (Paulson et al., 2000); c-Fos neurons were induced by peripheral pain stimulation, and the expression number was significantly elevated in RSC (Lei et al., 2004); the decreased metabolic signal was also detected in RSC (C. E. Kim et al., 2014). It could be concluded that nerve injury induces remarkable changes in RSC. Our previous study found the cell-type dependent transcriptional changes in RSC induced by peripheral nerve injury. Compared with naïve mice, nociceptive stimulation activated more retrosplenial neurons in the mice with nerve injury. When these splenial neurons were inhibited, the pain threshold of mice was significantly elevated in the mice with nerve injury or not those with sham surgery, which indicated that RSC played an essential role in the pain regulatory network (J.-H. Wang et al., 2021). Therefore, tFUS acting on RSC was likely to affect nociceptive behaviour.

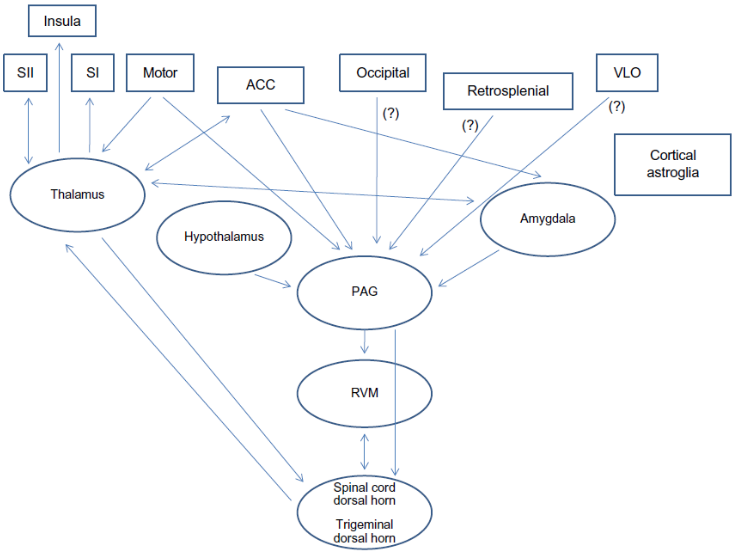

Figure 1.5.2 Ascending and descending interconnections between cortical and other structures involved in pain modulation (Quintero, 2013)**.**

Note and abbreviations: (?), potential projections from these structures; ACC, anterior cingulate cortex; PAG, periaqueductal gray; RVM, rostral ventromedial medulla; SⅠ, primary somatosensory cortex; SⅡ, secondary somatosensory cortex; VLO, ventrolateral orbital cortex.

Nociceptive flexion reflex (NFR) is a reflection of nociceptive afferent activation of spinal pain reflex circuits; therefore, this method has been widely used as a pain readout in rodents, where the stimulus is applied to the paw or tail, and the withdrawal is used as a readout for the animal’s pain sensitivity (Abdus-Saboor & Luo, 2022). There are several different approaches, such as manual and electronic Von Frey, Randall-Selitto, and Hargreaves tests, gait analysis, weight-bearing, burrowing, and facial grimace scales (Deuis et al., 2017). Among those methods, the manual Von Frey (mechanical stimuli) and Hargreaves (heat stimuli) tests are still widely used to detect the changes in pain sensitivity, which are the golden standards to measure the pain threshold in rodents. There are many nociceptors, with a peripheral branch terminating in the skin of the hindpaw of rodents. The mechanical or heat stimuli activate those nociceptors, and the signals are then delivered to the spinal cord and brain for processing as the pain sensation (Deuis et al., 2017).

In order to investigate how tFUS regulates the neuronal activity and modulates ethology and how to connect them, the possible hypothesis and associated aim are proposed below.

Hypothesis:

tFUS probably regulates neuronal activity through specific mechanosensitive ion channels and further regulates the function of target brain regions (Legon et al., 2012; P.-F. Yang et al., 2018).

Aim:

In order to answer this question, the pain-related brain area RSC is selected as the target of tFUS. The multi-channel recording is conducted to detect neuronal activity. The Von Frey ethological assay and Hargreaves system detect the pain threshold in naïve and neuropathic pain mice. Calcium imaging, patch-clamp recording, and RNA-seq uncover tFUS-sensitive cellular characteristics.

.

Chapter 2 Materials and methods

2.1 Experimental animals

The Animal Ethics Committee approved all the Zhejiang University School of Medicine animals in the experiment. All the experiments were conducted according to the International Standards for the Protection and Use of Experimental Animals (No. : ZJU2015-177-01). Mice were raised in a Specific pathogen Free (SPF) environment in the Animal Center of Zhejiang University Medical College. The temperature was kept at 19℃ to 25℃, the humidity was 60% to 65%, and the ambient light was held at 12 hr bright and dark schedule (light 07:00-19:00). The mice acclimated for about a week before the formal test. We managed biohazardous waste by Chinese medical waste management regulations. Tg (Egr1-GFP) GO90Gsat/Mmucd transgenic mice, male, 8~10 weeks old, derived from C57BL/6J mice. B6 (U)-CDH23V-2J/J transgenic mice (Cdh23), male and female, 8~10 weeks old, derived from C57BL/6J mice.

2.2 Ultrasonic neuromodulation

Ultrasonic stimulation was performed through a head-mounted ultrasonic transducer (G. Li et al., 2019) and the brain stimulation system (Qiu et al., 2017). The head-mounted ultrasonic probe had a diameter of 5 mm and a resonant frequency of 0.74 MHz. The mice were first anaesthetized by intraperitoneal injection of pentobarbital sodium (50 mg/kg, Sigma, Cat#P3761). The base was installed on the skull above the RSC (AP, -1.5 mm; ML, ±0.2 mm), and two stainless steel screws were implanted into the head to support the base. The ultrasound base and screws were further fixed with dental cement. Both control and tFUS mice were conducted the surgery and implantation. The mice were tested one week after recovery. The head-mounted probe was connected to the ultrasonic base by an ultrasonic coupling agent filled into the base during the test. The brain stimulation system produced an ultrasonic pulse stimulation with a sound pressure of 214 kPa (100% amplitude) every 1.5, 3, or 10 s and lasted 2 min through a head-mounted stimulator. The pulse duration was 0.5 ms, the pulse repetition time was 1 ms, and the stimulation duration was 300 ms.

2.3 Patch-clamp recording

Human embryonic kidney cells (HEK-293T) were cultured in DMEM (Corning Cellgro, Cat#10-017-CVA) containing 5% fetal bovine serum (Excel. Bio, Cat# FCS500). The medium also contained 5% F12 (Gibco^{TM}, Cat#11765-054) and penicillin/streptomycin (Gibco^{TM}, Cat#15140122). 0.25% trypsin (Gibco^{TM}, Cat#25200056) digestion was performed every 2~3 days. All the cultures were placed in a 3.5 cm NEST dish at 37℃ and 5.0% CO_2. Trpc4 plasmid

(ORIGENE, Cat#MR226912) was transfected into HEK-293T using Lipofectamine^{TM} 3000 transfection reagent (Invitrogen^{TM}, Cat#L3000075). After transfection for 12-14 hr, the fluorescence of the fluorescent protein could be seen under a fluorescence microscope (Olympus, Cat# CKX53). In inside-out mode, the current of Trpc4 cells was recorded by HEKA EPC 10 amplifier controlled by Patch Master software (HEKA). Borosilicate glass was used as raw material, and the absorbent sheet resistant to ~6 MΩ was prepared by fire polishing. Electrophysiology bath and pipette solutions were used in recording. The membrane potential was kept at 0 mV at the beginning, -60 mV for 200 ms, and then 0 mV for 50 ms as a cycle. The current was sampled at 10 kHz and filtered at 2.9 kHz. All records were recorded at 22℃ with a maximum variation of 1℃. Trpc4 inhibitor ML204 was injected into the patch-clamp electrode. The inhibitor ML204 was dissolved in dimethyl sulfoxide (DMSO) as a storage solution (221 mM) and diluted with bath solution (10 μM) before the experiment. An ultrasonic stimulator with a resonant frequency of 0.74 MHz was installed on the side of the cell culture dish, and the ultrasonic probe was immersed in the bath above the recorded cells. The pulsed ultrasonic stimulator performed pulsed ultrasonic stimulation every 3 s for 5 min at a sound pressure of 214 kPa (25% amplitude). The pulse duration was 0.5 ms, the pulse repetition time was 1 ms, and the stimulation duration was 300 ms.

2.4 Electrode implantation and surgery

The mice were anaesthetized with 5% isoflurane in an induction chamber and 2.5% isoflurane through a facemask. Mice were secured in a stereotaxic frame (RWD Life Science, Shenzhen, China) and implanted with 4-5 jeweller's screws to anchor the combined base structure of electrodes and ultrasound transducer. Because of steric hindrance from the ultrasound transducer, the 8-channel electrode implantation angle on the horizontal plane was 30 degrees aiming at the RSC (AP, -1.58 mm; ±ML, 0.2 mm; DV, -2.0 mm). After surgery, mice recovered for 4-7 days. Data were recorded using the NeuroStudio data acquisition system (BrainTech Inc, Jiangsu, China). Electrodes were connected to a headstage containing 32 gain operational amplifiers. Neuronal activity was recorded at 30 kHz, bandpass filtered from 1 kHz to 5 kHz, and isolated automatically by the acquisition processor system (BrainTech Inc). OfflineSorter (Plexon, USA) was used for performing single-unit spike sorting. Customized MATLAB R2020b (MathWorks) programs performed the remaining analyses.

2.5 Calcium imaging of living cells

Trpc4 plasmid (ORIGENE, Cat# MR226912) was transfected into HEK-293T using Lipofectamine^{TM} 3000 transfection reagent (Invitrogen^{TM}, Cat# L3000075). To obtain stably expressing Trpc4 cells, we used G418 sulfate (BBI, Cat# A600958) to screen. In preparation for cell imaging, cells were inoculated in a 3.5 cm glass substrate dish (NEST, Cat#801002) at optimum concentration. Before imaging, the cells were washed twice with calcium imaging buffer (CIB). After washing, 2 μM Fluo-4 (Invitrogen^{TM}, Cat# F14217) in 1 mL CIB was incubated in a dark petri dish at 37℃ for 30 min. After incubation, the CIB containing Fluo-4 was replaced with a fresh buffer (de Melo Reis et al., 2020). Real-time images were generated by a confocal microscope (OLYMPUS IX83-FV3000), and the data obtained were analyzed by ImageJ. Control, Trpc4, and ML204 groups received ultrasonic stimulation. The resonant frequency of the ultrasonic probe was 0.74 MHz. The stimulation system produced an ultrasonic pulse stimulation with a sound pressure of 214 kPa (100% amplitude) every 3 s and lasted 2 min through a head-mounted stimulator. The pulse duration was 0.5 ms, the pulse repetition time was 1 ms, and the stimulation duration was 300 ms.

2.6 Neuropathic pain model

The model of neuropathic pain is established by referring to existing literature reports (Vadakkan et al., 2005): the mouse left lower limb common peroneal nerve (CPN) ligation was used for surgical modelling. After intraperitoneal injection of pentobarbital sodium (50 mg/kg, Sigma, Cat#P3761), the hair at the lateral knee joint of the left lower extremity was shaved with a hair shaver. After disinfection with iodophor and alcohol, a longitudinal incision was made at the middle groove of peroneus longus and peroneus breus at the surface of the fibula 3 mm away from the left knee, with a length of about 1 cm. Then cut fascia, and separate long peroneal muscle and short peroneal muscle by blunt dissection. Under a surgical microscope showing CPN, it always accompanies blood vessels along with a horizontal angle between 30 and 40 degrees of an inclined downward trend. CPN was gently isolated with a glass needle and ligated with 5-0 silk thread. And then, muscle and skin incisions were sutured. The operation procedure of the sham group was the same as above, but the common peroneal nerve was not ligated.

2.7 Von Frey behavioural assay

The Von Frey behavioural assay was performed according to the up-down algorithm described by Dixon (Chaplan et al., 1994). We placed the animals in a clear plastic box containing a raised mesh grid and applied calibrated Von Frey filaments to the middle of the plantar surface of each centre of the left hindpaw until the filament bent. Brisk withdrawal or paw flinching was considered a positive response. In the absence of a response, the filament of the next greater force was applied. Following a response, the filament of the next lower force was used. "X" was marked as the positive response of the mouse, and "O" was recorded as no withdrawal. The 50% response threshold was treated as the paw withdrawal threshold (PWT), which was calculated by using the formula: 50% g threshold = $10^{(X_f + k\delta)/10000}$, where X_f is the value (in log units) of the final Von Frey hair used; k is the tabular value for a pattern of positive/negative responses, and δ is the mean difference (in log units) between stimuli (here 0.296). To determine the effects of tFUS, we applied trains of ultrasound pulses three stimuli of 2 min at 5-min intervals, and the PWT was measured at the end of each 2 min tFUS, and the control mice were not applied to tFUS. The head-mounted ultrasonic probe had a diameter of 5 mm and a resonant frequency of 0.74 MHz. The brain stimulation system produced an ultrasonic pulse stimulation with a sound pressure of 214 kPa (100% amplitude) every 3 s and lasted 2 min through a head-mounted stimulator. The pulse duration was 0.5 ms, the pulse repetition time was 1 ms, and the stimulation duration was 300 ms.

2.8 Thermal sensation test

The thermal sensation was examined using the Hargreaves system (Hargreaves et al., 1988) (Ugo Basile, Gemonio, Italy, Cat#37370-001) to measure the paw thermal withdrawal latency (TWL). We habituated the mice to the testing chamber seven days before the test and acclimatized them to the enclosure room for 30 min per day. Before the test, we left the animals in the same enclosure chamber for about 30 min. We moved the infrared emitter/detector directly underneath the centre of the left hindpaw during the test, emitted the infrared laser, and recorded the TWL. The cut-off time was 20.0 s to prevent tissue damage. We performed the test at least three times to calculate the average reaction time of each mouse. To determine the effects of tFUS, we applied trains of ultrasound pulses three stimuli of 2 min at 5-min intervals, and the TWL was measured at the end of each 2 min tFUS, and the control mice were not applied to tFUS. The head-mounted ultrasonic probe had a diameter of 5 mm and a resonant frequency of 0.74 MHz. The brain stimulation system produced an ultrasonic pulse stimulation with a sound pressure of 214 kPa (100% amplitude) every 3 s and lasted 2 min through a head-mounted stimulator. The pulse duration was 0.5 ms, the pulse repetition time was 1 ms, and the stimulation duration was 300 ms.

2.9 Open-field test

Open-field test (OFT) was widely used to examine the animals' motor ability and anxiety. The open-field test was adapted from the protocol reported by Choleris (Choleris et al., 2001). The individual mouse was released facing the corner of a square open-field arena. The light intensity was 657 lux or 0.96 W/m^2. The animal freely moved in the arena for 5 min. During the 5-min testing, tFUS was applied for 2 min, beginning 1 min after the start of the test. The head-mounted ultrasonic probe had a diameter of 5 mm and a resonant frequency of 0.74 MHz. The brain stimulation system produced an ultrasonic pulse stimulation with a sound pressure of 214 kPa (100% amplitude) every 3 s and lasted 2 min through a head-mounted stimulator. The pulse duration was 0.5 ms, the pulse repetition time was 1 ms, and the stimulation duration was 300 ms.

2.10 Elevated plus-maze test

The elevated plus-maze (EPM) comprised two open arms (30×5 cm) without walls and two enclosed arms (30×5 cm) with 15-cm-high walls on each side. The arms were 60 cm above the ground. All mice were individually tested in 5-min sessions each; in the tFUS group, tFUS was applied for 2 min, beginning 1 min after the start of the test. The maze was cleaned thoroughly with 75% ethanol between each test. Movements were tracked and analyzed offline using ANY-maze software (Stoelting, Illinois, USA). The head-mounted ultrasonic probe had a diameter of 5 mm and a resonant frequency of 0.74 MHz. The brain stimulation system produced an ultrasonic pulse stimulation with a sound pressure of 214 kPa (100% amplitude) every 3 s and lasted 2 min through a head-mounted stimulator. The pulse duration was 0.5 ms, the pulse repetition time was 1 ms, and the stimulation duration was 300 ms.

2.11 Novel object recognition

The novel object recognition (NOR) test draws on the behavioural paradigm reported in previous studies (Leger et al., 2013). In short, each test mouse was placed in a 45 cm×45 cm plastic box and acclimated to the new environment for 10 min. Then, two identical objects were placed in the middle of the box, 10 cm away from the inner wall, and tFUS was given the second minute during the 5-min exploration period. After 24 hr, the mouse was put back into the test box again, and one of the recognized objects was replaced with a new object with a different shape and colour, and the mouse was free to explore the new and old objects for 5 min. The any-maze software was used to record the mice's time near the object. The recognition index measured how long the mice spent on new and old objects. Recognition index: Old (A2)% = (time of A2 being recognized in Section 1)/(total time of A1+A2 being recognized in Section 1); Novel (B)% = (time of B being recognized in section 2)/(total time of A1+B being recognized in section 2). The head-mounted ultrasonic probe had a diameter of 5 mm and a resonant frequency of 0.74 MHz. The brain stimulation system produced an ultrasonic pulse stimulation with a sound pressure of 214 kPa (100% amplitude) every 3 s and lasted 2 min through a head-mounted stimulator. The pulse duration was 0.5 ms, the pulse repetition time was 1 ms, and the stimulation duration was 300 ms.

2.12 Stereotaxic injection

Adult mice aged 2~3 months, 22~30 g, were injected intraperitoneally with pentobarbital sodium (50 mg/kg, Sigma, Cat#P3761). After deep anaesthesia, the head of the mouse was carefully fixed on a stereoscopic brain locator with a temperature maintainer. The hair on the skull surface was removed with a razor and then disinfected with iodine and 75% medical alcohol. Open the skin's surface (to a small incision operation window), wipe the skull with 30% hydrogen peroxide, expose the anterior fontanelle point, and wipe the hydrogen peroxide solution to remove the mucous membrane on the skull. The height of the anterior and posterior fontanelles was then measured using a locator needle to ensure the same height between the anterior and posterior fontanelles, and the RSC was located according to the mouse brain atlas (AP: -1.58 mm; ML: ±0.2 mm; DV: -1 mm). After the localization of the brain, with the help of stereoscopic surgery, the cranial drill was carefully drilled. Microinjection pump for bilateral virus injection, each side was not more than 1 μL, the experimental group and control group were injected with the same amount of virus, injection speed of 0.05 µL/min, 10 min after the injection to ensure that the virus fully spread and not overflowed along the needle path. Finally, the skin was sutured carefully, and all mice were kept in a thermostatic device until they were completely awake and then returned to the cage.

2.13 Targeted recombination in active population test

To selectively inhibit Egr1-positive cells after tFUS, targeted recombination in the active population (TRAP) was applied to correlate the expression of Cre with an ultrasonic-induced expression of Egr1. Egr1 acted as the promoter in this system, followed by the sequence ^{ERT2}Cre^{ERT2}. Therefore, the production of Egr1 activated ^{ERT2}Cre^{ERT2}. Intraperitoneal injection of 4-hydroxytamoxifen (4-TM) in mice induced the entry of Cre into the nucleus, which recombined the sequences between LoxP sites. In order to control the activity of neurons, chemogenetic inhibition hM4Di (Gi) was added, clozapine nitrogen oxide (CNO) was combined with hM4Di to inhibit the activity of neurons, and Cre controlled DIO-hM4Di (Gi) expression. Virus injection was divided into four groups: Ⅰ: CMV-AAV9-mCherry and Syn-Flex-GFP, Ⅱ: CMV-AAV9-mCherry and Syn-DIO-hM4Di (Gi)-GFP, Ⅲ: Egr1-^{ERT2}Cre^{ERT2}-mCherry and Syn-Flex-GFP, Ⅳ: Egr1- ^{ERT2}Cre^{ERT2}-mCherry and Syn-DIO-hM4Di (Gi)-GFP. A virus was injected into the RSC (AP: -1.58 mm; ML: ±0.2 mm; DV: -1 mm) of mice. After 21 days of viral expression, the RSC of the mouse was stimulated by ultrasound for 2 min. The head-mounted ultrasonic probe had a diameter of 5 mm and a resonant frequency of 0.74 MHz. The brain stimulation system produced an ultrasonic pulse stimulation with a sound pressure of 214 kPa (100% amplitude) every 3 s and lasted 2 min through a head-mounted stimulator. The pulse duration was 0.5 ms, the pulse repetition time was 1 ms, and the stimulation duration was 300 ms. After 30 min of ultrasonic stimulation, 4-TM (25 mg/kg, Med Chem Express, Cat#HY-16950) was given intraperitoneally. Three days later, CNO (2 mg/kg, Med Chem Express, Cat#HY-17366) was injected intraperitoneally 30 min before the formal test.

2.14 Real-time quantitative fluorescence PCR experiment

Primers were designed by referring to the sequences of *β-actin, Egr1,* and *c-Fos* in GenBank. The specific sequence information is shown in Table 3.13.1 below. Hangzhou Youkang Biological Co., LTD synthesized the designed primers.

Table 2.14.1 Primer sequences for real-time quantitative fluorescence PCR

Primer	**Primer suquence（5'-3'）**
Egr1 forward	ATGGTGGAGACGAGTTA
Egr1 reverse	GAGGAAGACGATGAAGC
c-Fos forward	AGACCGTGTCAGGAGGCA
c-Fos reverse	CCATCTTATTCCGTTCCCT
β-actin forward	TGTTACCAACTGGGACGA
β-actin reverse	GTCTCAAACATGATCTGGGTC

After ultrasonic stimulation, the mice were anaesthetized with pentobarbital sodium (50 mg/kg, Sigma, Cat#P3761). After anaesthesia, the mice were immediately decapitated on an ice plate, their brains were taken, and the RSC was observed under an anatomical microscope. According to the TransZol Up Plus RNA kit (TransGen Biotech, Cat#er501-01), RNA was extracted from the RSC, and its purity and concentration were measured. A total RNA of 1.0 μg was taken from each group, and reverse transcription was performed by using the reverse transcription reagent HiScript®Ⅱ Q RT SuperMix (Nanjing Novizan Biological Company, Cat#R223). The transcribed cDNA was used as the real-time quantitative PCR reaction template, as shown in table 3.13.2. The real-time PCR experiment obtained the Ct value, amplification curve, and dissolution curve. According to the formula $\Delta Ct = CT_{Target} - CT_{actin}$, the average Ct value of

3 duplicate samples of each sample was taken to calculate the ΔCt value of each target gene relative to the reference gene *β-actin*, using $2^{-\Delta\Delta Ct}$ (Livak & Schmittgen, 2001) method, the relative expression level of each gene was calculated.

Table 2.14.2 Real-time quantitative PCR reaction system and procedure

Reaction system	Volume (uL)	Program
2×PCR mix	5	95℃ 3 min
Forward primer	0.4	95℃ 5 s
Reverse primer	0.4	40 cycles
cDNA	1	60℃ 15 s
H_2O	3.2	

2.15 Immunofluorescent staining

After deep anaesthesia with pentobarbital sodium (50 mg/kg, Sigma, Cat#P3761), the chest cavity was cut open, and the heart was exposed. An incision was made in the right auricle, and the perfusion needle was inserted from the left ventricular apex to the aorta. The blood in the tissue was removed by slow perfusion with pre-cooled PBS. When the colour of the liquid turned pale to colourless, 4% paraformaldehyde (PFA) was applied until the limbs and tail of the mice became stiff. After perfusion, the whole brain was carefully removed, immersed in 4% PFA for fixation, and placed at 4℃ overnight. The fixed tissues were subjected to gradient dehydration and were first placed in a 15% sucrose solution at 4℃ overnight. After the tissues completely sank, the fixed tissues were replaced with 30% sucrose solution and completely sank at 4℃. Coronal sections were performed on a freezing microtome after embedding the tissue with an OCT embedding agent. 30 μm thick brain slices containing the RSC region were collected and evenly affixed to polylysine-coated carrier slices. The brain slices were rinsed with PBS 3 times and then blocked with donkey serum solution containing 0.3% Triton X-100 at room temperature for 1 hr. The blocking solution was discarded, and a primary antibody was diluted with 0.3% Triton X-100 donkey serum (Egr1, 1:1000; NeuN, 1: 500; c-Fos, 1:1000), placed in a wet box, and incubated at 4℃. On the second day, the wet box was removed from 4℃ and rewarmed for 30 minutes at room temperature. The primary antibody was discarded and rinsed with PBS 3 times. The fluorescent secondary antibody, appropriately diluted with 2.5% donkey serum, was added and incubated at room temperature to avoid light for 1 hr. The second antibody was adsorbed and discarded, rinsed with PBS 3 times, sealed with an anti-fluorescence quench agent containing DAPI, dried at room temperature, and observed under a laser confocal microscope. The staining results were processed and analyzed by ImageJ. The regions selected for analysis (RSC: AP, -1.58 mm; ±ML, 0.2 mm; DV, -2.0 mm) were based on the mouse brain atlas of the ultrasonic target. The insets were chosen in a similar region; however, there were some deviations in location.

2.16 Nissl staining

For the frozen sections, rinse the sections with distilled water for 2-5 min; add Nissl staining solution (Sangon Biotech, Cat#E607316) and incubate at room temperature for 10-30 min; wash twice with distilled water for 2 min each. Finally, samples can be observed under microscopy.

2.17 Single-cell isolation and RNA-sequencing

Single-cell isolation: the mice were anaesthetized with isoflurane; the head was cut off quickly, the RSC was taken out, and the tissue was chopped up on an ice plate and put into 1 mL digestive solution for digestion at 37℃ for 30 min. After complete digestion, the tissue was blown 12 times with a rounded tip three times to obtain the supernatant. Gradient centrifugation followed, in which the single-cell suspension and debris were stratified, and the single-cell suspension was carefully sucked out. After the initial count and cell survival status were checked under the microscope, the 10×Genomics was used to capture single cells.

10×Chromium single-cell transcriptome sequencing (scRNA-seq): microfluidic technology sorted single cells. The gel beads with barcode, primers, and single cells were wrapped in oil droplets, in which the coagulation dissolved, oligo was released, and mRNA was released by cell rupture. Barcode cDNA was obtained by the SMART method. The region near polyA at the 3' end was used for library construction sequencing, and the samples were processed with a V3 kit. Read1 was composed of 16 bp sequences of 10×cell barcode and 12 bp sequences of unique molecular identifiers (UMI). Barcode was used to label a single cell and was present on random nucleotide sequences of reverse transcription primers. Read 2 was a 151 bp cDNA sequence, and generally, only the first 98 bp was used for downstream analysis of Cell Ranger. In order to identify effective cells, 10×single cell marker should meet at least one of the following requirements: (1) barcode sequence existed in the list of known markers in the 10×single cell marker database; (2) the Hamming distance between the barcode obtained by sequencing and the sequence in the known barcode list was 1. The posterior probability of the barcode generated by sequencing error was calculated according to the prior probability of base quality and candidate barcode count distribution. When the posterior probability was ≥ 0.975, the barcode sequence obtained by sequencing would be corrected. In order to remove PCR duplication in sequencing, the UMI sequence of read 1 was corrected with the following UMI correction criteria: (1) UMI did not contain N; (2) The base mass of UMI was greater than or equal to 10; (3) UMI with 1 Hamming distance in the same cell was corrected to UMI with more read support. The number of high-quality cells was determined based on the UMI number distribution of cells. The evaluation method was to arrange the UMI number of each barcode in descending order, which was greater than or equal to 10% of the 99% UMI number distribution in the preset cell number as the threshold, to screen cells with high RNA abundance, and identify cells with low RNA abundance through background model. Therefore, we got high-quality cells. In the analysis, the dual-terminal sequencing mode of the 10×single cell building database and Illumina sequencing platform were adopted to conduct high-throughput sequencing of samples, and Cell Ranger, the 10×internal software, was conducted the data quality statistics of original data. The reference genome was compared with the Ensembl database. Then, according to the cell filtration index, the number of genes selected was greater than or equal to 200 by default, the UMI number of mitochondrial genes was less than or equal to 10%, and the UMI sequence proportion of red blood cell marker genes was less than or equal to 10%. The double cells were removed, and high-quality single cells were obtained by filtration. The sequenced read number of all samples, number of original evaluated cells, average read number of each cell, the median number of expressed genes per cell, effective barcode, sequencing saturation, alignment rate, and number of filtered cells were counted.

Cell clustering: for UMI sequence numbers of high-quality single cells and genes in the sample, the total UMI number of each cell and the scaling factor ratio of 10000 were calculated. In order to correct the depth of cell sequencing, normalized processing was carried out, and principal component analysis (PCA) was performed for genes with a high degree of variation measured by diffusion coefficient component analysis to detect the similarity between cells in a dimensionless way. The closer the sample distance was, the closer the gene expression trend was. For the top 30 principal components with the most considerable interpretation variance in PCA results, *t*-distributed neighbour embedding (*t*-SNE) and uniform manifold approximation (UMAP) were adopted. These two-dimensionality reduction methods were used to visualize single-cell clusters, respectively. The principle of the *t*-SNE display method was to recalculate the Euclidean distance between samples in a high-dimensional space through the conditional probability of random neighbour chimerism based on the student's *t*-distribution so that samples in a low-dimensional space can present separated clusters. Merge the filtered cells of two or more samples, and the analysis results were stored in the merged subfolder alongside the sample name. Seurat was used for clustering analysis of high-quality cell populations. PCA space was constructed based on Euclidean distance to construct a KNN (K-nearest neighbour) graph. Then, the Louvain Modularity optimization algorithm was used for clustering cell populations. Cloupe can import projection_*t*-SNE_SC.csv's *t*-SNE coordinates, projection_UMAP_SC.csv's UMAP coordinates, and clusters_SC.csv's clustering categories. Cloupe used Loupe Cell Browser for visualization.

Cell marker gene analysis: Given Seurat's cell clustering results, we first analyzed the overall correlation and PCA between the cell groups and then used Seurat's FindAllMarkers function bimod likelihood ratio statistical test to screen differentially expressed genes in different cell populations. Meet the P_adj < 0.05 and $|\log_2$（fold change）$| > 1$ between the designated cell population and the rest of the cell population of differential genes. The top 10 or 30 genes were screened for heat map, feature plot, violin plot, and dot plot. GO, and GSEA used the Clusterprofiler R package to analyze. The potential cell-to-cell communication pathways were analyzed using the CellChat R package.

2.18 RNA-seq based on fluorescence-activated cell sorting (FACS)

The method for cell isolation of adult mouse brain tissue was based on the reported method (Brewer & Torricelli, 2007). The adult mice were injected intraperitoneally with a compound anaesthetics agent. The brain was quickly removed, the target area was dissected quickly on the ice, and the tissue was cut into small pieces. The shredded tissue was then transferred to a 1.5 mL centrifuge tube. Use a HibernateA (Invitrogen, Cat#A1247501)/B27 (Invitrogen, Cat#A17504) (HABG) medium in 3 mg/ml pronase (Sigma, Cat# p6911-1g) to digest tissue for 30 min in a 37℃ constant temperature shaker at 180 rpm. After digestion, slowly beat the tissue with the polished tip. Centrifugation was performed at a density gradient speed of 800 g for 15 min. After the centrifugation, the suspension of the target cells was absorbed and added into a 5 mL PBS solution without calcium and magnesium ions. The cells were cleaned and centrifuged at 200 g for 2 min. After centrifugation, the cellular supernatant was discarded, and cells were re-suspended with PBS. Cell number and health status were determined by trypan blue staining. Subsequently, FACS (Cat# BD FACS ORP ARIA Ⅱ) was used to divide Egr1-green fluorescent protein (GFP) cells and non-GFP cells. Next, the collected cells were lysed, reversely transcribed into cDNA, and amplified. The average length of the amplified DNA fragment was about 200 bp, and TruePrepTM Index Kit V3 for Illumina® (Vazyme™, Cat# TD203) was used. Connect the Illumina sequencing connector, TruePrepTM DNA Library Prep Kit V2 for Illumina® (Vazyme™, Cat# td501-td503) libraries were constructed and checked with the Agilent Bioanalyzer 2100 system and Qubit 2.0 Fluorometer (Invitrogen, Carlsbad, CA, USA). The average length of the final cDNA library was 350 bp (±50 bp). After the library was qualified, conducted pooling of different libraries according to the effective concentration and the amount of data obtained, performed Illumina Hiseq X-TEN (LC Bio, China) sequencing and produced a 150 bp paired terminal reading.

Cutadap (M. Martin, 2011) was used in the bioinformatics analysis to remove reads containing joint contamination, low-quality bases, and uncertain bases. Then use FastQC to control serial quality. We used HISAT2 (D. Kim et al., 2015) to map the mouse genome GRCm38 in Ensemble92 and String Tie (Pertea et al., 2015) to assemble each sample's read mapped. Then, the transcripts of all samples were combined and reconstructed into a comprehensive transcriptome using Perl scripts. Finally, after the transcriptome was generated, the expression levels of all transcriptomes were estimated using String Tie (Pertea et al., 2015) and Ballgown (Frazee et al., 2015). Through the edgeR package (Robinson et al., 2010), $|\log_2(\text{fold change})| > 1$ and $P\_\text{adj} < 0.05$ statistically significant difference mRNA was selected. GO, and GSEA used the Clusterprofiler R package to analyze.

2.19 Statistical analysis

Data were expressed as mean ± s.e.m., paired, unpaired Student’s *t*-test, and Tukey's multiple comparisons test, measured differences between the two groups, and comparison between groups was performed by chi-square test (χ^2 test), Fisher’s exact test; one-way ANOVA, two-way ANOVA, two-way repeated measures ANOVA and Sidak’s multiple comparisons test were used for comparison between multiple groups. GraphPad Prism 8, $P < 0.05$, was considered statistically significant.

Chapter 3 Trpc4 as a key factor for the tFUS neuromodulation in RSC

3.1 Transcranial-focused ultrasound (tFUS) modulated pain behaviour in mice

A neuromodulation system was used (Figure 3.1A). Signals were first generated by a function generator, amplified by a power amplifier, and delivered by the head-mounted ultrasonic probe to transmit ultrasonic waves. These ultrasound waves penetrated the skull and entered specific brain areas to induce non-invasive neuromodulation (G. Li et al., 2019). The ultrasonic probe consists of five parts: electrical socket, metal housing, gasket, piezoelectric ceramic, and focusing lens. The ultrasonic base was fixed with skull nails and dental cement, and the ultrasound probe was installed on the mouse's target brain region (G. Li et al., 2019; Qiu et al., 2017) (Figure 3.1B). An ultrasonic coupling agent was filled in the base to avoid air disturbance during ultrasonic transmission. Then, ultrasonic waves were delivered to the mice when they moved freely for the behavioural test. The ultrasonic parameters are shown in Figures 3.1C and D.

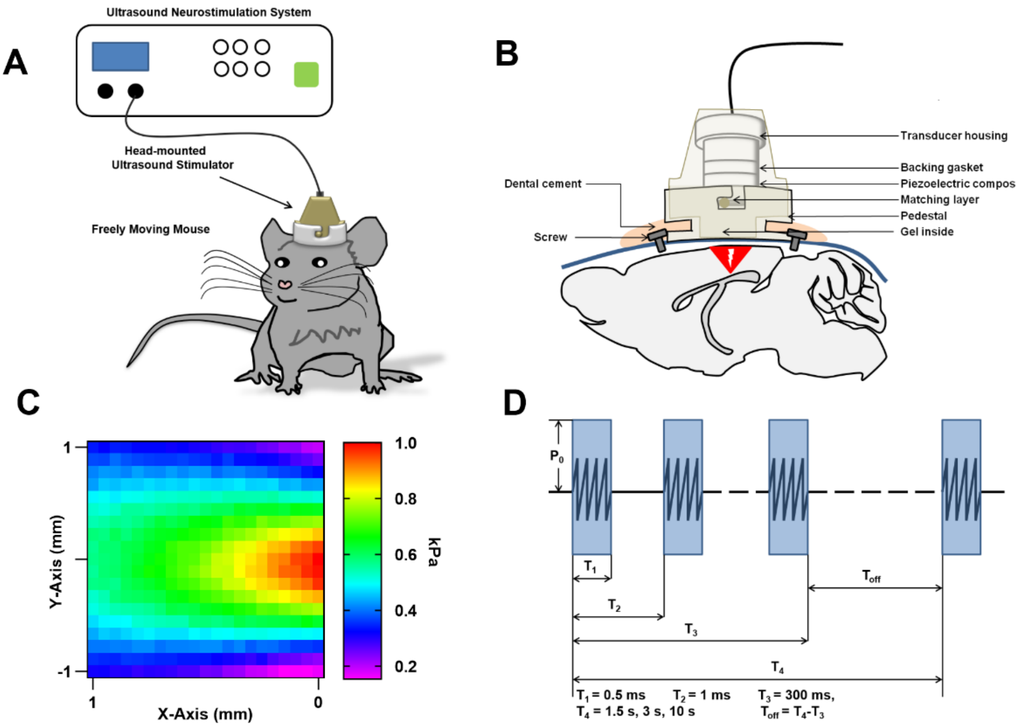

Figure 3.1 Schematic diagram of ultrasound neuromodulation.

(A) Schematic illustration of in vivo ultrasonic stimulation in free-moving mice.

(B) Schematic diagram of a head-mounted ultrasonic probe.

(C) Standardized sound pressure distribution diagram of the ultrasonic probe, X-Axis represents the stimulation depth of the probe, and Y-Axis represents the horizontal side of the probe.

(D) Pulse ultrasonic parameter pattern, P_0, amplitude of sound pressure; T_1, duration of sustained pulse; T_2, pulse repetition period; T_3, duration of ultrasonic stimulation; T_4, duration of stimulus repetition; T_{off}, stop time of ultrasonic stimulation. Specific parameters of transcranial focused ultrasound (tFUS) are as follows: T_1 = 0.5 ms; T_2 = 1 ms; T_3 = 300 ms; T_4 = 1.5 s, 3 s, 10 s; $T_{off} = T_4 - T_3$; P_0 = 214 kPa.

3.1.1 tFUS targeting RSC could regulate pain behaviour in mice

In order to verify the effect of tFUS on pain behaviour in mice, the retrosplenial cortex (RSC) (Quintero, 2013; Sikes et al., 2008), processing somatosensory stimulus information, was selected as the center targeted for tFUS. PWT and TWL were measured during tFUS. In order to avoid the temperature dramatically increasing of the target, the ultrasonic amplitude, T_1, T_2, and T_3 remained constant and just changed the duration of stimulus repetitions of tFUS. The results showed that PWT and TWL were significantly increased when the stimulus repetition time T_4 was 3 s (Figures 3.1.1A and B), so this tFUS stimulus parameter was selected for subsequent molecular biochemistry and animal behaviour tests.

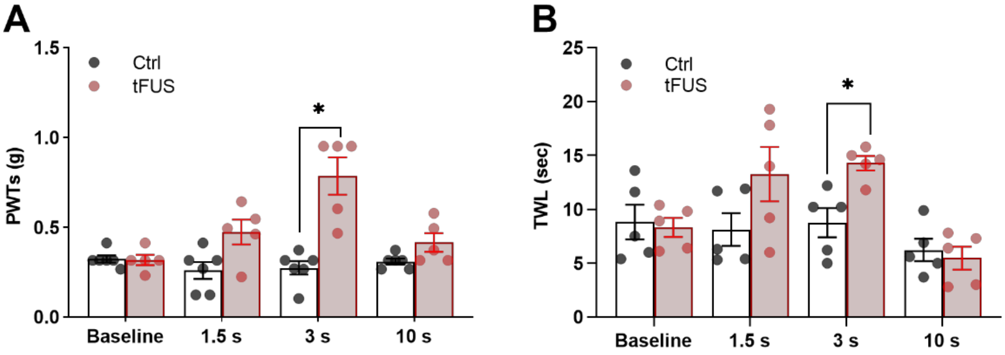

Figure 3.1.1 Behavioural effects of tFUS targeting retrosplenial cortex (RSC).

(A) tFUS of different T_4 (T_4 is 1.5 s, 3 s, and 10 s, respectively) acting on RSC induces the effects on PWT. Two-way repeated measures ANOVA, interaction: $F_{(3, 27)} = 10.78$, $P < 0.0001$; different T4: $F_{(3, 27)} = 7.438$, $P = 0.0009$; Control (Ctrl) *vs.* tFUS: $F_{(1, 9)} = 23.66$, $P = 0.0009$; n (Ctrl) = 6 and n (tFUS) = 6.

(B) tFUS of different T_4 acting on RSC induces the effects on TWL. Two-way repeated measures ANOVA, interaction: $F_{(3, 24)} = 2.837$, $P = 0.0594$; Different T_4: $F_{(3, 24)} = 6.142$, $P = 0.003$; Ctrl *vs.* tFUS: $F_{(1, 8)} = 5.539$, $P = 0.0464$; n (Ctrl) = 6 and n (tFUS) = 6.

All data are means ± s.e.m. $^*P < 0.05$.

3.1.2 tFUS regulated pain sensation with target specificity

Then, we wanted to know whether tFUS regulated pain sensation with target specificity. Therefore, tFUS was applied to the anterior cingulate cortex (ACC) to investigate whether tFUS specifically affects the pain threshold. ACC was chosen as the target because it relates to pain through brain imaging results (Apkarian et al., 2005). PWT and TWL were measured when tFUS stimulated ACC in mice. PWT and TWL were significantly increased compared with the control group (Ctrl) (Figures 3.1.2.1A and B). Reducing ACC neuronal excitability or excitatory synaptic transmission leads to desensitization of nociception (Y.-J. Wang et al., 2020). Thus, tFUS may induce inhibitory effects on ACC.

In addition, we selected the primary motor cortex (M1), which is not part of the pain network (Castillo Saavedra et al., 2014). We found that tFUS acting on M1 did not change the pain threshold of mice (Figure 3.1.2.2A). However, the movement distance of mice in the open-field test (OFT) was significantly decreased (Figures 3.1.2.2B and C), suggesting that tFUS acting on M1 could alter locomotion.

RSC and ACC closely relate to pain; when tFUS acted on them, the PWT and TWL of mice were significantly altered. tFUS acting on M1 had no remarkable impact on the pain sensation but could markedly change the motor ability of mice. Overall, tFUS was specific to the functional regulation of brain regions. Since ACC and RSC belong to the cingulate cortex (Vogt, 2019), we will focus our research on the RSC in the subsequent work.

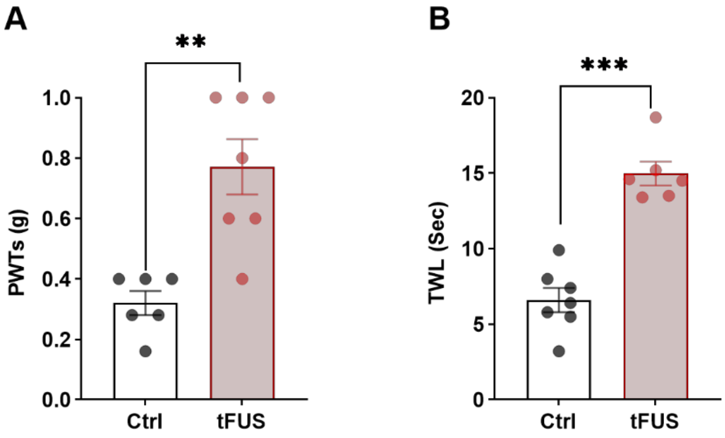

Figure 3.1.2.1 tFUS acting on ACC increases PWT and prolongs TWL significantly.

(A) tFUS targeting ACC remarkably increases PWT. Unpaired *t*-test, $t = 4.24$, $P < 0.01$, n (Ctrl) = 6, n (tFUS) = 7.

(B) tFUS targeting ACC significantly prolongs TWL. Unpaired *t*-test, $t = 7.38$, $P < 0.0001$, n (Ctrl) = 7, n (tFUS) = 6.

All data are means ± s.e.m.; $^{**}P < 0.01$; $^{***}P < 0.001$.

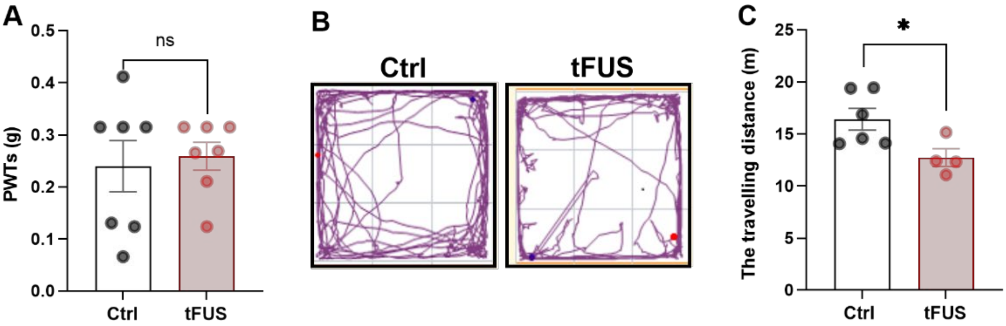

Figure 3.1.2.2 tFUS targeting M1 does not change PWT but affects the travelling distance.

(A) There is no significant change in PWT when tFUS acts on M1 compared to Ctrl. Unpaired *t*-test, $t = 0.3463$, $P = 0.7351$, n (Ctrl) = 7, n (tFUS) = 7.

(B) When tFUS acts on M1, the travelling is significantly reduced compared to Ctrl. Unpaired *t*-test, $t = 2.509$, $P = 0.0364$, n (Ctrl) = 6, n (tFUS) = 4.

All data are means ± s.e.m.; $^{*}P < 0.05$; ns, no significant difference.

3.1.3 tFUS alleviated pain threshold in chronic pain mice

Peripheral nerve damage can cause neuropathic pain, compromising 8% of people (Dahlhamer et al., 2018). Based on our above findings, tFUS could increase the thresholds of PWT and TWL; then, we wanted to know whether tFUS can also affect the threshold in chronic pain mice. In order to answer this question, we applied tFUS to common peroneal nerve (CPN) ligation mice, a neuropathic pain model. The results showed that PWT and TWL significantly decreased seven days after CPN, consistent with previous studies (Y.-J. Wang et al., 2020). The effects of tFUS on RSC were consistent with those of normal mice, increasing PWT and prolonging TWL (Figures 3.1.3A and B). These results suggested that tFUS also had an alleviated effect on the pain threshold in neuropathic pain mice.

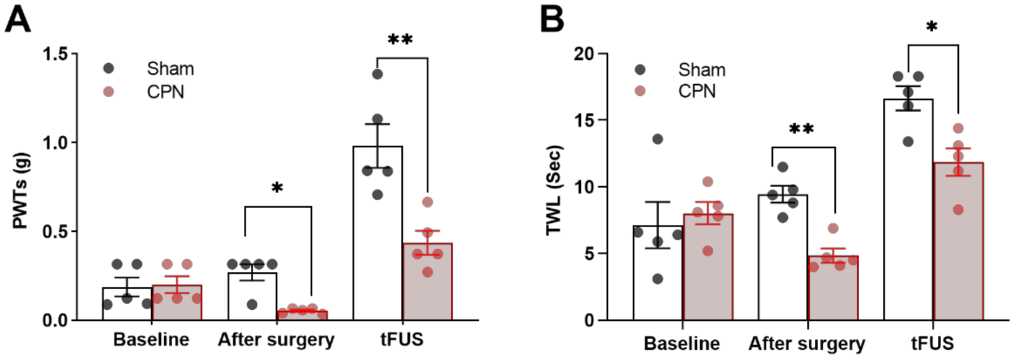

Figure 3.1.3 tFUS acting on RSC increases PWT and prolongs TWL in mice with nerve injury.

(A) tFUS application in RSC significantly increases PWT in sham and common peroneal nerve (CPN) ligation mice. Two-way repeated measures ANOVA, sham *vs.* CPN: interaction, $F_{(2, 16)} = 12.10$, $P < 0.01$; baseline *vs.* tFUS, $F_{(1.45,11.60)} = 62.91$, $P < 0.0001$; sham *vs.* CPN, $F_{(1,8)} = 14.91$, $P < 0.01$; Sidak's multiple comparisons test, sham *vs.* CPN: baseline, $P = 0.99$; after surgery, $P < 0.05$; tFUS, $P < 0.05$; n = 5 per group.

(B) tFUS application in RSC remarkably prolongs TWL in sham and CPN mice. Two-way repeated measures ANOVA, sham *vs.* CPN: interaction, $F_{(2, 16)} = 3.937$, $P = 0.0407$; baseline *vs.* tFUS, $F_{(1,8)} = 24.24$, $P = 0.0012$; sham *vs.* CPN, $F_{(1.198, 9.580)} = 24.01$, $P = 0.0005$; Sidak's multiple comparisons test, sham *vs.* CPN: baseline, $P = 0.9600$; after surgery, $P = 0.0017$; tFUS, $P = 0.0255$. n = 5 per group.

All data are means ± s.e.m. ; $^{*}P < 0.05$; $^{**}P < 0.01$.

3.1.4 tFUS acted on RSC, which did not affect anxiety, learning, and memory in mice

To confirm whether tFUS can produce anxiety-like behaviour in mice and whether it can affect mice's learning and memory ability. Firstly, the open-field and elevated plus-maze paradigms were used to determine whether the mice exhibited anxiety-like behaviour when tFUS acted on RSC. In the open-field test (OFT) (Figure 3.1.4A), there was no significant change in the time and traveling distance of the mice entering the central region under the tFUS condition compared to the Ctrl (Figures 3.1.4B to D). In the elevated plus-maze test (EPM) (Figure 3.1.4E), there was no notable change in the time and entries of the open arms (Figures 3.1.4F to H). Thus, tFUS did not produce anxiety-like emotions in mice.

Secondly, to determine whether learning and memory ability was affected by tFUS, mice were tested by novel object recognition experiments (NOR) (Figure 3.1.5A). The results showed that tFUS did not affect the time to explore the new object (Figures 3.1.5B and C).

Therefore, we concluded that tFUS did not induce anxiety in mice. Moreover, tFUS did not affect mice's learning and memory ability.

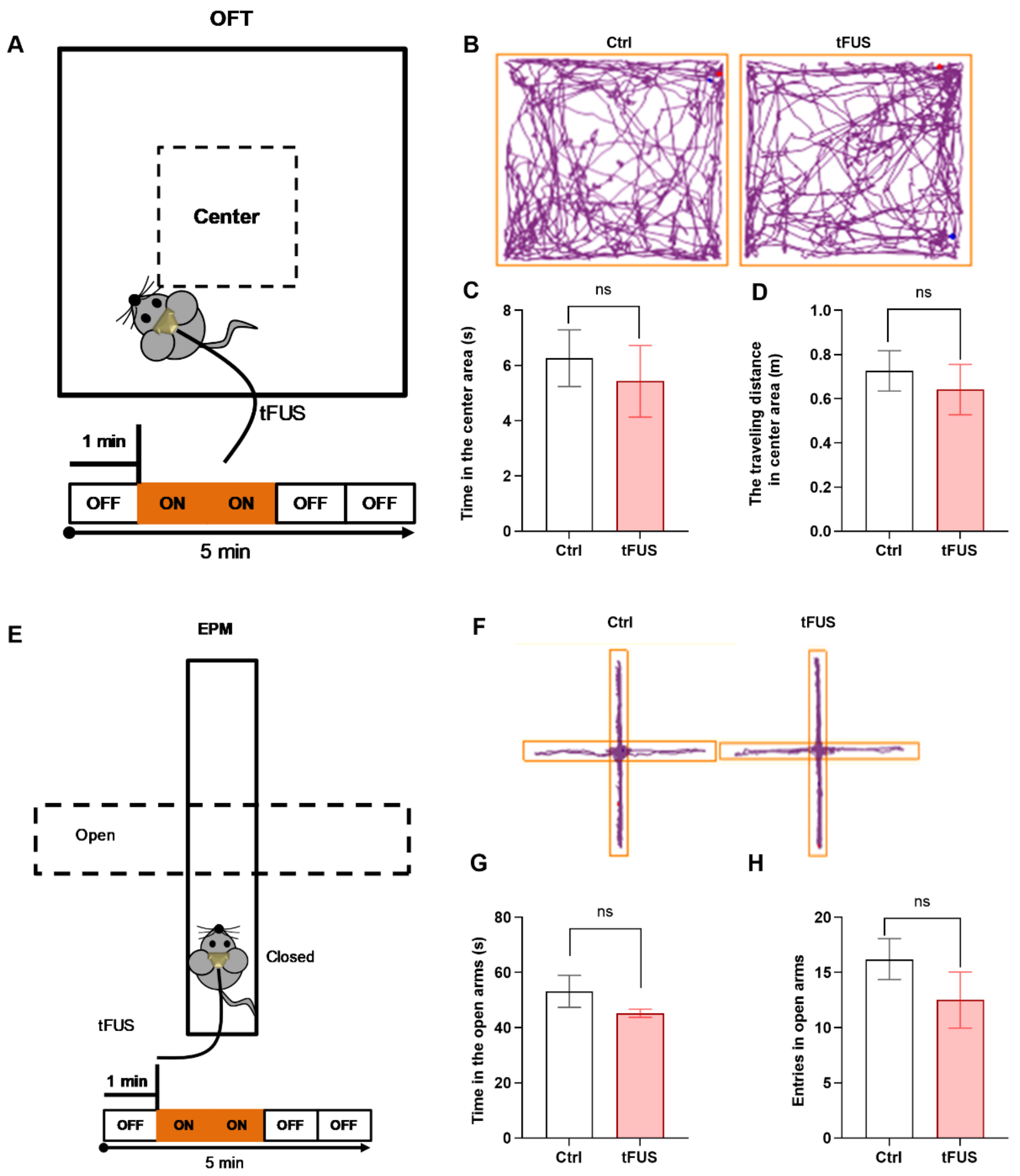

Figure 3.1.4 tFUS acts on RSC, which does not induce anxiety-like behaviours in mice.

(A) The schematic illustration of tFUS acting on RSC in the open-field test (OFT).

(B) Representative trajectories of Ctrl (left) and tFUS (right) in the OFT.

(C) There is no remarkable difference in the time spent in the central area of the open-field between Ctrl and tFUS. Unpaired *t*-test, *t* = 0.5139, *P* = 0.6148, n (Ctrl) = 10, n (tFUS) = 9.

(D) Traveling distance of Ctrl and tFUS in the central area of the open-field. Unpaired *t*-test, *t* = 0.5809, *P* = 0.5690, n (Ctrl) = 11, n (tFUS) = 9.

(E) The schematic illustration of tFUS acting on RSC in the elevated plus-maze (EPM).

(F) Represented trajectories of Ctrl (left) and tFUS (right) in the EPM.

(G) Time in the open arms of Ctrl and tFUS mice in the EPM. Unpaired *t*-test, *t* = 1.185, *P* = 0.2748, n (Ctrl) = 5, n (tFUS) = 5.

(H) Entries of Ctrl and tFUS mice in the EPM. Unpaired *t*-test, *t* = 1.209, *P* = 0.2661, n (Ctrl) = 5, n (tFUS) = 5.

All data are means ± s.e.m.; ns, with no significant difference.

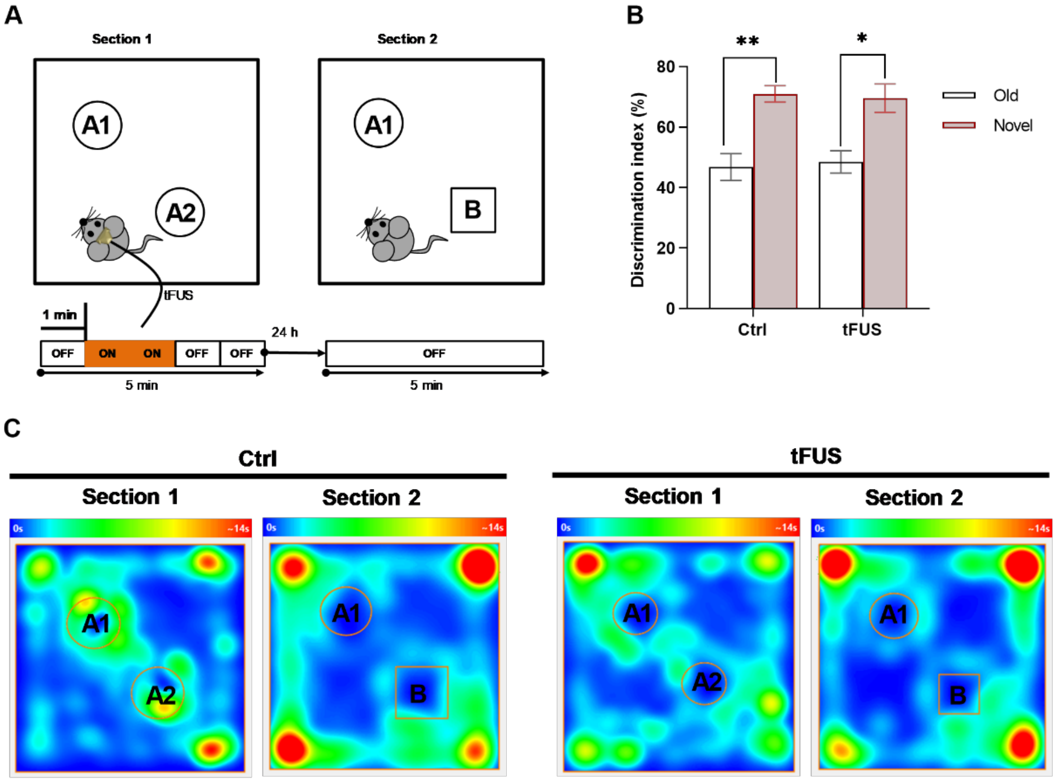

Figure 3.1.5 tFUS acting on RSC does not affect mice's learning and memory

behaviour.

(A) Schematic diagram of tFUS acting on RSC in novel object recognition (NOR) experiment.

(B) The proportion of time spends on the old and the new objects in the NOR. Two-way repeated measures ANOVA, Ctrl *vs.* tFUS: interaction, $F_{(1, 8)} = 0.15$, $P = 0.71$; Ctrl *vs.* tFUS, $F_{(1, 8)} = 0.001$, $P = 0.71$; time spent on objects A and B, $F_{(1, 8)} = 31.22$, $P < 0.001$; Sidak's multiple comparisons test, Ctrl, $P < 0.01$; tFUS, $P < 0.05$. n = 5 mice in both Ctrl and tFUS groups.

(C) Heat maps of trajectory in the NOR test. Ctrl (left), tFUS (right).

All data are means ± s.e.m.; $^{*}P < 0.05$; $^{**}P < 0.01$; ns, with no significant difference.

3.2 Egr1 (early growth response 1) as a marker of tFUS-sensitive cells in RSC

Based on the above findings, tFUS could regulate the function of specific brain regions. Then, we wanted to know how tFUS regulated the activity of cells in the target.

3.2.1 tFUS activated Egr1$^+$ cells in RSC

In order to know how tFUS regulates the cellular activity of RSC, we detected the expression levels of immediate early genes (*IEGs*), which reflected immediate changes in cellular activity activated by external stimulation, such as *Egr1*, *c-Fos* (Renier et al., 2016), in RSC after tFUS. *IEGs* could be activated within a few minutes and without the need for de novo protein synthesis. The results showed that the expression of *Egr1* was significantly increased at 0.5 hr and 2 hr after two-minute-tFUS stimulation compared with the Ctrl (Figures 3.2.1.1A and B). Under the same conditions, the expression of *c-Fos* was elevated at 0.5 hr after tFUS but not 2 hr (Figures 3.2.1.1C and D). To confirm the mRNA expression of *Egr1* and *c-Fos* at 0.5 hr after tFUS stimulation, I selected ACC and M1 as tFUS targets. The results exhibited that the *Egr1* remarkably increased at 0.5 hr after tFUS targeting ACC and M1 (Figure 3.2.1.2A). The *c-Fos* dramatically elevated only in the ACC, but no apparent change in M1 (Figure 3.2.1.2B). Therefore, it could be confirmed that the tFUS-induced changes in *Egr1* are more sensitive and longer than *c-Fos*.

At the protein level, the expression of Egr1 and c-Fos at 50 min (to ensure that the protein has been synthesized) after 2-minute-tFUS acting on RSC was detected by immunofluorescence staining. The ratio of Egr1$^+$/DAPI was noticeably elevated in the tFUS compared to the Ctrl (Ctrl: 5.18 ± 1.39%, tFUS: 65.32 ± 3.01%) (Figures 3.2.1.3A and B), while the ratio of c-Fos$^+$/DAPI was not significantly changed (Ctrl: 8.64 ± 2.34%, tFUS: 9.41 ± 0.73%) (Figures 3.2.1.3C and D).

Considering the changes in mRNA and protein expression levels, Egr1 has a more sensitive and durable response to tFUS than c-Fos, which is easier to detect. Therefore, Egr1 could be viewed as a marker for tFUS-sensitive cells.

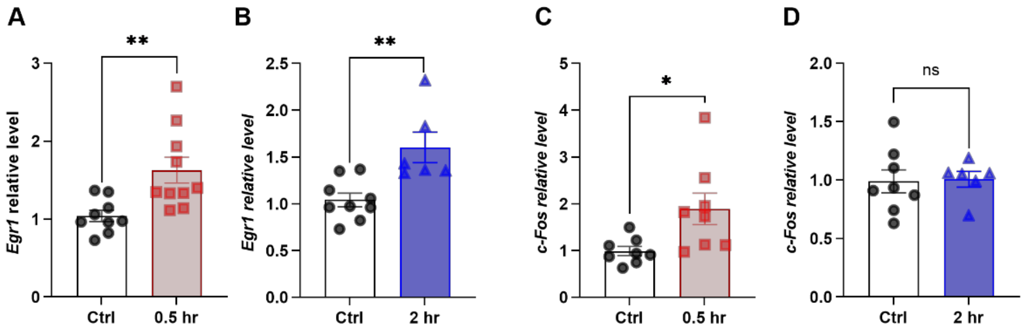

Figure 3.2.1.1 The relative expression of *Egr1* and *c-Fos* changes after tFUS targeting RSC.

(A) The expression of *Egr1* mRNA at 0.5 hr after tFUS acting on RSC. Unpaired *t*-test, *t* = 3.134, *P* = 0.0060, n (Ctrl) = 9, n (tFUS) = 10.

(B) The expression of *Egr1* mRNA at 2 hr after tFUS targeting RSC. Unpaired *t*-test, *t* = 3.552, *P* = 0.0035, n (Ctrl) = 9, n (tFUS) = 6.

(C) The expression of *c-Fos* mRNA at 0.5 hr after tFUS targeting RSC. Unpaired *t*-test, *t* = 2.574, *P* = 0.0221, n (Ctrl) = 8, n (tFUS) = 8.

(D) The expression of *c-Fos* mRNA at 2 hr after tFUS acting on RSC. Unpaired *t*-test, *t* = 0.1438, *P* = 0.8880, n (Ctrl) = 8, n (tFUS) = 6.

All data are means ± s.e.m. **P* < 0.05; ***P* < 0.01; ns, with no significant difference.

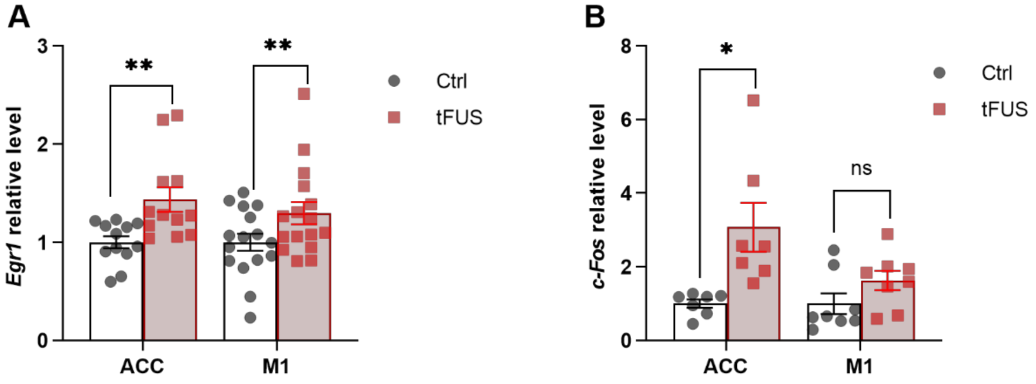

Figure 3.2.1.2 After tFUS targeting ACC and M1, the relative expression of *Egr1* and *c-Fos* changes.

(A) The expression of *Egr1* mRNA level at 0.5 hr after tFUS targeting ACC and M1. ACC: Unpaired *t*-test, *t* = 3.116, *P* = 0.0050, n (Ctrl) = 12, n (tFUS) = 12. M1: Unpaired *t*-test, *t* = 2.064, *P* = 0.0477, n (Ctrl) = 16, n (tFUS) = 16.

(B) The expression of *c-Fos* mRNA level at 0.5 hr after tFUS targeting ACC and M1. ACC: Unpaired *t*-test, *t* = 3.073, *P* = 0.0097, n (Ctrl) = 7, n (tFUS) = 7. M1: Unpaired *t*-test, *t* = 1.628, *P* = 0.1258, n (Ctrl) = 8, n (tFUS) = 8.

All data are means ± s.e.m.; **P* < 0.05; ***P* < 0.01; ns, with no significant difference.

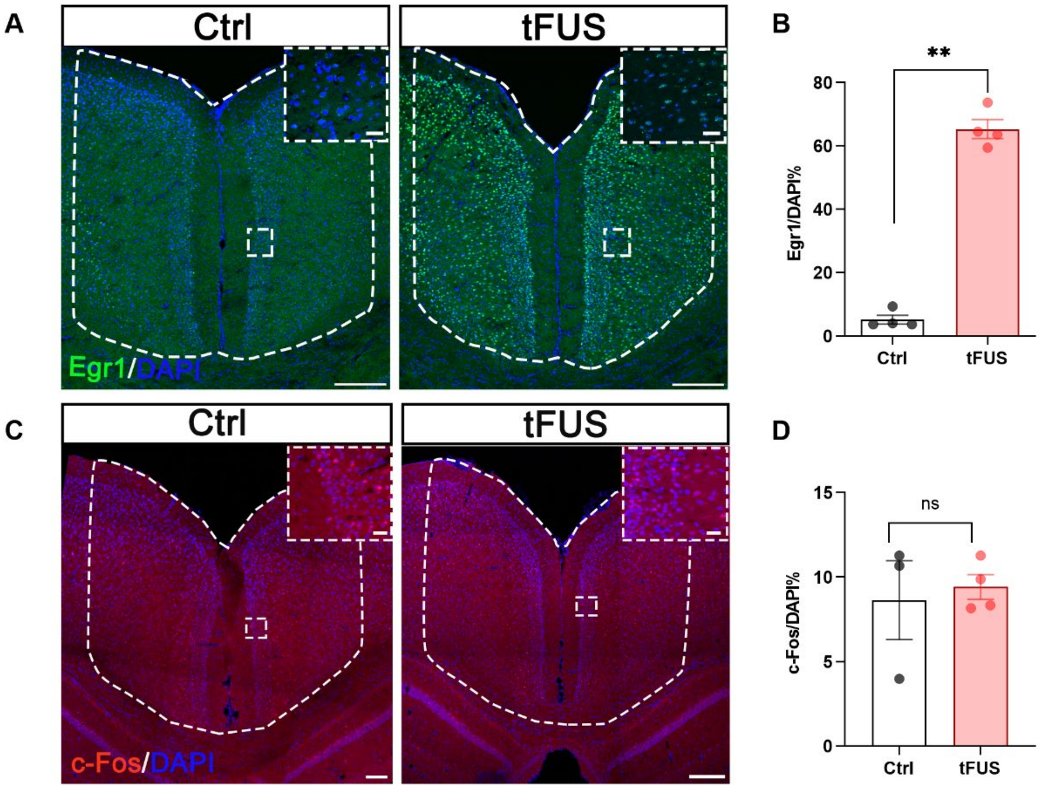

Figure 3.2.1.3 After 50 min for 2-minute-tFUS acting on RSC, the protein expression of Egr1 markedly increases, while c-Fos has no remarkable change.

(A) Ctrl (left) and tFUS (right) Egr1 expression in RSC, the overall scale bar of RSC is 200 μm, and the scale bar of the enlarged area is 20 μm. The white dashed outline is RSC, and the rectangle region is the enlarged area of the partial RSC.

(B) Summary result exhibits the number of Egr1^{+} cells expressed relative to DAPI in RSC of

Ctrl and tFUS groups. Unpaired *t*-test, $t = 18.17$, $P < 0.0001$, n (Ctrl) = 4, n (tFUS) = 4.

(C) Ctrl (left) and tFUS (right) c-Fos expression in RSC, the overall scale bar of RSC is 100 μm, and the scale bar of the enlarged area is 20 μm. The white dashed outline is RSC, and the rectangle region is the enlarged area of the partial RSC.

(D) Summary result exhibits the number of c-Fos$^+$ cells expressed relative to DAPI in RSC of Ctrl and tFUS groups. Unpaired *t*-test, $t = 0.36$, $P = 0.73$, n (Ctrl) = 3, n (tFUS) = 4.

All data are means ± s.e.m.; $^{**}P < 0.01$; ns, with no significant difference.

3.2.2 tFUS regulated RSC neuronal activity

However, whether tFUS-activated Egr1$^+$ cells are primarily neuronal cells remains uncertain. Next, we used neuronal marker NeuN (neuronal-specific nuclear protein) to identify the cell types of tFUS-activated cells. In the tFUS group, approximately 76% of Egr1$^+$ cells were co-labelled with NeuN$^+$ cells. NeuN$^+$ & Egr1$^+$ cells were significantly increased in the tFUS group compared with the Ctrl group (Figures 3.2.2.1A and B). Therefore, we know that the cell type regulated by tFUS was mainly neuron. There were some Egr1 positive signals detected in the control mice because we used Egr1-promoter GFP mice to conduct this experiment, and the spontaneous activity of mice caused the expression of Egr1. To further confirm the changes in neuronal activity induced by tFUS, we implanted 8-channel recording electrodes in the mouse RSC. The spike recorded in RSC was analyzed by principal component analysis (PCA) to obtain a good clustering effect and effective separation of single-neuron discharge (Figures 3.2.2.2A and B). The spike's half-wave width and discharge frequency divided neurons into pyramidal neurons and interneurons (Figure 3.2.2.2C). The mice implanted with the multi-channel electrode and ultrasound probe base received three combined tFUS stimulation cycles (S1, S2, S3) and post-tFUS intervals (AS1, AS2, AS3) (Figure 3.2.2.2D). The spike rate of pyramidal neurons was significantly reduced during 0.3 s of tFUS action (Figures 3.2.2.2E and F). The changes in discharge frequency of these pyramidal neurons were not consistent after tFUS treatment. Some neurons increased their discharge frequency, while others weakened or remained unchanged. These results indicated that the activity of RSC pyramidal neurons under tFUS was inconsistent, and there were characteristics of network coding changes (Figures 3.2.2.2G and H). In addition, it could also be found that the proportion of neuron spike rate decreased was remarkably higher than that of increased (Figure 3.2.2.2I). After analysis, the same variation trend of spike rate was observed in the isolated interneurons (Figures 3.2.2.2J to M). Notably, the proportion of interneurons decreased significantly more than the proportion increased (n = 18 neurons, 50% decreasing, 22% increasing, Fisher's exact test, *P* = 0.03) (Figure 3.2.2.2N).

The way tFUS regulates neurons has been controversial, and some studies have shown that focused ultrasound can directly regulate the activity of neurons (Kubanek et al., 2018; Meneghetti et al., 2020). At the same time, some studies have proven that tFUS may indirectly regulate neuronal activity through sensory pathways (Guo et al., 2018; Sato et al., 2018). A mouse model of congenital deafness with a point mutation of the *Cadherin 23* (*Cdh23*) gene was selected (Cdh23 mice) (F. Han et al., 2012) to clarify the regulation of tFUS on RSC. Cdh23 protein is an important component of the helical hair cell tip. Mutation of *Cdh23* causes hearing loss in mice 27 days after birth and becomes severe with age. Under the sound induction of hearing range (70 dB) (sound stimulation parameters used here were consistent with those of tFUS), wild-type mice (WT) showed noticeable behavioural changes with sound, and the mobile time elevated dramatically. Whereas, Cdh23 mice showed no such response (WT: 52.47 ± 2.15 s; Cdh23: 2.84 ± 1.45 s, $P < 0.01$, Figure 3.2.2.3A), reconfirming that Cdh23 mice did not respond to sound stimulation. The PWT and TWL of Cdh23 mice were markedly increased (Figure 3.2.2.3B) and prolonged (Figure 3.2.2.3C) under tFUS exposure. Subsequently, the expression of Egr1 in the RSC of Cdh23 mice was detected by immunofluorescent staining, and it was found that tFUS considerably increased the number of Egr1^{+} cells (Figures 3.2.2.3D and E). This suggests that tFUS directly regulated neuronal activity in the RSC.

We concluded that tFUS directly regulated neuronal activity in RSC rather than through indirect sensory pathways combined with the above results.

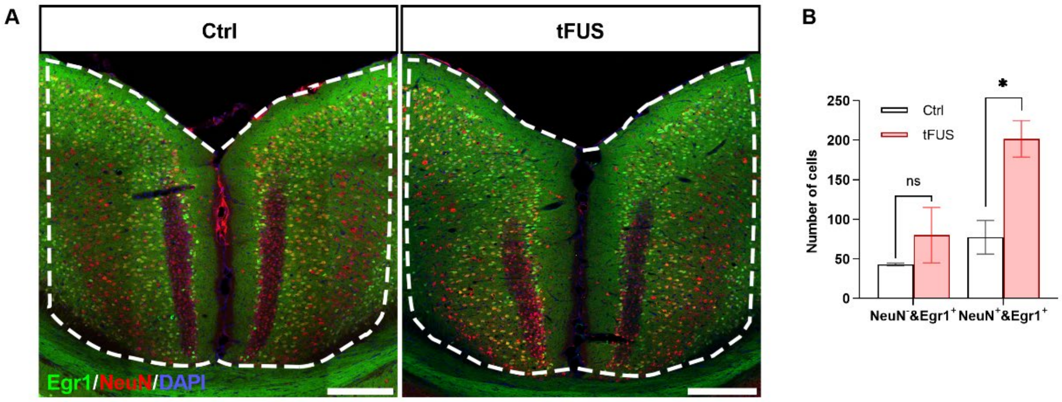

Figure 3.2.2.1 The tFUS-induced Egr1$^+$ cells are mainly neurons.

(A) Coronal section of Egr1$^+$ cells co-located with neuron-specific marker NeuN in the RSC of Egr1-GFP mice (Ctrl on the left and tFUS on the right). The overall scale bar of RSC is 200 μm. The white dashed outline is RSC.

(B) In Egr1 positive cells, the number of NeuN cells (NeuN$^+$ & Egr1$^+$) and non-NeuN cells (NeuN$^-$ & Egr1$^+$). Two-way repeated measures ANOVA, interaction: $F_{(1,8)} = 1.198$, $P = 0.3056$; Ctrl *vs.* tFUS: NeuN$^-$ & Egr1$^+$, $P = 0.6985$; NeuN$^+$ & Egr1$^+$, $P = 0.0387$; n (Ctrl) = 3, n (tFUS) = 7.

All data are means ± s.e.m., $^*P < 0.05$; ns, with no significant difference.

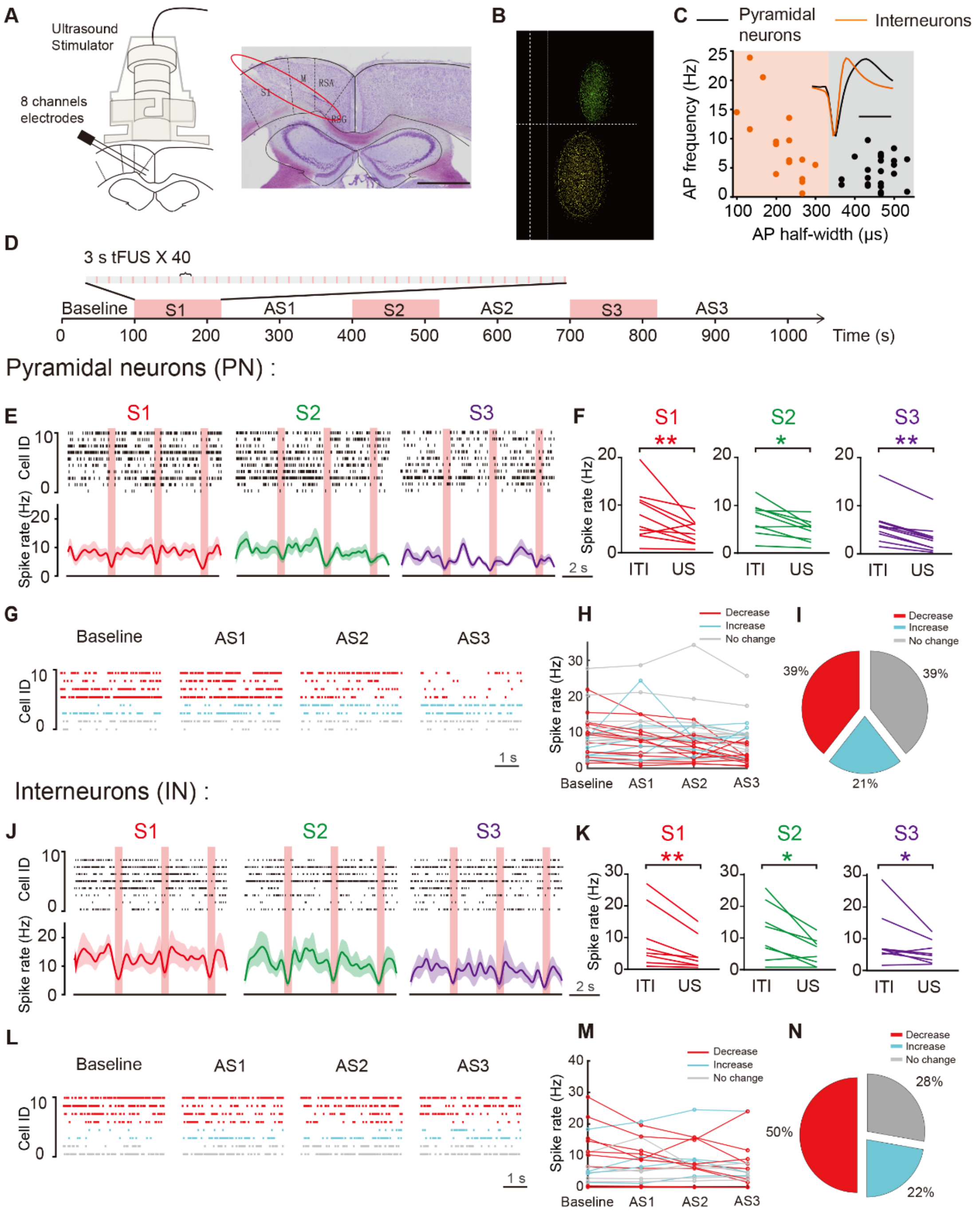

Figure 3.2.2.2 tFUS can temporarily and continuously inhibit RSC neuronal activity.

(A) Left: schematic of the multi-channel electrode is unilaterally implanted in RSC, and the assembled head-mounted ultrasound transducer is fixed to the mouse skull.

Right: this coronal section with Nissl staining shows the trace of multi-channel electrode implantation in the RSC (red circle).

(B) Two-dimensional principal component (PC) analysis waveform clustering example diagram, yellow and green represent two types of well-clustered and differentiated single neuron discharge.

(C) Putative pyramidal neurons (black) are separated from putative interneurons (orange) by unsupervised cluster analysis. Inset: the example action potential waveforms from one putative interneuron and one putative pyramidal neuron (scale bar 400 ms).

(D) Timeline for the experimental protocol. S1: stimulation 1; AS1: after stimulation 1.

(E) - (I) Response of RSC putative pyramidal neurons during and after tFUS.

(E) Rasters of example neurons and mean rate, 95% confidence intervals. Compared to inter tFUS interval (ITI), example neurons show distinctly reduced firing rate during the sustained pulse (US).

(F) Spike firing rate for excitatory neurons during ITI and US; paired *t*-test between ITI and US; $*P < 0.05$, $**P < 0.01$.

(G) Rasters of example, pyramidal neurons during baseline, AS1, AS2, and AS3 periods.

(H) tFUS causes pyramidal neurons spike firing rate changing after stimulation in RSC.

(I) Percentage of decreasing, increasing, and no changing firing rate of pyramidal neurons. (n = 33 neurons, 39% decreasing, 21% increasing, Fisher's exact test, $P = 0.04$).

(J) - (N) Response of RSC putative interneurons during and after tFUS.

(J) Rasters of example neurons and mean spike firing rate, 95% confidence intervals.

Compared to inter tFUS interval, example neurons show distinctly reduced firing rate during US (Red).

(K) Spike firing rate for interneurons during ITI and tFUS; paired *t*-test between ITI and tFUS; **P* < 0.05, ***P* < 0.01.

(L) Rasters of example interneurons during baseline, AS1, AS2, AS3 periods.

(M) tFUS causes interneurons spike firing rate change after stimulation in RSC.

(N) Percentage of decreasing, increasing, and no changing firing rate of interneurons. (n = 18 neurons, 50% decreasing, 22% increasing, Fisher's exact test, *P* = 0.03).

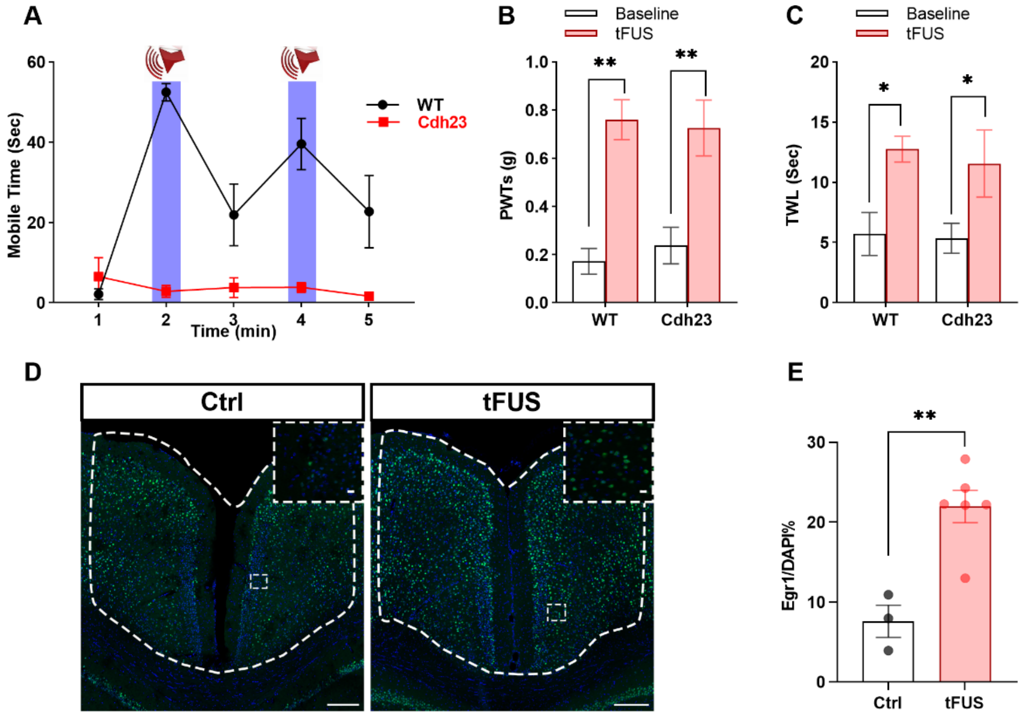

Figure 3.2.2.3 In Cdh23 mice, tFUS can still alter the somatosensory threshold.

(A) Response test of Cdh23 mice to sound stimulation. Two-way repeated measures ANOVA, WT *vs.* Cdh23, $F_{(1, 17)} = 32.93$, $P < 0.0001$; interaction: $F_{(4, 68)} = 14.23$, $P < 0.0001$; different time phases: $F_{(4, 68)} = 11.42$, $P < 0.001$; n (WT) = 9 , n (Cdh23) = 10.

(B) tFUS is applied to RSC, the PWT is detected in WT and Cdh23 mice. Two-way repeated measures ANOVA, interaction: $F_{(1, 5)} = 0.24$, $P = 0.64$; WT *vs.* Cdh23, $F_{(1, 5)} = 0.07$, $P = 0.80$; baseline *vs.* tFUS: $F_{(1, 5)} = 28.67$, $P < 0.01$; n (WT) = 4, n (Cdh23) = 3.

(C) tFUS is applied to RSC, the TWL is detected in WT and Cdh23 mice. Two-way repeated measures ANOVA, interaction: $F_{(1, 5)} = 0.13$, $P = 0.74$; WT *vs.* Cdh23, $F_{(1, 5)} = 0.12$, $P = 0.74$; baseline *vs.* tFUS: $F_{(1, 5)} = 33.17$, $P < 0.01$; n (WT) = 4, n (Cdh23) = 3.

(D) The coronal diagram of Egr1$^+$ expression after tFUS is applied to RSC in Cdh23 mice (Ctrl on the left, tFUS on the right). The overall scale bar of RSC is 200 μm, and the scale bar of the enlarged area is 10 μm.

(E) Expression of Egr1$^+$ cells in RSC of Cdh23 mice after tFUS. Unpaired *t*-test, $t = 4.45$, $P < 0.01$; n (Ctrl) = 3, n (tFUS) = 6.

All data are means ± s.e.m., $^*P < 0.05$; $^{**}P < 0.01$.

3.2.3 tFUS-induced Egr1$^+$ cells were involved in the regulation of pain

Next, we wanted to know whether Egr1-expressing cells modulate pain after tFUS. Targeted recombination in the active population (TRAP) was applied (Figures 3.2.3A to C). In the TRAP system, the sequence of ER^{T2}-Cre-ER^{T2} is inserted after the Egr1 promoter to ensure the expression of Egr1, promoting the expression of subsequent ER^{T2}-Cre-ER^{T2}. 4-Hydroxytamoxifen (4-TM) can activate the expression of cyclization recombination enzyme (Cre), which can move from cytoplasm to nucleus to perform the recombinant enzyme's function further, cleft two LoxP sites, and make the sequence between the two LoxP sites become positive and express. Three weeks after virus injection in RSC, mice were intraperitoneally injected with 4-TM 30 min after tFUS. Three days later, mice received CNO to inhibit ultrasound-activated Egr1 cells, and virus expression was confirmed after the experiment (Figure 3.2.3D). We found that both PWT and TWL were significantly increased in the Ctrl group after CNO injection but not in the TRAP group (Figures 3.2.3E and F). Therefore, when the tFUS-activated Egr1 cells were inhibited, the effect of tFUS on pain sensation was further inhibited. These results reflected that tFUS regulated pain sensation through $Egr1^{+}$ cells in RSC.

Collectively, tFUS induced the expression of $Egr1^{+}$ cells, and these cells mediated the effect of tFUS on pain behaviour. Furthermore, we concluded that Egr1 was a marker of tFUS-sensitive cells in RSC.

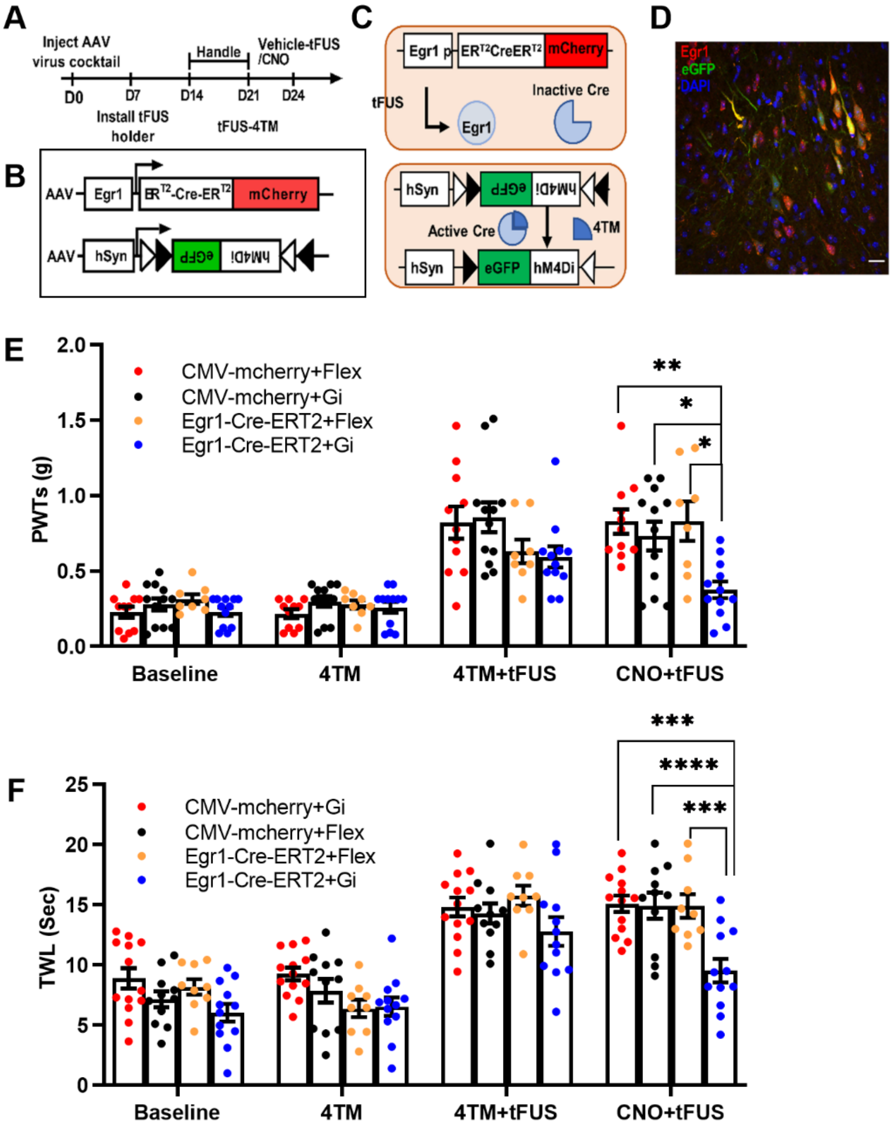

Figure 3.2.3 tFUS-induced Egr1⁺ cells in RSC are necessary for pain behaviour.

(A) Targeted recombination in the active population (TRAP) system experimental flow chart.

(B) Egr1-ER^{T2}CreER^{T2}-mCherry AAV virus and cyclization recombination enzyme (Cre) dependent Syn-DIO-hM4Di-eGFP AAV virus construction element diagram.

(C) Example diagram of TRAP system design: bilateral microinjection of AAV-Egr1-

$ER^{T2}CreER^{T2}$-mCherry and Cre dependent AAV-Syn-DIO-hM4Di-eGFP hybrid virus ($Egr1^{TRAP}$) into RSC, tFUS activates Egr1 expression, resulting in subsequent expression of $ER^{T2}CreER^{T2}$-mCherry. Intraperitoneal injection of 4-hydroxytamoxifen (4-TM) allows Cre to enter the nucleus and drive the expression of recombinant Cre-dependent hM4Di-eGFP.

(D) Example diagram of AAV-Egr1-$ER^{T2}CreER^{T2}$-mCherry and Cre-dependent AAV-Syn-DIO-hM4Di-eGFP virus expression in RSC after tFUS acting on RSC and intraperitoneal injection of 4-TM, scale bar 20 μm.

(E) The effect of TRAP system inhibits tFUS-activated $Egr1^+$ cells on PWT. Two-way repeated measures ANOVA, interaction: $F_{(9, 117)} = 3.516$, $P = 0.0007$; different operations: $F_{(2.363, 92.16)} = 67.4$, $P < 0.0001$; different groups: $F_{(3, 39)} = 4.141$, $P = 0.0122$; n (CMV-mCherry::Gi) = 12, n (CMV-mCherry::Flex) = 13, n (Egr1-$ER^{T2}CreER^{T2}$-mCherry::Flex) = 9, n ($Egr1^{TRAP}$) = 14.

(F) The effect of TRAP system inhibits tFUS-activated $Egr1^+$ cells on TWL. Two-way repeated measures ANOVA, interaction: $F_{(9, 123)} = 1.871$, $P = 0.0623$; different operations: $F_{(3, 41)} = 11.61$, $P < 0.0001$; different groups: $F_{(3, 41)} = 4.141$, $P < 0.0001$; n (CMV-mCherry::Gi) = 12, n (CMV-mCherry::Flex) = 13, n (Egr1-$ER^{T2}CreER^{T2}$-mCherry::Flex) = 9, n ($Egr1^{TRAP}$) = 14.

All data are means ± s.e.m., $^*P < 0.05$, $^{**}P < 0.01$, $^{***}P < 0.001$, $^{****}P < 0.0001$.

3.3 Transcriptome characteristics of the tFUS-sensitive cells

Based on the above results, we identified Egr1$^+$ cells as an essential marker of tFUS-sensitive cells. In order to further screen out the critical factors of tFUS acting on RSC, we selected Egr1-GFP mice and combined fluorescence-activated cell sorting (FACS) to screen tFUS-activated Egr1-GFP cells and cells without GFP, and then the selected cells were used to transcriptomic sequencing. The specific experimental strategy is shown in Figure 3.3. In Ctrl and tFUS samples (Ctrl = 2 groups; tFUS = 2 groups; among them, n = 2 mice in each group), all sorted cells were divided into four groups, namely, cells without GFP (GFP$^-$) and cells with GFP (GFP$^+$) in Ctrl group, and GFP$^-$ and GFP$^+$ in tFUS group.

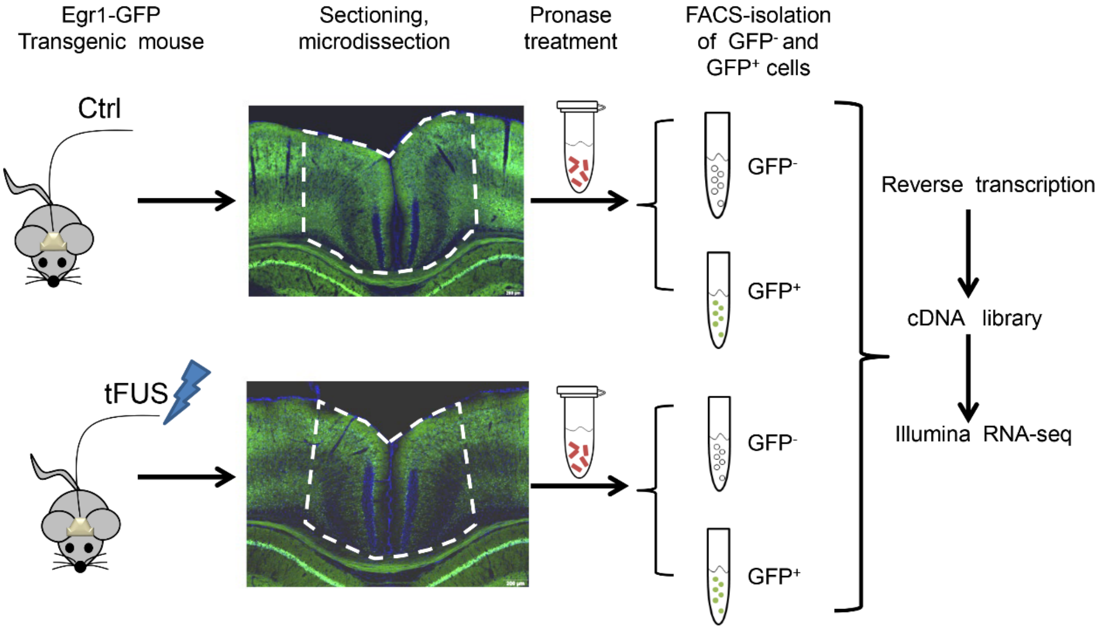

Figure 3.3 Flow chart shows transcriptome sequencing strategy for screening tFUS-

activated cells in RSC.

Egr1-GFP mice in the Ctrl group do not receive tFUS, and Egr1-GFP mice in the tFUS group receive tFUS for 2 min. After 50 min, the brain tissues are isolated and digested by pronase. Single-cell suspension is obtained, and GFP^- and GFP^+ cells are collected by fluorescence-activated cell sorting (FACS). The selected cells are reversely transcribed and amplified into cDNA libraries. The Illumina system sequences the final cell libraries.

3.3.1 *DEG* characteristics of tFUS-sensitive cells

According to the transcriptome sequencing results of tFUS-sensitive cells, we performed quality control, transcription quantification, data transformation, correlation analysis, and principal component analysis (PCA) samples for the obtained data. Then, we conducted differential expression analysis. In the process of genetic detecting, $| \log_2 FC | > 1$ and $P\_adj < 0.05$ as selection criteria, volcano plots exhibit *DEGs* distribution (Figures 3.3.1A and B). Red dots represent a significant increase in genes, blue dots represent a significant decrease in genes, and grey dots represent not significantly different genes. Figures 3.3.1A and B show the *DEG* volcano plots of GFP^- and GFP^+ cells in Ctrl and tFUS. The number of *DEG* in tFUS was markedly more than Ctrl, and most *DEGs* were remarkably upregulated. From the Venn diagram of *DEG* (Figure 3.3.1C), there are 53 *DEGs* with notable changes between GFP^- cells and GFP$^+$ cells in the Ctrl group. In the tFUS group, GFP$^-$ and GFP$^+$ cells had 786 *DEGs* with marked changes. The Ctrl and tFUS groups had 20 identical *DEGs*. There were still 8,438 genes with no significant differences. Specifically, 75.47% (40/53) of Ctrl's *DEGs* were up-regulated genes, and 24.53% (13/53) of *DEGs* were down-regulated genes (Figure 3.3.1D). In tFUS, 99.36% (781/786) of *DEGs* were up-regulated, and 0.64% (5/786) of *DEGs* were down-regulated (Figure 3.3.1E). Thus, tFUS induced changes in the expression of most genes in *Egr1*$^+$ cells.

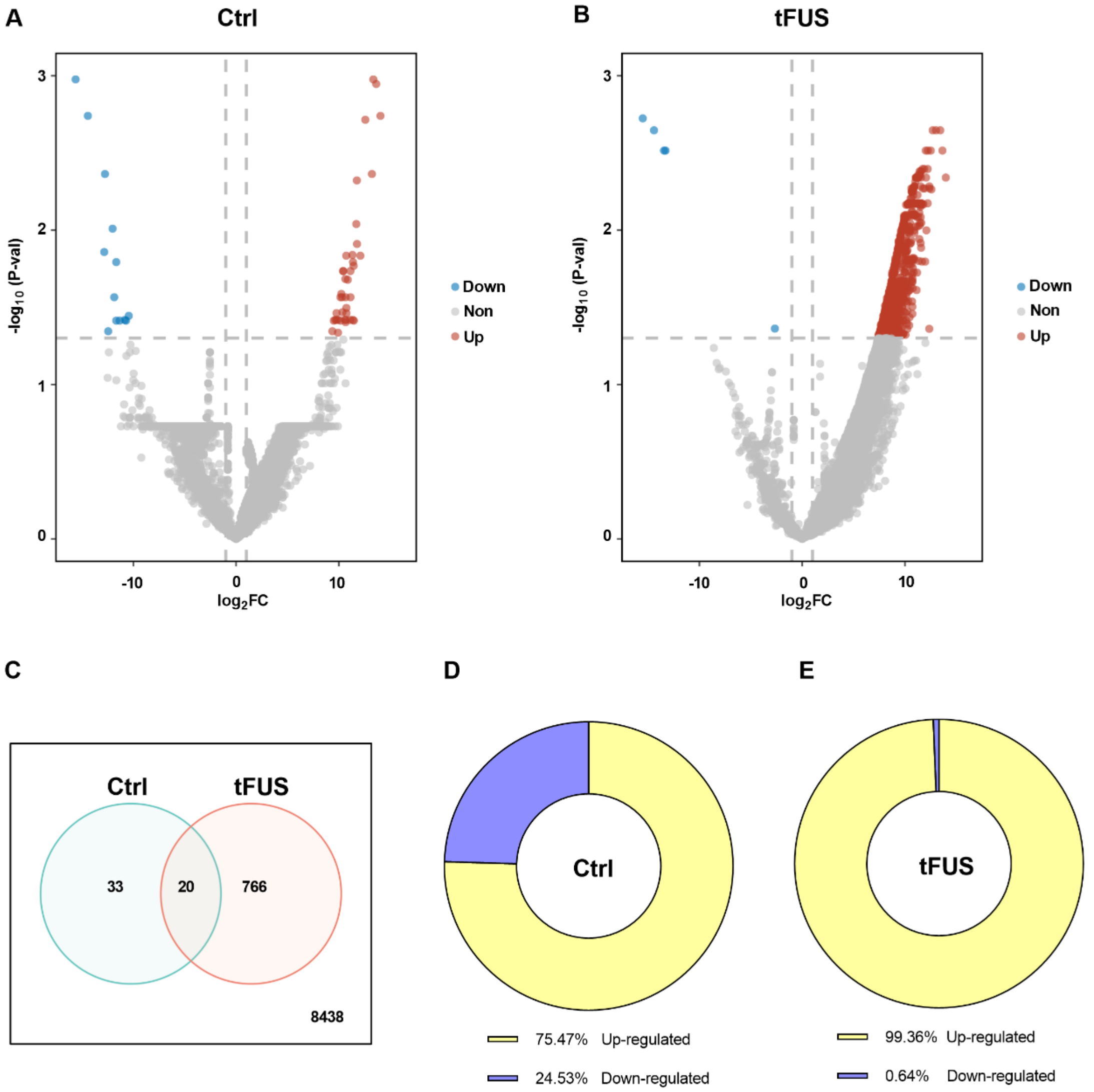

Figure 3.3.1 *DEG*s in Ctrl and tFUS sensitive cells have a remarkable difference.

(A) The volcano plot exhibits the distribution of *DEGs* in Ctrl, where red dots represent genes with a significant increase, blue dots represent genes with a significant decrease, and grey dots represent genes with no significant changes.

(B) The volcano plot exhibits the distribution of *DEGs* in tFUS, where red dots represent genes with a significant increase, blue dots represent genes with a significant decrease, and grey dots represent genes with no significant changes.

(C) The Venn diagram presents the number of *DEGs* in each sample.

(D) The pie chart exhibits the proportion of up-regulated and down-regulated *DEGs* in Ctrl.

(E) The pie chart shows the proportion of up-regulated and down-regulated *DEGs* in tFUS.

3.3.2 Screening of key genes in tFUS-activated Egr1$^+$ cells

According to our multi-channel recording results, tFUS regulated neuronal activities, which indicated that the ion channels might mediate the effects of tFUS. Intriguingly, the encoding proteins of nine upregulated *DEGs* were related to the ion transmembrane transporting (Table 3.3.2); we, therefore, paid attention to the nine genes.

Table 3.3.2 The list of encoding proteins of nine up-regulated *DEGs* related to the ion transmembrane transporting

Gene	Encoding protein	$\log_2$FC	*P*_adj
Atp5b	ATP synthase F1 subunit beta	10.119	0.038
Atp6v0d2	ATPase H$^+$ transporting V0 subunit D2	7.605	0.045
Cracr2a	Calcium release activated channel regulator 2A	9.614	0.010
Clcn5	Chloride voltage-gated channel 5	8.846	0.042
Cnga4	Cyclic nucleotide gated channel subunit alpha 4	8.305	0.045
Lrrc8a	Leucine-rich repeat containing 8 VRAC subunit A	10.652	0.016
Kcnj8	Potassium inwardly-rectifying channel subfamily J member 8	9.453	0.038
Kcnh3	Potassium voltage-gated channel subfamily H member 3	9.073	0.033
Trpc4	Transient receptor potential cation channel subfamily C member 4	9.717	0.031

We analyzed data from the mouse cortex single-cell transcriptome database (Figures 3.3.2.1A and B) (https://cells.ucsc.edu/?ds=mouse-nervous-system&gene=Sbds) (Zeisel et al., 2018). Since the RSC is part of the cerebral cortex, we used the scRNA data from the cerebral cortex of mice. Based on the expressions of the classic markers, we identified the neurons, including the glutamatergic neurons (ExN) marked as the expressions of *CaMKIIα* and *Thy1*, and the GABAergic neurons (InN) expressing *Gad1* and *Thy1*. The astrocytes (Astro) that expressed the *Gja1*, the immune cells included the microglia cells (Micro) and macrophages (Mac); both cell types expressed *Hexb*, while the Mac dominantly expresses *Pf4*. The oligodendrocytes (Oligo) and oligodendrocyte precursor cells (OPC) were identified due to the expression of *Cldn11* and the *Pdgfra*, respectively. For the cells from the vascular, we mainly identified the endothelial cells (EC) with *Cldn5*. Among the nine upregulated ion channels related to *DEGs*, we detected a high expression of *Atp5b* on nearly all cell types, minor expression of *Atp6v0d2*, *Cracr2a,* and *Cnga4*. Furthermore, the *Clcn5* and *Kcnj8* showed a dominant expression on the macrophages and EC, respectively. The *Lrrc8a* was detected on the Astro, EC, and InN. The *Kcnh3* was mainly detected on the ExN, while the *Trpc4* was on both ExN and InN (Figure 3.3.2.2). The increase in Trpc4 expression revealed that Trpc4 might play an essential role in ultrasonic neuromodulation in RSC. Our electrophysiological recording results showed that the tFUS changed the neuronal activities of both pyramidal and interneurons, which shed light that the Trpc4 was one of the targets of tFUS.

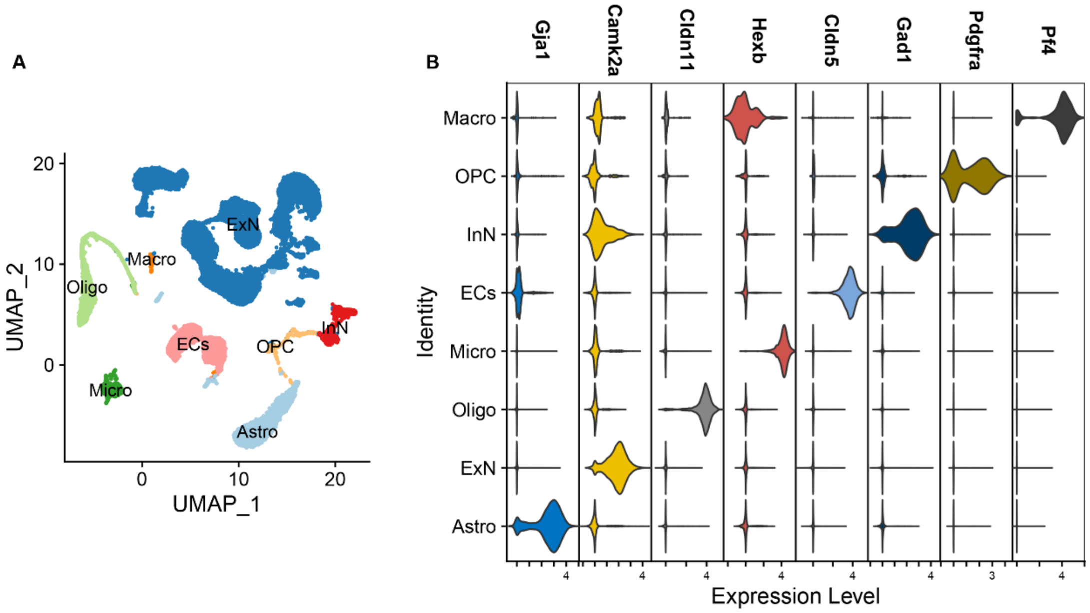

Figure 3.3.2.1 Cell classification from the mouse cortex single-cell transcriptome database.

(A) Visualization of main classes of cells using UMAP (uniform manifold approximation and projection).

(B) Violin plot exhibits the distribution of expression of selected marker genes across all eight cell types.

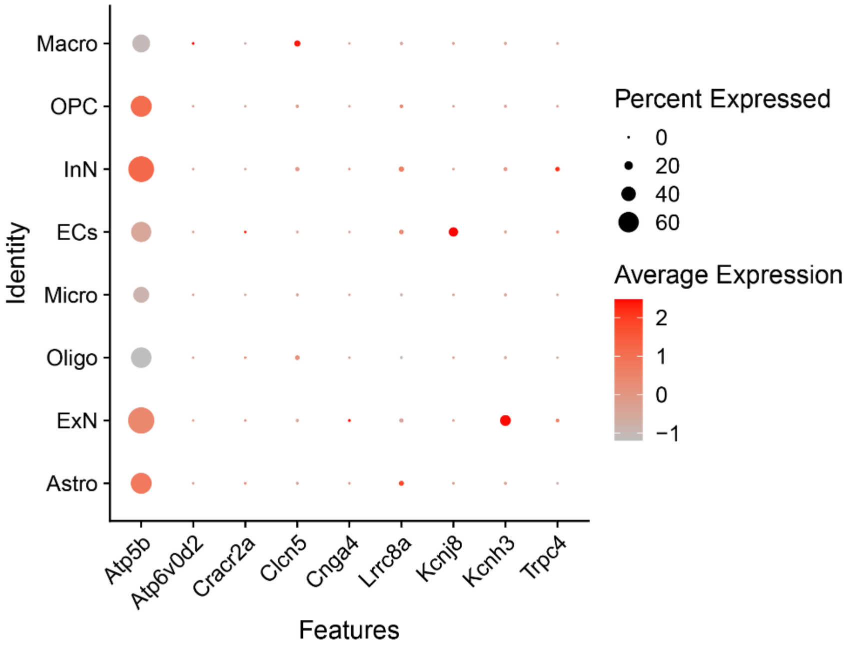

Figure 3.3.2.2 Dot plot shows the expression of nine up-regulated *DEGs* in different cell types.

3.3.3 Effect of tFUS on Trpc4

In order to explore the effect of tFUS on Trpc4, we used Fluo-4 fluorescent probe to detect the intracellular calcium concentration of Trpc4 cells induced by tFUS because Trpc4 is permeable to calcium ions (Vazquez et al., 2004). Interestingly, the fluorescent intensity of Trpc4 cells was dramatically changed by ultrasound stimulation, while the fluorescent signal of the control cells was not significantly changed (Figure 3.3.3A). Moreover, after adding ML204 (10 μM) (Miller et al., 2011), a specific inhibitor of Trpc4, and an IC_{50} value of 0.96 μM, ultrasound could not cause any changes in the fluorescent intensity of

Trpc4 cells (Figure 3.3.3B). After ultrasound stimulation, the signal in the Ctrl group fluctuated, which was the background fluctuation of red fluorescence, and this signal also existed in the Trpc4 group. Therefore, we preliminarily concluded that tFUS could open the Trpc4 channel. The patch-clamp recording was performed in inside-out mode (Figure 3.3.3C). The current of Trpc4 cells increased significantly under ultrasound stimulation compared with Ctrl. This phenomenon was suppressed by ML204 (Figures 3.3.3D and E).

Therefore, our results demonstrated that the Trpc4 could be controlled by ultrasound stimulation.

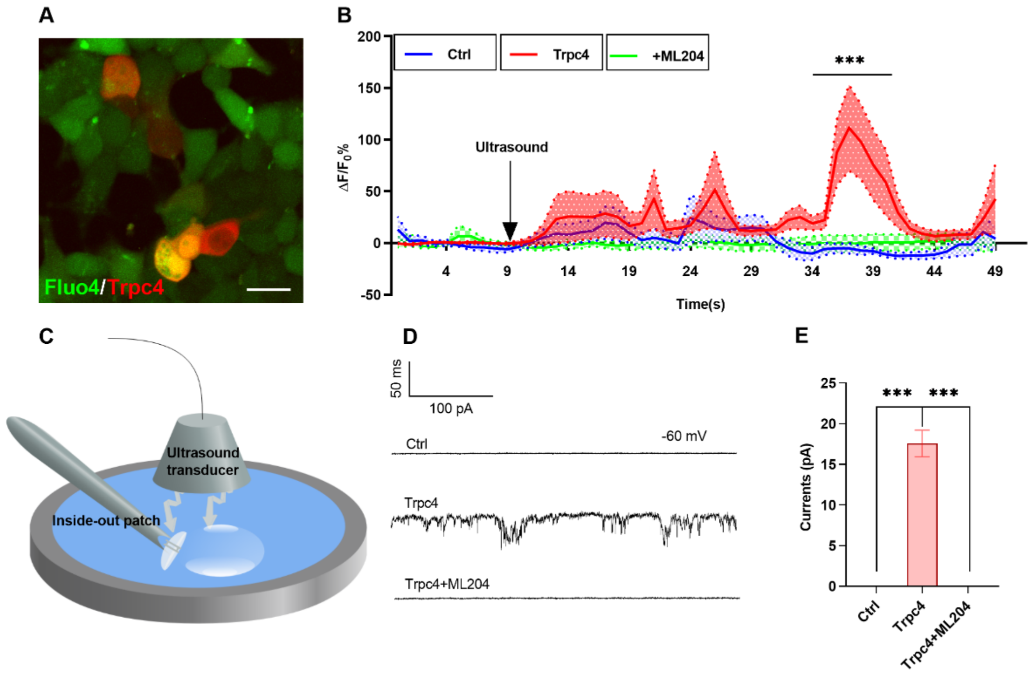

Figure 3.3.3 Trpc4 is an ion channel responding to tFUS.

(A) An example cell diagram shows the expression of the Trpc4-RFP plasmid and the calcium dye Fluo-4 in HEK-293T cells with a scale of 20 μm.

(B) Line chart displays fluorescent intensity (ΔF/F%) in calcium imaging experiment; the blue line represents the Ctrl group, the red line represents the tFUS group, and the green line represents the ML204 (10 μM) group. In order to avoid cell drifting caused by ultrasonic stimulation, Ctrl, Trpc4, and ML204 groups received ultrasound from 10 to 20 s and from 30 to 40 s, and there was no ultrasound during other periods. The resonant frequency of the ultrasonic probe was 0.74 MHz. The stimulation system produced an ultrasonic pulse stimulation with a sound pressure of 214 kPa (100% amplitude) every 3 s and lasted 2 min through a head-mounted stimulator. The pulse duration was 0.5 ms, the pulse repetition time was 1 ms, and the stimulation duration was 300 ms.

Two-way repeated measures ANOVA, interaction, $F_{(98,\ 833)}$ = 1.718, P < 0.0001; different time points, $F_{(3.298,56.06)}$ = 1.412, P = 0.2469; different treatments, $F_{(2,17)}$ = 7.106, P = 0.0057; n (Ctrl) = 5, n (tFUS) = 8, n (tFUS+ML204) = 7.

(C) The pattern diagram shows electrophysiological recording in inside-out mode with tFUS. The ultrasonic stimulator with a resonant frequency of 0.74 MHz was installed on the side of the cell culture dish, and the ultrasonic probe was immersed in the bath above the recorded cells. The pulsed ultrasonic stimulator performed pulsed ultrasonic stimulation every 3 s for 5 min at a sound pressure of 214 kPa (25% amplitude). The pulse duration was 0.5 ms, the pulse repetition time was 1 ms, and the stimulation duration was 300 ms. Ctrl, Trpc4, and ML204 groups received ultrasonic stimulation throughout the recording.

(D) The representative trace diagram exhibits the current value recorded by Ctrl, tFUS, and ML204 (10 μM)c, and the holding potential is -60 mV.

(E) The bar chart shows the current values recorded in Ctrl, tFUS, and ML204 groups. One-way ANOVA, $F_{(2,19)} = 3.486$, $P < 0.0001$; n (Ctrl) = 5 patches from 3 cell cultures, n (tFUS) = 12 patches from 4 cell cultures, n (tFUS+ML204) = 5 patches from 3 cell cultures. All data are means ± s.e.m.; $^{***}P < 0.001$.

3.3.4 The role of Trpc4 in tFUS regulation of pain sensation in mice

We already knew that the Trpc4 could be modulated by ultrasound stimulation. Then, we wanted to know what role Trpc4 played in tFUS regulation of pain sensation.

Firstly, the expression of Trpc4 protein was detected in the RSC of Egr1-GFP mice by immunofluorescent staining. The proportion of Egr1 cells ($Egr1^+/Trpc4^+$) and non-Egr1 cells ($Egr1^-/Trpc4^+$) was calculated. It was found that tFUS acting on RSC increased the ratio of $Egr1^+/Trpc4^+$ cells (Figures 3.3.4A and B), with nearly 70% of $Egr1^+$ cells co-expressing Trpc4. In the Ctrl group, the ratio of $Egr1^-/Trpc4^+$ and $Egr1^+/Trpc4^+$ was similar without marked change, which indicated that tFUS elevated the expression of Egr1 in Trpc4 cells.
Subsequently, mice were treated with ML204 (2 mg/kg, twice a day, for five

consecutive days, intraperitoneal injection) (Pereira et al., 2018) to inhibit Trpc4 activity. The results showed that tFUS could not increase PWT (Figure 3.3.4C) or prolong TWL (Figure 3.3.4D) in the ML204 group, while tFUS still increased PWT and prolonged TWL in the solvent group. Similarly, immunofluorescent staining results exhibited that, compared with the solvent group, tFUS did not notably change the ratio of Egr1$^+$ cells under ML204 (Figures 3.3.4E and F). In summary, Trpc4 controlled the response of Egr1 cells to tFUS.

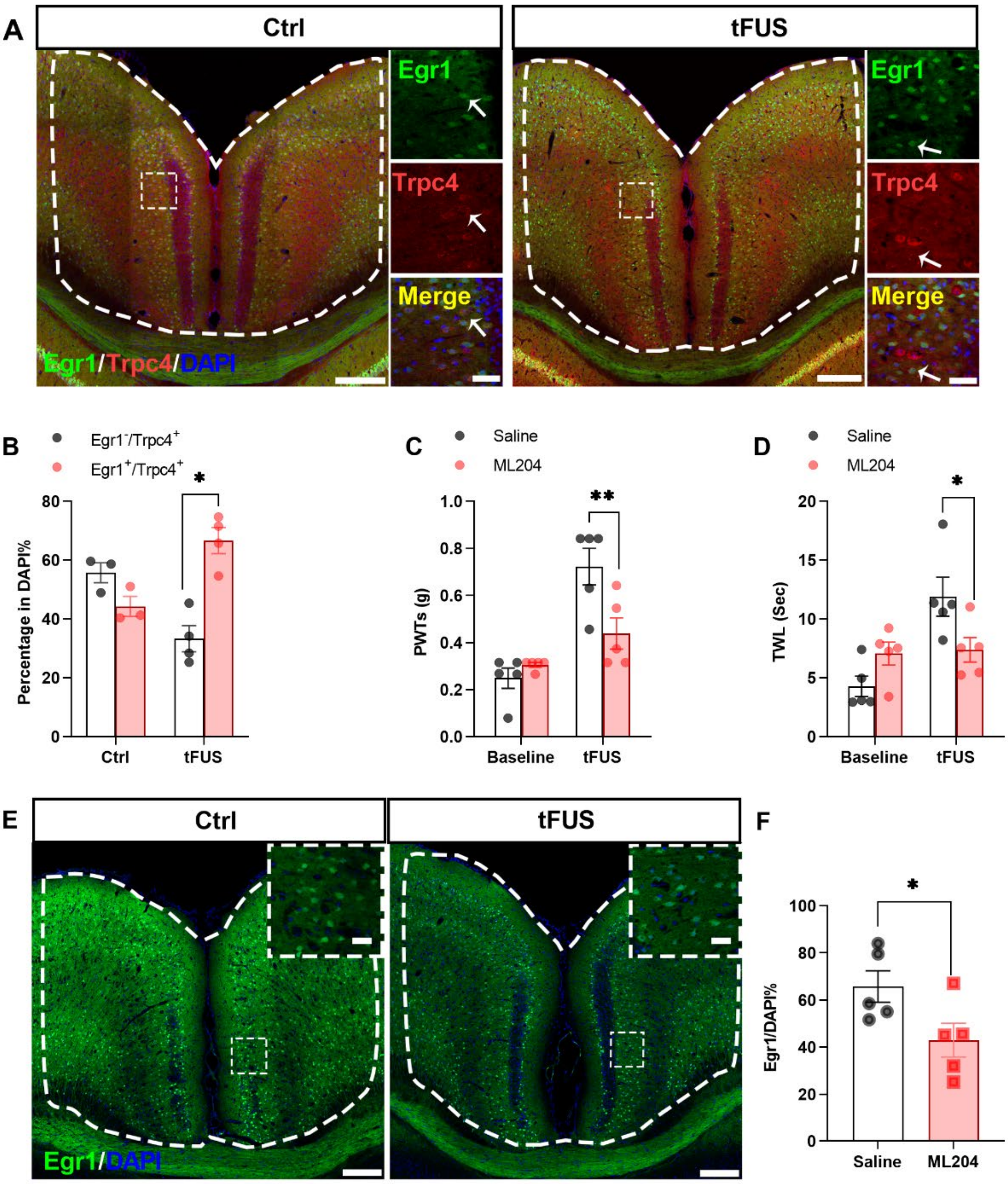

Figure 3.3.4 Trpc4 controls the response of Egr1 cells to tFUS.

(A) tFUS stimulation of RSC increases the ratio of Egr1$^+$ in Trpc4$^+$ cells. Sample image of ultrasound-activated co-localization of Egr1 and Trpc4 in RSC (overall image scale 200 μm, magnified local image scale 20 μm).

(B) In Trpc4 positive cells, the proportion of Egr1 cells (Egr1$^+$/Trpc4$^+$) and non-Egr1 cells

($Egr1^-/Trpc4^+$). Two-way repeated measures ANOVA, interaction: $F_{(1, 5)} = 14.08$, $P = 0.0133$; $Egr1^-/Trpc4^+$ *vs.* $Egr1^+/Trpc4^+$: P *(Ctrl)* = 0.4529, P *(tFUS)* = 0.0159, n (Ctrl) = 3, n (tFUS) = 4.

(C) ML204 (2 mg/kg) inhibits the activity of Trpc4 and influences the PWT induced by tFUS. Two-way repeated measures ANOVA, $F_{(1,8)} = 8.94$, $P < 0.05$, n = 5 per group.

(D) ML204 (2 mg/kg) inhibits the activity of Trpc4 and influences the TWL induced by tFUS. Two-way repeated measures ANOVA, $F_{(1,8)} = 39.92$, $P < 0.001$, n = 5 per group.

(E) Representative diagrams exhibit Egr1 expression after tFUS acting on RSC in the saline group and ML204 group (overall image scale 200 μm, magnified local image scale 20 μm).

(F) Expression ratio of $Egr1^+$ cells after ML204 inhibits Trpc4 activity in RSC. Unpaired *t*-test, $t = 2.33$, $P < 0.05$, n = 5 per group.

All data are means ± s.e.m., $^*P < 0.05$; $^{**}P < 0.01$.

3.3.5 Specifically inhibiting the effects of Trpc4 on tFUS regulation of neuronal activity and pain threshold

According to our transcriptomic sequencing results, we can confirm that Trpc4 was mainly expressed in neurons. To further confirm the effect of tFUS on pain regulation after knockdown (KD) of Trpc4 expression, we used the AAV virus of Trpc4-shRNA to knock down Trpc4 in RSC neurons (Figures 3.3.5.1A and B).

The results were consistent with those of ML204. tFUS increased PWT and prolonged TWL in the scramble virus group but did not change PWT and TWL in the Trpc4 shRNA group (Figures 3.3.5.1C and D). Subsequently, we examined the effect of Trpc4 knockdown on RSC neuron activity. Scramble shRNA had no effect on the percentage of continuous decline in neuron activity after tFUS application, however, knocking down Trpc4 significantly reduced the percentage of continuous decline in pyramidal neurons and interneurons activity (pyramidal neurons: scramble, n = 19, decreased by 37%, Trpc4 KD, n = 17, decreased by 24%, *P* = 0.04; interneuron: scramble, n = 25, decreased by 52%; Trpc4 KD, n = 12, decreased by 17%, *P* < 0.001; Fisher's exact test). In addition, pyramidal neurons (scramble, n = 25, increased by 16%; Trpc4 KD, increased by 12%, n = 12, Fisher's exact test, *P* = 0.54) and interneurons (scramble, increased by 4%; Trpc4 KD, increased by 17%, Fisher's exact test, *P* = 0.08) showed no change in the percentage of continuously increased activity (Figures 3.3.5.2A to C). Therefore, we summarized that the expression of Trpc4 was necessary for tFUS to regulate the continuous decline of RSC neuron activity, especially in interneurons, thus affecting the regulation of tFUS on pain sensation.

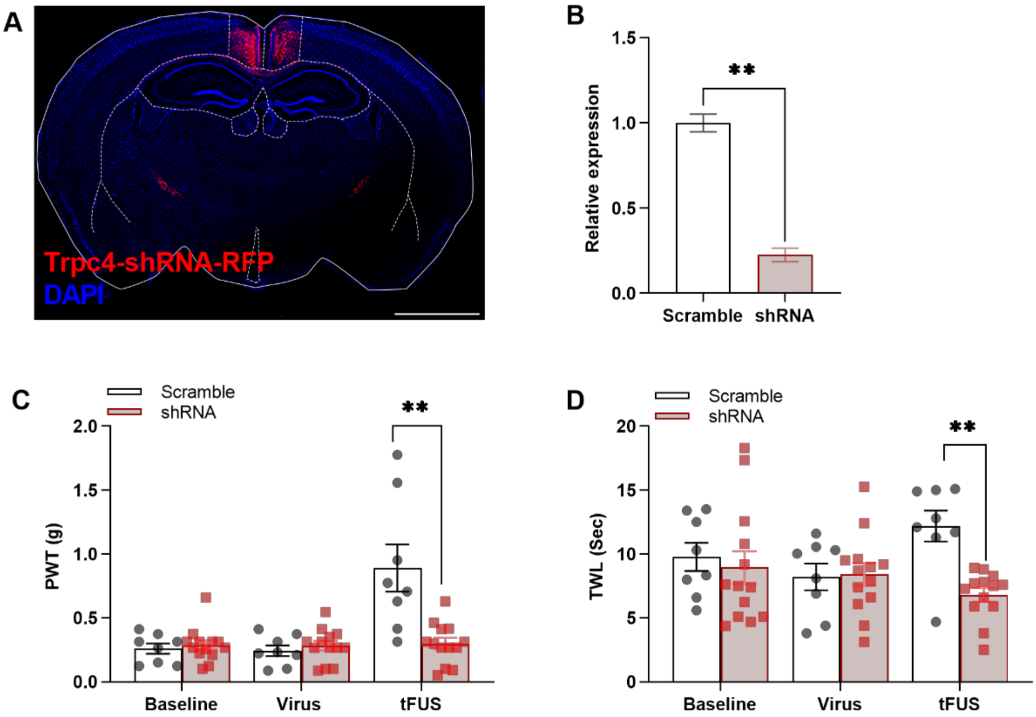

Figure 3.3.5.1 Specific inhibition of Trpc4 blocks tFUS regulation of pain sensation.

(A) Schematic diagram of Trpc4-shRNA-RFP virus expression in RSC with a 2 mm scale.

(B) Trpc4 shRNA knocks down *Trpc4* expression. Unpaired *t*-test, $t = 11.87$, $P = 0.0003$, n = 3 per group.

(C) Effects of tFUS on PWT after shRNA knocking down Trpc4 expression. Two-way repeated measures ANOVA, $F_{(2, 38)} = 12.21$, $P < 0.0001$, n (scramble) = 8, n (Trpc4 shRNA) = 13.

(D) Effects of tFUS on TWL after shRNA knocking down Trpc4 expression. Two-way repeated measures ANOVA, $F_{(2, 38)} = 3.76$, $P < 0.05$, n (scramble) = 8, n (Trpc4 shRNA) = 13.

All data are means ± s.e.m., $^{**}P < 0.01$.

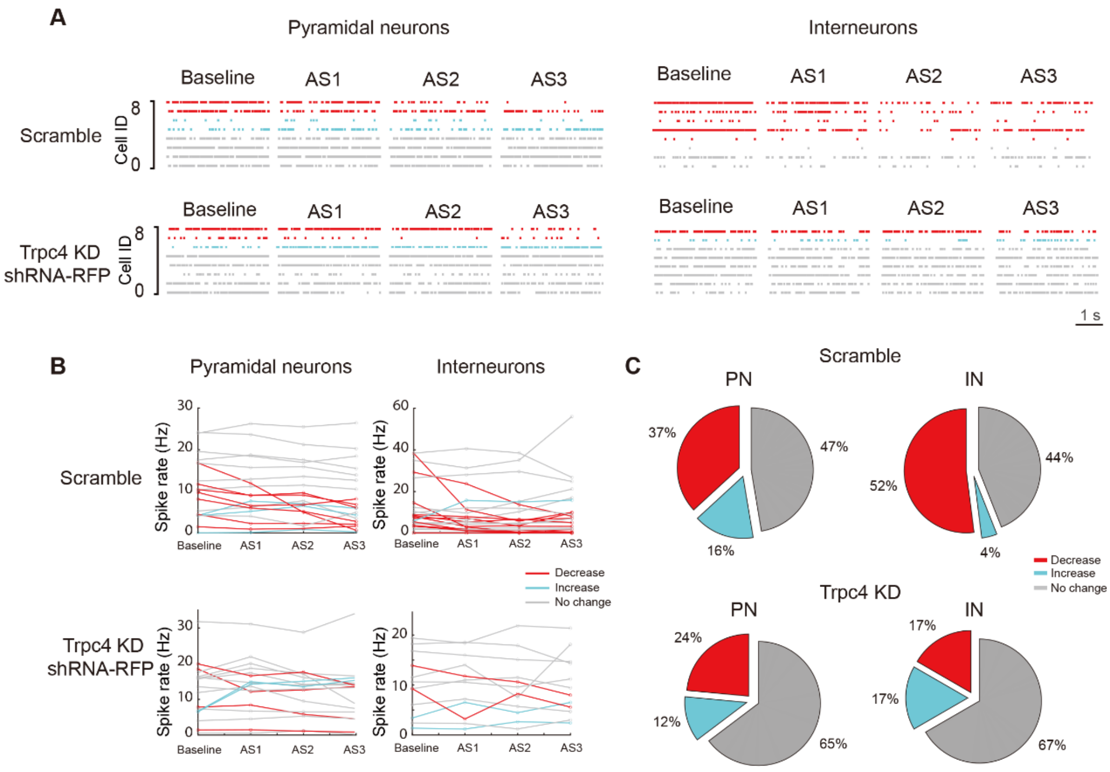

Figure 3.3.5.2 Knockdown of Trpc4 remarkably reduces tFUS-induced sustainedly decreasing RSC neurons' activity.

(A) Rasters plots for pyramidal neurons (PNs) (left) and interneurons (INs) (right) during baseline, AS1, AS2, AS3 periods after expression of Trpc4 knockdown (bottom) and scramble (top) shRNA.

(B) Trpc4 knockdown reducing the number of tFUS-induced decreasing spike firing rate after stimulation both in PNs (left) and INs (right).

(C) Trpc4 knockdown reducing the percentage of tFUS-induced decreasing spike firing rate after stimulation both in PNs (left) and INs (right) (PN: scramble, n = 19 neurons, 37% decreasing, Trpc4 KD, n = 17 neurons, 24% decreasing, Fisher’s exact test, *P* = 0.04; IN: scramble, n = 25 neurons, 52% decreasing, Trpc4 KD, n = 12 neurons, 17% decreasing, Fisher's exact test, $P < 0.001$).

3.4 Discussion

Ultrasonic neuromodulation is a non-invasive neural regulation technology widely studied in recent years, mainly focusing on the ultrasonic regulation of ion channels and somatosensation-relating behaviour. However, there is a rupture between these two research fields, which has not been connected. Moreover, the ultrasonic neuromodulation mechanism has not been established. Therefore, we boldly hypothesized that tFUS-activated ion channels might play an essential role in tFUS-induced changes in somatosensation. In order to solve such problems, this study mainly explored the cellular mechanism of ultrasonic neuromodulation.

Our study found that tFUS acted on RSC, induced remarkable changes in neuronal activity, and behaviourally altered pain threshold in mice, accompanied by changes in transcription level and protein level of Egr1. These Egr1$^+$ cells played an essential role in the analgesic effect of tFUS. Based on Egr1-GFP cells RNA-seq, we identified Trpc4, mainly expressed in neurons. Trpc4 also controlled the response of Egr1$^+$ cells to tFUS. Trpc4, as a critical factor in the neuronal regulation of tFUS, will provide a new strategy for the noninvasive treatment of chronic pain.

3.4.1 Different parameters of ultrasound had different effects

Different ultrasonic parameters affect the ultrasonic neuromodulation outcomes. The ultrasonic parameters closely affected the ultrasonic intensity, and stimulus effects include the amplitude of sound pressure, the duration of ultrasonic stimulation T_3, the duration of stimulus repetition T_4, the duty cycle, and the pulse repetition frequencies ($1/T_2$) (G. Li et al., 2019). Those ultrasonic parameters have been optimized by my cooperators, who invented the ultrasonic neuromodulation system (G. Li et al., 2019; Qiu et al., 2017). However, due to the mechanical induction, ultrasonic absorption in the target increases temperature, which may lead to thermo-neuromodulation. In order to avoid the thermal effects (Blackmore et al., 2019) of tFUS, the ultrasonic amplitude, T_2, and T_3 remained constant and just changed the duration of stimulus repetitions of tFUS (T_4). The results showed that PWT and TWL were significantly increased when the T_4 was 3 s rather than 1.5 s or 10 s. 1.5 s, 3 s, and 10 s of T_4 had varying spatial-peak, temporal-averaged intensity (I_{SPTA}), which reflected the intensity averaged over the total experimental time and the optimal measured amount of heat transferred to tissue by ultrasound. The I_{SPTA} of 10-second-T4 was 22.9 mW/cm^2, which was too weak to alter behavior. The

I_{SPTA} of 1.5-second-T4 was 152.9 mW/cm^2, the strongest intensity among those candidate parameters; however, it could not change the pain threshold. The I_{SPTA} of 3-second-T4 was 76.4 mW/cm^2, and this intensity could significantly elevate the pain threshold. Therefore, we could know that the change of pain threshold regulated by tFUS was not a linear change with the increase of ultrasonic intensity.

3.4.2 tFUS regulated somatosensation by acting on RSC

Previous reports showed that low-intensity and high-intensity focused ultrasound targeted L5 dorsal root ganglion (DRG) significantly reduces nociceptive sensitivity thresholds without causing tissue damage in neuropathic pain rodents (Hellman, Maietta, Byraju, Park, et al., 2020; Y.-F. Lee et al., 2015; Liss et al., 2021; Prabhala et al., 2018). Compared with previous studies using ultrasound to modulate pain, it was the first time that the pain threshold dramatically changed when tFUS acted on the pain-related cortical subregion RSC. Interestingly, both PWT and TWL were remarkably elevated in neuropathic pain mice when tFUS was applied to RSC.

In order to confirm the target-specificity of tFUS, tFUS was applied to different brain regions, and associated ethological tests were conducted. RSC and ACC closely relate to pain; when tFUS acted on them, the PWT and TWL of mice were significantly altered. M1 is not part of the pain network (Castillo Saavedra et al., 2014); tFUS acting on M1 had no remarkable impact on the pain sensation but could markedly change the motor ability of mice.

Next, we wanted to know what happened in brain regions where tFUS acted. Subsequently, we detected the expression of *IEG, c-Fos,* and *Egr1*, which reflected cellular activity after tFUS treatment with RSC. The results showed that both transcription and protein expression of Egr1 was significantly increased, and the marked difference lasted for 2 hr. However, c-Fos was only dramatically increased at the transcriptional level, without a change in protein level. In addition to RSC, ACC and M1 were also detected at the transcriptional level. After tFUS treatment, *Egr1* in both ACC and M1 was remarkably increased, but *c-Fos* was only increased in ACC, and there was no marked change in M1. Therefore, it was clear that Egr1 is more sensitive to tFUS, and tFUS targets brain regions selectively.

In subsequent experiments, we mainly focused on RSC. In order to determine the cell types of tFUS-responsive cells, we detected the colocalization of Egr1^{+} cells with marker genes related to cell types. We found that most Egr1 cells were co-labeled with the marker protein NeuN of neurons in the RSC. Here, we could know that tFUS mainly acts on neurons in the RSC. To determine whether tFUS acted directly on neurons in the RSC or indirectly regulated the sensory pathway (Mohammadjavadi et al., 2019), we applied tFUS to the RSC of born deaf (Cdh23) mice. We found that both PWT and TWL were remarkably increased, and the number of Egr1 neurons was also dramatically elevated by tFUS in Cdh23. At the same time, the activity of pyramidal neurons and interneurons in the RSC was significantly changed by multi-channel in vivo recordings under tFUS. The above results suggest ultrasonic stimulation directly regulates neuronal activity rather than indirectly.

Next, we were curious about the effect of ultrasound-activated Egr1$^+$ cells in tFUS neuromodulation. Therefore, using a TRAP system that could precisely control the activity of neurons (Tasaka et al., 2020). Explicitly inhibiting ultrasound-activated Egr1$^+$ cells, the analgesic effect of tFUS was blocked. We confirmed that tFUS-activated Egr1$^+$ cells play an essential role in ultrasonic neuromodulation.

Collectively, tFUS has site-specificity and directly activates RSC cells to elevate the pain threshold. Also, Egr1 can be used as a marker in response to tFUS.

RSC could process noxious information, respond to nociceptive stimuli in pain neural circuits, and participate in the inhibitory mechanisms of pain reduction. Concerning the potential circuit of RSC regulating spinal reflex withdrawal behaviours, both retrograde and anterograde tracing techniques were used to explore the afferent and efferent connections of RSC (Quintero, 2013; T van Groen & Wyss, 1990; Thomas van Groen & Wyss, 1992; Thomas Van Groen & Wyss, 2003). According to retrograde and anterograde tracing results, there is a descending interconnection between RSC and periaqueductal gray (PAG), and PAG functions as central pain control. The PAG sparsely projects to the spinal cord but densely projects to the rostral ventromedial medulla (RVM), which further projects to the dorsal horn by the dorsolateral side of the spinal cord. Also, non-selective activation of the neurons in the PAG-RVM modulatory network produces an antinociception effect (Heinricher & Ingram, 2008; Quintero, 2013). Taken together, RSC could project to PAG, activate PAG-RVM modulatory network and project to the spinal cord, and regulate spinal reflex withdrawal behaviours.

3.4.3 Trpc4 was essential for the regulation of ultrasound in vitro and in vivo

We found that tFUS directly regulated the activity of $Egr1^+$ cells in RSC, and these $Egr1^+$ cells were mainly co-located with the neuron marker NeuN, which indicates that tFUS may regulate the activity of Egr1 neurons in RSC. We also used multi-channel in vivo recording to confirm this result. Both pyramidal neurons and interneurons were significantly changed by tFUS.

We also fully proved that Egr1 was a cellular marker for tFUS-induced response in RSC. RSC of Egr1-GFP mice was stimulated by tFUS, and these tFUS-activated Egr1-GFP cells were selected by flow cytometry for transcriptional sequencing. The results showed that 786 *DEGs* were found in Egr1-GFP cells of the tFUS group. There were only 53 *DEGs* in Egr1-GFP cells of the Ctrl group, and only 20 *DEGs* were expressed in both Ctrl and tFUS, which further proved that Egr1 could indeed be used as a marker for tFUS responsive cells.

Based on transcriptome sequencing results of Egr1-GFP cells, we detected multiple up-regulated *DEGs* related to the ion transmembrane transporting in response to ultrasound, mainly including *Atp5b, Atp6v0d2, Cracr2a, Clcn5, Cnga4, Lrrc8a, Kcnj8, Kcnh3, and Trpc4*. The reason why we chose those genes is that several studies have found that tFUS activated ion channels, including the two-pore potassium ion channel family (Kubanek et al., 2016), TREK-1 (KCNK2), TREK-2 (KCNK10), and TRAAK (KCNK4), $Na_{V1.5}$ (Scn5a) (Kubanek et al., 2016), Piezo1 (Liao et al., 2019; Prieto et al., 2018), MscL1 (J. Ye et al., 2018), TRPA1 (Oh et al., 2019), TRPC1, TRPP1/2 (S. Yoo et al., 2022), TRP4 (Ibsen et al., 2015), MEC4 (Kubanek et al., 2018) and MEC6 (Zhou et al., 2022). Among those ultrasound-activated ion channels, Piezo1, TRPC1, TRPP1/2, and TRPA1 were identified in the mammalian brain. Piezo1, TRPC1, and TRPP1/2 are endogenous calcium-permeable ion channels in cortical neurons which support the mechanosensitive ion channels-mediated mechanisms in ultrasonic neuromodulation (S. Yoo et al., 2022). In addition to neurons, it is also reported that ultrasound activates astrocytic TRPA1 and further modulates neuronal activity (Oh et al., 2019). All of the above shows that ion channels mediate ultrasonic neuromodulation.

The above nine selected genes were mapped to the single-cell database. Among those candidate genes, both *Kcnh3* and *Trpc4* were mainly expressed in neurons. Trpc4, or not *Kcnh3*, was selected as the study target because it could respond to mechanical stimuli (Beech, 2012; Vazquez et al., 2004), which provided the hint that Trpc4 might respond to ultrasonic stimulation. The increase in *Trpc4* expression reflected that tFUS could modulate the mRNA expression of *Trpc4*. In addition, *Trpc4* encoded ion channel might be sensitive to tFUS stimulation. The calcium imaging and patch-clamp recording results showed that tFUS could modulate the Trpc4 channel at the cellular level, and the Trpc4-specific inhibitor ML204 can prevent these changes. By colocalizing Egr1 and Trpc4, the number of Egr1 cells remarkably increased in Trpc4 cells after tFUS. The ML204 could inhibit the increment of Egr1 cells' number and eliminate the analgesic effect of tFUS. We also detected the colocalization of Trpc4 cells in tFUS-activated Egr1 cells, with about 80% of Trpc4 cells co-expressing with tFUS-activated Egr1 cells (data not shown). However, there was no direct evidence that tFUS-increased Trpc4 and Egr1 exist in the same type of cells. Trpc4 shRNA could block the analgesic effect of tFUS and eliminate tFUS-induced neuronal activity through multi-channel recording. In order to avoid the off-target effects of Trpc4 shRNA, three different shRNA sequences were designed to knock down Trpc4 and screen the most stable and effective one (shRNA-2) to conduct in vivo tests (Figure 3.4.3).

Taken together, Trpc4 controls the response of Egr1 cells to tFUS. Also, Trpc4 responds to ultrasound stimulation and plays a crucial role in ultrasonic neuromodulation. This is the first evidence that Trpc4 plays an important role in ultrasonic activation and promotes the research of ultrasonic neuromodulation.

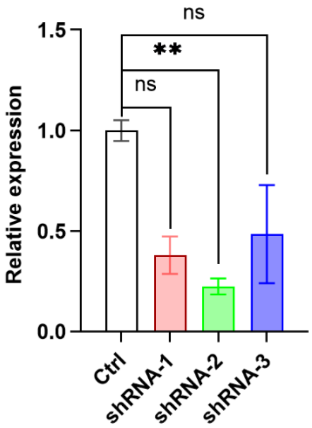

Figure 3.4.3 Screen of optimal Trpc4 shRNA.

One-way ANOVA, $F_{(3.\ 7)} = 3.88$, $P = 0.0104$; Tukey's multiple comparisons test, *P (Ctrl vs. shRNA-1)* > 0.05, *P (Ctrl vs. shRNA-2)* < 0.01, *P (Ctrl vs. shRNA-3)* > 0.05; n (Ctrl) = 3, n (shRNA-1) = 3, n (shRNA-2) = 3, n (shRNA-3) = 3.

All data are means ± s.e.m., $^{**}P < 0.01$, ns, with no significant difference.

3.4.4 Limitations and future works

There are still several limitations in this study. Firstly, we did not use different intensities of ultrasound to stimulate cells in calcium imaging and electrophysiological tests. In future work, we will use a series of parameters to explore the ultrasonic effects on cells. Secondly, we still do not know whether Trpc4 plays a direct or indirect role in ultrasonic activation. There are three criteria for direct mechanical activation (Christensen & Corey, 2007); first, the current delay caused by the stimulus should be faster than that of the known second-messenger system, usually less than 5 ms; second, the kinetics of channel activation should rely on the stimulus amplitude, which means the speed of channel opening increases with the mechanical forces strengthening; finally, the channel gating should have a mechanical correlate, for example, the movement or change of mechanical force can be detected in sensory cells or organs within the same stimulus range of the channel opening. Based on the above criteria, Trpc4 might be indirectly activated by tFUS because the current delay of Trpc4 caused by tFUS was slower than the known second-messenger system. It is necessary to confirm this further by detecting the kinetics of channel activating and the mechanical correlate of channel gating.

Chapter 4 tFUS induced transcriptomic changes in RSC

4.1 RSC single-cell transcriptome atlas

In order to understand the changes in brain cells after tFUS, single-cell RNA-sequencing (scRNA-seq) was used to map RSC single-cell transcriptome atlas.

4.1.1 Cell classification of RSC

First, single cells in the RSC of tFUS stimulated and non-stimulated mice were isolated for transcriptomic sequencing (Figure 4.1.1A). In strict accordance with the quality control procedure of sampling, 28,704 single cells were collected from the RSC (Ctrl: 4 mice; tFUS: 4 mice). Then, the transcriptome data obtained were grouped into 33 cell populations for cluster analysis, and the cell populations containing only one group of cells were removed. A total of 19,185 single cells were obtained for subsequent analysis (Ctrl 1: 8,064; Ctrl 2: 4,477; tFUS 1: 3,743; tFUS 2: 2,896 cells), and 26 cell populations were obtained. Based on the results of SingleR (Single-cell recognition of cell types) and the expression of classic marker genes (Ximerakis et al., 2019), all cells were divided into nine main cell types (Figures 4.1.1B and C), including 17.5% microglia (Micro) mainly expressed *Cx3cr1*; 9.52% of astrocytes (Astros) mainly expressed *Gja1*; *Cldn11* was mainly expressed in 18.48% of oligodendrocytes (Oligos); 8.88% oligodendrocyte precursor cells (OPCs) mainly expressed *Pdgfra*; 8.92% of the neurons expressed *calmodulin-dependent protein kinase*

Ⅱα (CaMKⅡα), which was defined as *CaMKⅡα*$^{+}$ cells; *glutamic acid decarboxylase (GAD) 1 and 2 (GAD1 and GAD2)* were highly expressed in 2.62% of the two groups of cells, which were collectively defined as *GAD1*$^{+}$ cells; in addition, 29.36% of endothelial cells (ECs) were identified with high expression of *Cldn5*; 1.62% pericyte (Pcy) with high expression of *Kcnj8*; *Acta* was highly expressed in 3.09% vascular smooth muscle cells (vSMCs).

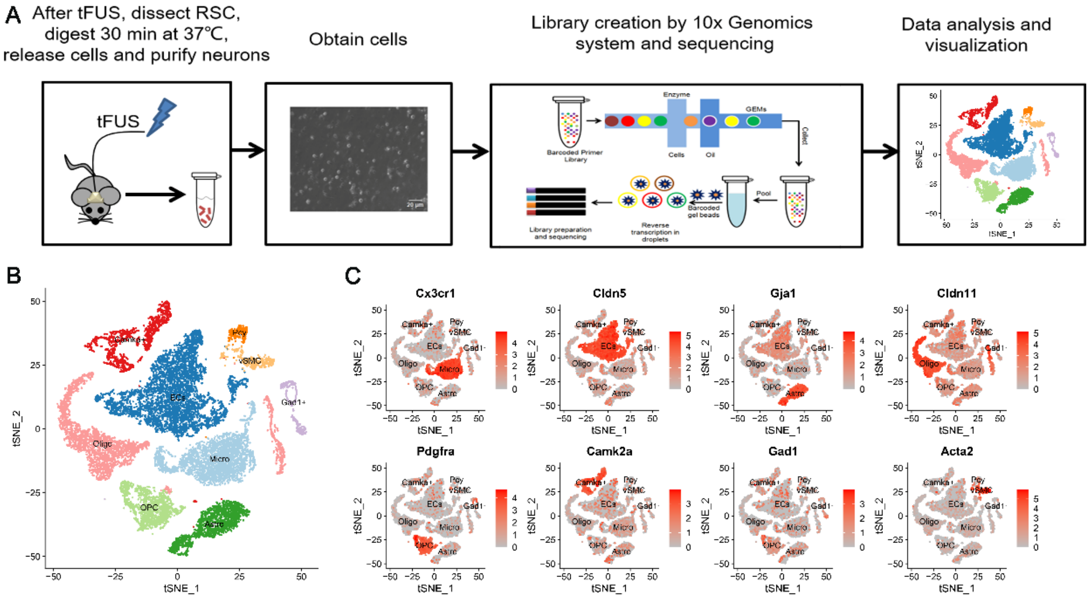

(A) Flow chart of single-cell transcriptome sequencing.

(B) *t*-SNE visualization of nine cell types in RSC.

(C) *t*-SNE visualization corresponding to characteristic marker genes of different cell types.

4.1.2 Glial cell classification in RSC

Glia cells in the CNS include microglia, astrocytes, oligodendrocytes, and oligodendrocyte precursor cells (Jäkel & Dimou, 2017). In the classification of glia cells in RSC, all microglia populations highly expressed *Hexb* and *Ctss*.

Cx3cr1 and *Lpcal2* were highly expressed in microglia cluster 1 (MC1) and microglia cluster 2 (MC2) compared with microglia cluster 3 (MC3) (Figure 4.1.2A). Due to their high expression of *P2ry12* (Figure 4.1.2B), MC1, MC2, and MC3 belonged to homeostasis microglia (Q. Li et al., 2019). Moreover, macrophages (Macs) showed high expression of *Lyz2* (Figure 4.1.2B) and *Apoe*. The two populations of astrocytes differed in the expression of some genes, such as *Mt1* and *Mt3*. *Clu* was mainly expressed in astrocyte 1 (Astro1) (Figure 4.1.2B), but *Gria2* (Figure 4.1.2B) and *Gm3764* were highly expressed in astrocyte 2 (Astro2). Two subtypes of oligodendrocyte precursor cells mainly expressed *Pdgfra* and *Cspg4* (Marques et al., 2016) (Figure 4.1.2C). Differentiation-committed oligodendrocyte precursor cells (COPs) were identified by expressing *Bmp4* (Figure 4.1.2D). Newly formed oligodendrocyte (NFOL) eminently expressed *Tcf7l2* at the early stage of differentiation (Figure 4.1.2D). In addition, four-cell populations mainly expressed *Mal*, and two of them highly expressed *Trf* (Figure 4.1.2D) and *Pmp22* (MFOL1 and MFOL2), indicating that these were two myelin cell types. In addition, there were two types of mature oligodendrocyte (MOL), MOL1 and MOL2, which mainly expressed *Trf* (Figures 4.1.2C and D).

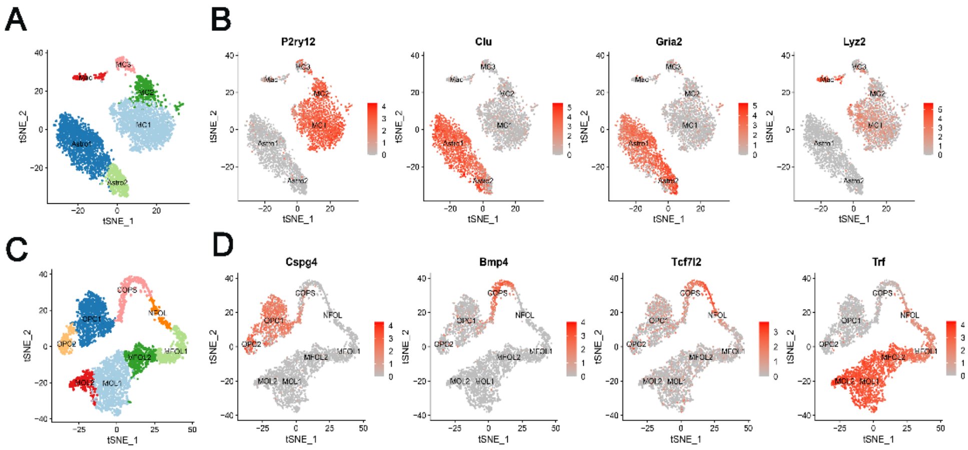

Figure 4.1.2 Classification of glial cells in RSC.

(A) *t*-SNE visualization of microglia (MC) and astrocytes (Astros).

(B) Two-dimensional *t*-SNE visualizes cell classification of *P2ry12*, *Clu*, *Gria2*, and *Lyz2* in MC and Astros.

(C) *t*-SNE visualization of oligodendrocytes (Oligos) and oligodendrocyte precursor cells (OPCs).

(D) *t*-SNE visualization of differentially expressed marker genes in Oligos and OPCs.

4.1.3 Classification of neurons in RSC

Neurons (Neus) of RSC were divided into four cell types according to marker genes *Meg3* and *Thy1*, namely Neu1, Neu2, Neu3, and Neu4 (Figure 4.1.3A). Neu1, Neu2, and Neu4, with high expression of *CaMKⅡα* and *Slc17a7,* were glutamate neurons. Neu3 was a gamma-aminobutyric acid neuron (Figure 4.1.3B) because it mainly expressed *Gad1* and *Gad2*. The symbolic genes with high expression in Neu1 included *Rnf152m*, *Camta1,* and *Cit*. Unlike Neu1, Neu2 highly expressed *Rasgrp1*, *Lmo4*, *Nlgn1,* and *Grin2a*. Meanwhile, the major *DEGs* of Neu4 were *Calm1* and *Stmn3*.

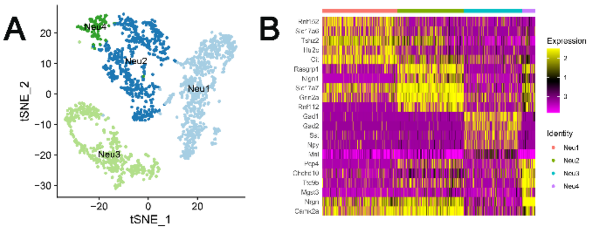

Figure 4.1.3 Neuron (Neu) classification in RSC.

(A) *t*-SNE visualization of Neu in RSC.

(B) Heat map shows the primary *DEG* in Neu subtypes.

4.1.4 Cell classification of blood vessels and associated vascular cells in RSC

There are arteries, capillaries and veins in the CNS (Vanlandewijck et al., 2018). The vascular system mainly comprises ECs and mural cells. The mural cells are, in general, terms of pericytes (Peris) and vascular smooth muscle cells (vSMCs) (He et al., 2018). The analysis found that marker genes for arterial EC, such as *Stmn2* and *Gkn3*, were detected in different EC cell populations (Figure 4.1.4A), such as EC2, EC6, and EC7 subtypes (Kalucka et al., 2020). The well-known vein marker genes *Slc38a5* and *Cfh* were mainly expressed in EC1, EC3, and EC5. The primary artery marker gene *Vwf* was expressed in the arteries (EC7) and veins (EC3 and EC5), indicating that EC7 cells were mainly from the major arteries, and EC3 and EC5 cells were mainly from the prominent veins. Except for EC7, capillary-marker genes *Mfsd2a* and *Rgcc* were highly expressed in all five EC types. In addition, capillary vascular marker genes *Tgfb2* and *Glul* were highly expressed in EC2 and EC6, while capillary vascular marker genes *Tfrc* and *Car4* were mainly expressed in EC1, EC3, and EC6 (Figure 4.1.4B).

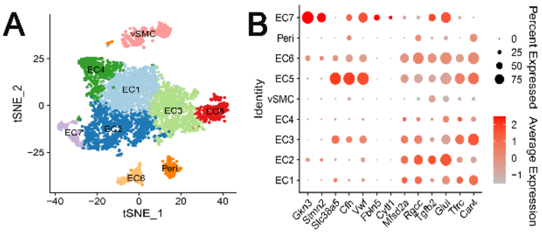

Figure 4.1.4 Classification of blood vessels and vascular-associated cells in RSC.

(A) Two-dimensional visualized *t*-SNE cell classification of endothelial cell (EC), pericyte (Peri), and vascular smooth muscle cell (vSMC).

(B) Dot plots of expression of different marker genes in EC, Peri, and vSMC.

4.2 tFUS caused cell-specific transcriptome changes

Based on single-cell transcriptomic sequencing of RSC, we analyzed *DEGs* between Ctrl and tFUS using Seurat's FindMarkers function. The volcano plot (Figure 4.2A) shows the differential distribution of gene expression levels between *CaMKⅡα*$^+$ cells in the Ctrl and tFUS groups. The red dots represent significantly up-regulated genes, the blue dots represent significantly down-regulated genes, and the grey dots represent genes with no significant changes. Some markedly changed genes were significantly altered in other cell types, not only in *CaMKⅡα*$^+$ cells. For example, *zinc finger and BTB domain containing 20 (Zbtb20)* were dramatically up-regulated in *CaMKⅡα*$^+$ and *Gad1*$^+$ cells. *Mitochondrially encoded NADH: ubiquinone oxidoreductase core subunit*

3 (MT-ND3) was notably up-regulated in various cell types. *Ribosomal protein L41 pseudogene (Gm10076)* and *Cystatin C (Cst3)* were significantly down-regulated in at least seven cell types (Figure 4.2B). Further analysis of *DEGs* in all cells revealed that approximately 20% of down-regulated *DEGs* (Figure 4.2C) and 21% of up-regulated *DEGs* (Figure 4.2D) were detected in at least two cell types.

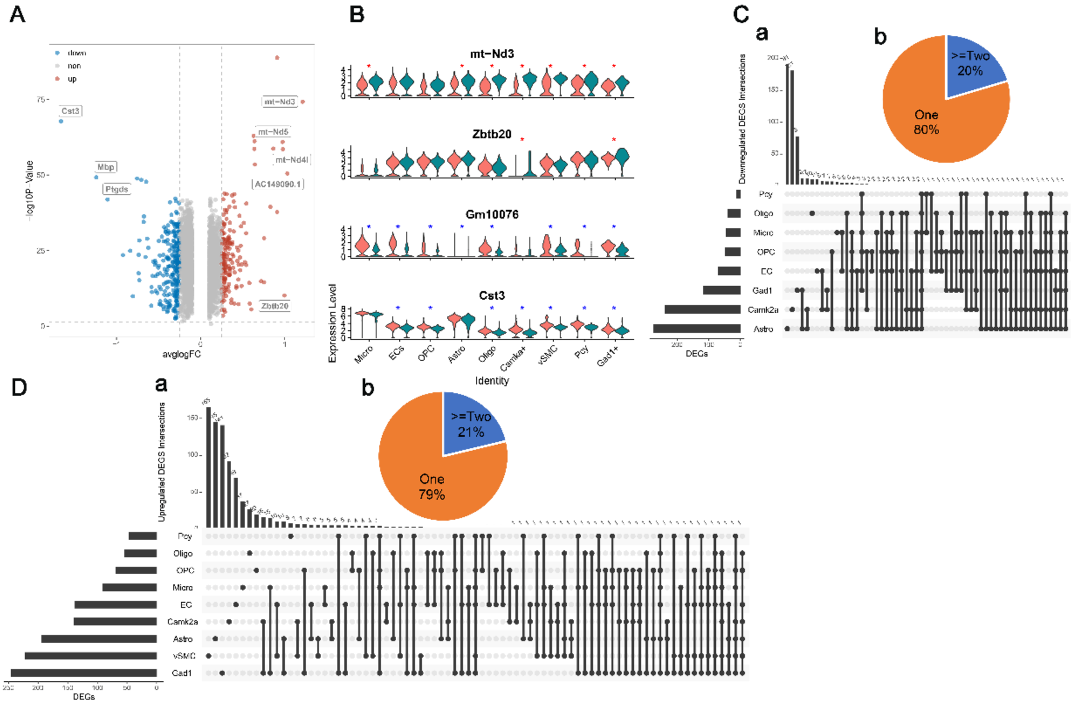

Figure 4.2 tFUS-induced *DEG*s are detected by scRNA-seq in RSC.

(A) Volcano plot of *DEGs*. The X-axis represents |$\log_2$ (fold change)|, Y-axis represents -$\log_{10}$ (*P*_adj), each point represents a gene, red dots represent the genes with a significant increase, blue dots represent the genes with a significant decrease, and grey dots represent the genes without significant changes.

(B) Violin plot displays *DEGs* expressed in different cell types.

(C) a, Upset plot exhibits markedly down-regulated *DEGs* induced by tFUS in different cell types.

b, Sector diagram shows that nearly 20% of down-regulated *DEGs* are present in at least two cell types.

(D) a, Upset plot displays significantly upregulated *DEGs* induced by tFUS in different cell types.

b, Sector diagram shows that nearly 21% of upregulated *DEGs* are present in at least two cell types.

4.3 Cell type-dependent functional changes induced by tFUS

To further explore the functional changes in tFUS-induced *DEGs*, we used gene set enrichment analysis (GSEA) (Subramanian et al., 2005) to analyze the degree of differential expression of genes in Ctrl and tFUS groups. A normalized enrichment score (NES) was used to detect whether the preset gene set was enriched at the top or the end of the gene sequence list to determine the effect of synergistic changes of *DEG* (Figures 4.3A and B).

Firstly, enrichment analysis was conducted for the related biological process (BP) involved in *DEG* to explore the main BP performed by gene products under tFUS. Figure 4.3C shows each cell type's first five BP subitems altered (activated or inhibited). The corresponding changes in BP of different cell types were also different. In Astro, activated BP mainly included lipid phosphorylation, mRNA metabolism, cell-cell communication, and protein autophosphorylation, while inhibited BP included oxidative phosphorylation, ATP metabolism, and mitochondrial function, such as electron transport chain. In *CaMKⅡ*α^{+} cells, BP activation was up-regulated by neural regulation, Ca^{2+} transport, lyase activity, and neurotransmitter receptor activity. Instead, suppressed Gene Ontology (GO) entries included neuronal myelin encapsulation and transition metal ion homeostasis. In our scRNA database, tFUS also altered gene expression in EC. We detected that activated BP was mainly related to vascular processing and negative regulation of cell communication. Nevertheless, the inhibited BP included oxidative phosphorylation and ATP metabolism. Activated BP entries were also detected in *Gad1*$^+$ cells, Micro, Oligo, and vSMC, but not in OPC and Pcy. At the same time, suppressed BP entries were detected in all cell types. Oxidative phosphorylation and ATP metabolism were inhibited in Astro, EC, Oligo, OPC, Micro, Pcy, and *Gad1*$^+$ cells. Activated GO entry was inhibited in *CaMKⅡα*$^+$ cells, OPC, and vSMC, but the entry was activated in *Gad1*$^+$ cells. These results suggested that the effect of tFUS on BP was cell-dependent, with only a few items consistent in all cell types.

Subsequently, GSEA was performed on DEGs' molecular function (MF) (Figures 4.3B and D) to explore the primary MF performed by gene product molecules under tFUS. Consistent with the results of BP analysis, only two activated MF entries were detected in Pcy, and no activated entries were detected in OPC. Among the top 5 MF entries for activation/suppression of each cell type, MF varied across cell types. For example, up-regulated guanine nucleotide exchange factor activity was detected in Astro, *CaMKⅡα*$^+$ cells, EC, and Oligo;

structural components of ribosomes were inhibited in Astro, EC, and Oligo but activated in *Gad1*$^+$ cells and Micro, suggesting that tFUS may influence ribosome function. In addition, proton transmembrane transporter activity (Astro, Oligo, and OPC), inorganic cation transmembrane transporter activity (EC, Micro, and Pyc), electron transfer activity (Astro, Micro, and Oligo), and amide binding activity (EC, OPC and vSMC) were inhibited in all three cell types, respectively. Ten MF entries were inhibited in two kinds of cells. For example, GTPase regulatory activity was inhibited in both Astro and EC.

Similarly, the enrichment analysis was also performed on the cellular component (CC) of *DEGs* (Figure 4.3E) to explore the role of *DEG* products under tFUS. Analysis showed that the proteins encoded by *DEGs* under tFUS were mainly located in lysosomes, mitochondria, myelin sheath, synapses, and cytoskeleton (Figures 4.3F and G).

Combined with the above results, tFUS could cause functional changes in transcription levels of different cell types.

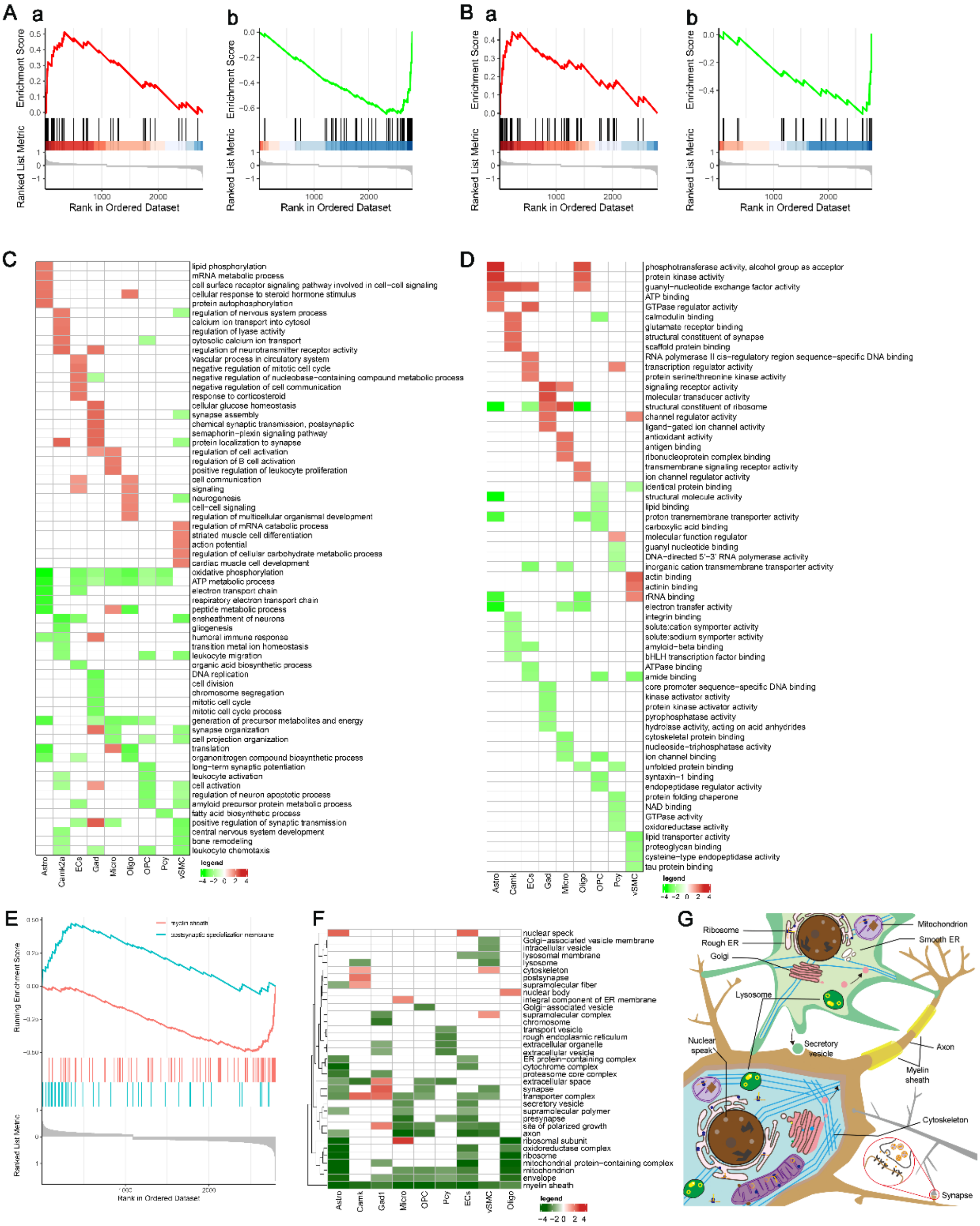

Figure 4.3 tFUS induces cell-dependent functional changes.

(A) *DEGs* are isolated from *CaMKⅡα*$^+$ cells by gene set enrichment analysis (GSEA).

Biological process (BP) activated (a) and suppressed (b) Gene Ontology (GO) entries representative graphs.

(B) *DEGs* are isolated from *CaMKⅡα*$^+$ cells by GSEA. Molecular function (MF) activated (a) and suppressed (b) GO entries representative graphs.

(C) The heat map shows the top five GO BP entries of normalized enrichment score (NES) after GSEA analysis. The colours in the figure represent NES, with red representing activated BP entries and green representing suppressed BP entries.

(D) The heat map exhibits the top five GO MF entries of NES after GSEA analysis. The colours in the figure represent NES, with red representing activated MF entries and green representing suppressed MF entries.

(E) GSEA results of *DEGs* in *CaMKⅡα*$^+$ cells display activation (blue) and inhibition (red) of GO entries by cellular component (CC).

(F) The heat map shows the results of GO CC entries after GSEA analysis, with red representing activated CC entries and green representing suppressed CC entries.

(G) The cell schematic diagram exhibits the possible subcellular localization of *DEG*-encoded proteins.

4.4 tFUS-activated cell types and populations identified by Egr1$^+$ cells

Based on chapter 3, tFUS increased the ratio of Egr1$^+$ cells in the RSC, which was then validated in the scRNA-seq results.

4.4.1 Single-cell expression profile of tFUS-activated RSC Egr1$^+$

The proportion of Egr1$^+$ cells was first detected based on scRNA-seq results in RSC after tFUS and was markedly higher in the tFUS (17.49%) than in the Ctrl (15.36%) (χ^2 test, P = 0.003). Egr1 was expressed in almost all cell types (Figure 4.4.1A), mainly in Micro, Oligo, EC, Neu, and vSMC (Figure 4.4.1B).

Moreover, tFUS increased the rate of Egr1$^+$ in different cell types, including Neu (Ctrl: 36.02%, tFUS: 59.89%, χ^2 test, $P < 0.001$), vSMC (Ctrl: 30.67%, tFUS: 50.87%, χ^2 test, $P < 0.001$), EC (Ctrl: 9.20%, tFUS: 16.78%, χ^2 test, $P < 0.001$), and Peri (Ctrl: 7.92%, tFUS: 17.60%, χ^2 test, $P < 0.05$), but there was no such change in other cell types (Figure 4.4.1C). At the cell population level, tFUS increased the ratio of Egr1$^+$ in two Neu subtypes, four EC subtypes, vSMC and Peri (Figure 4.4.1D). The ratio of Egr1$^+$ was reduced in a subtype of microglia (MC1) and neurons (Neu4).

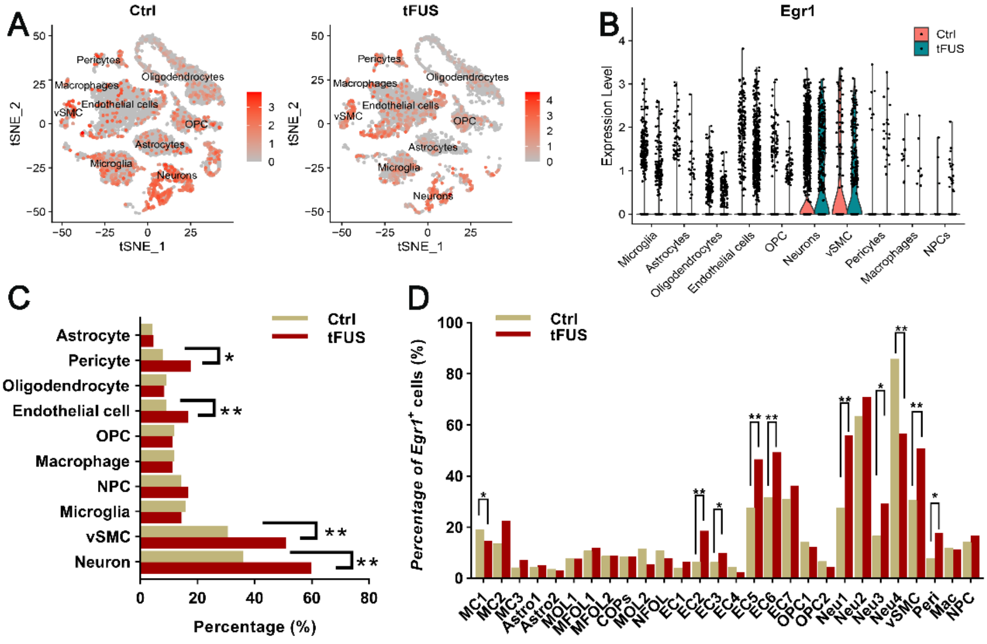

Figure 4.4.1 Egr1$^+$ single-cell atlas activated by tFUS in RSC.

(A) The *t*-SNE cell classification of Egr1$^+$ cells is visualized in the Ctrl group (left) and tFUS group (right).

(B) The violin diagram shows the expression level of Egr1$^+$ cells in different cell types.

(C) tFUS increases Egr1$^+$ cell ratios in Neu, vSMC, EC, and Peri ($^*P < 0.05$, $^{**}P < 0.01$).

(D) tFUS changes the proportion of Egr1$^+$ cells in different cell types ($^*P < 0.05$, $^{**}P <$

0.01).

4.4.2 Different *IEGs* responded differently to tFUS

To verify whether other *IEGs* responded to tFUS, the co-expression of *Egr1* with other *IEGs*, such as *Fosl2* and *Junb*, was analyzed based on the scRNA-seq results of RSC (Figure 4.4.2A). Among the cells expressing *Fosl2* and *Egr1*, only 13.24% of cells were double-positive (*Fosl2*$^+$/*Egr1*$^+$), and 19.36% of cells only expressed *Fosl2* (*Fosl2*$^+$/*Egr1*$^-$), and the rest of cells were *Egr1* positive cells (*Fosl2*$^-$/*Egr1*$^+$). This co-expression existed in *Egr1*, *Junb,* and other *IEGs*, including *Fosb*, *Arc*, *Egr3*, *Jun*, and *Nr4a1* (Figure 4.4.2B), suggesting that different *IEGs* had different expression patterns in the CNS.

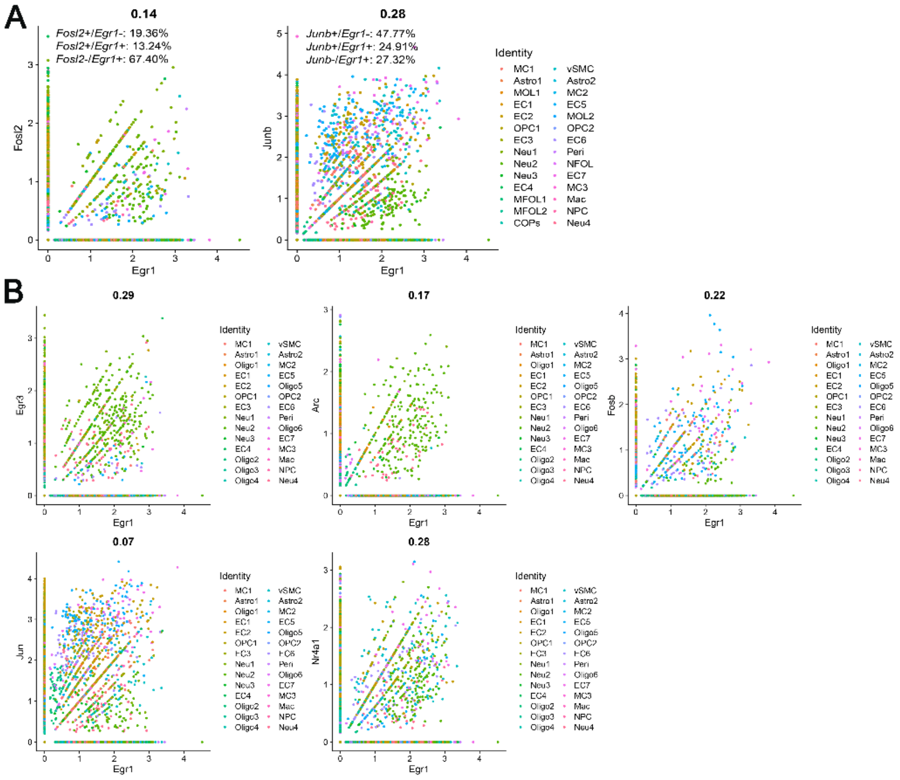

Figure 4.4.2 tFUS can cause expression changes of other *immediate-early genes*

(IEGs).

(A) The scatter plots show the co-expression of *Fosl2* with *Egr1* (left) and *Junb* with *Egr1* (right).

(B) The scatter diagrams display the co-expression of *Egr1* with other *IEGs*.

4.4.3 tFUS induced various types of *IEGs* to change in different types of cells

In addition to *Egr1*, did tFUS also cause other *IEG* expression changes? Comparing the proportion of different *IEG* positive cells in the Ctrl and tFUS groups based on scRNA-seq results from the RSC, tFUS increased the proportion of positive cells in five types of *IEGs*, including *Jun, Fosb, Fosl2, Junb,* and *Nr4a1*, but did not affect *Arc*. However, the percentage of *Egr3*$^+$ cells decreased.

Most of the detected *IEG* expressions were similar under tFUS. For example, tFUS increased the percentage of Egr1$^+$ cells in EC1, EC2, EC3, and vSMC, with the same phenomenon in *Jun, Fosb, Fosl2,* and *Junb* (Figure 4.4.3A). In Neu1 and Neu3, tFUS caused changes in the expression of at least three *IEGs*. Therefore, cells with at least three *IEG* changes were defined as tFUS responsive cells.

Based on this criterion, four neuron subtypes, six EC subtypes, MC1, vSMC, MFOL1, and NFOL (Figure 4.4.3B), were tFUS responsive cell populations. Among neuron populations, tFUS increased the ratio of six *IEGs* in glutamate neuron subtypes, Neu1 and Neu2, and three *IEGs* in gamma-aminobutyric neuron subtypes, Neu3. At the same time, it also reduced the ratio of three kinds of *IEGs* in glutamate neuron subtype Neu4. In MC1, the proportion of *Egr1*$^+$ cells decreased, but the expression of *Fosb, Junb, and Nr4a1* increased. EC, vSMC, and Peri are all essential components of blood vessels in the nervous system. Therefore, tFUS acted on RSC from the above results, affecting neurons, blood vessels, microglia, and oligodendrocytes.

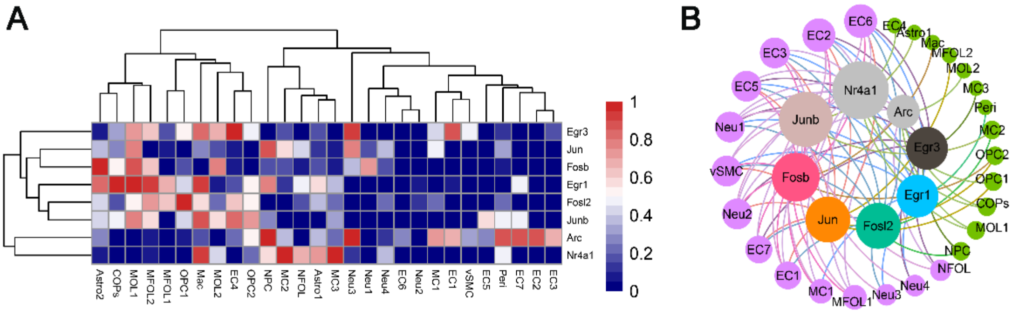

Figure 4.4.3 tFUS induces the changes of various *IEGs* in different cell types.

(A) The heat map presents the *P*-value (χ^2 test) of the change in *IEG*$^+$ cell ratio under tFUS.

(B) The network diagram exhibits the association between different populations of *IEG*$^+$ cells with varying ratios under tFUS.

4.5 Potential communication pathways between tFUS-sensitive cells and other cells

Since *Egr1* was highly expressed in Neu (*CaMKⅡα*$^+$*, GAD*$^+$ cells), EC, and vSMC after tFUS, the cells activated by tFUS were key nodes of intercellular communication, receiving or transmitting information to other cell types, resulting in changes in the transcriptome. Therefore, I mainly focused on the cellular communication between tFUS-sensitive cells and other cells. The common cellular communication pathways in the Ctrl group were excluded.

CaMKⅡα$^+$ cells first release glutamate, which binds to the AMPA receptor (α-amino-3-hydroxy-5-methyl-4-isoxazole-propionic acid receptor, AMPAR), NMDA receptor (N-methyl-D-aspartic acid receptor, NMDAR), kainate receptor and metabolic glutamate receptor further induce changes in gene expression (Meldrum et al., 1999). In our obtained scRNA-seq results (Figure 4.5A), we detected that the genes encoding the AMPAR subunit were mainly in OPC and Astro; genes encoding metabolic glutamate receptors, such as *glutamate metabotropic receptor 3 (Grm3)*, were mainly found in Astro and Oligo; the *metabolic amate metabotropic receptor 5 (Grm5)* was mainly found in Astro, and the *metabolic amate metabotropic receptor 7 (Grm7)* was mainly in pericyte (Pcy). These results indicated that Astro, Oligo, and Pcy might receive glutamatergic signals from *CaMKⅡα*$^+$ cells.

In addition, potential cell-to-cell communication pathways were analyzed using the CellChat R package (Figures 4.5B and C). We found that *CaMKⅡα*$^+$ cells expressed chemokine receptor through Cx3cl1-Cx3cr1 (C-X3-C motif chemokine ligand 1-C-X3-C motif chemokine receptor 1) and Thy1- Itgam_Itgb2 (Thymus cell antigen 1 theta - Integrin alpha-M_Integrin beta 2) pathways communicated with Micro (Figure 4.5D). Moreover, *CaMKⅡα*$^+$ cells communicated with Astro, OPC, Oligo, *GAD1*$^+$ cells, and EC through EPHA, NT, and NRG pathways (Figure 4.5E). The cell subtypes EC1-3 had a similar signaling output and communicated with Oligo, Pcy, Astro, OPC, and Micro via PROS, CD39, and GALECTIN pathways (Figure 4.5F). The expression of Egr1 in vSMC was also significantly increased. We detected that vSMC communicated with other cell types mainly through ncWNT, FGF, and ANGPT pathways (Figure 4.5G). Thus, different intercellular communication enabled EC, *CaMKⅡα*$^+$ cells, or vSMC to act on other cell types, resulting in transcriptome changes (Figure 4.5H).

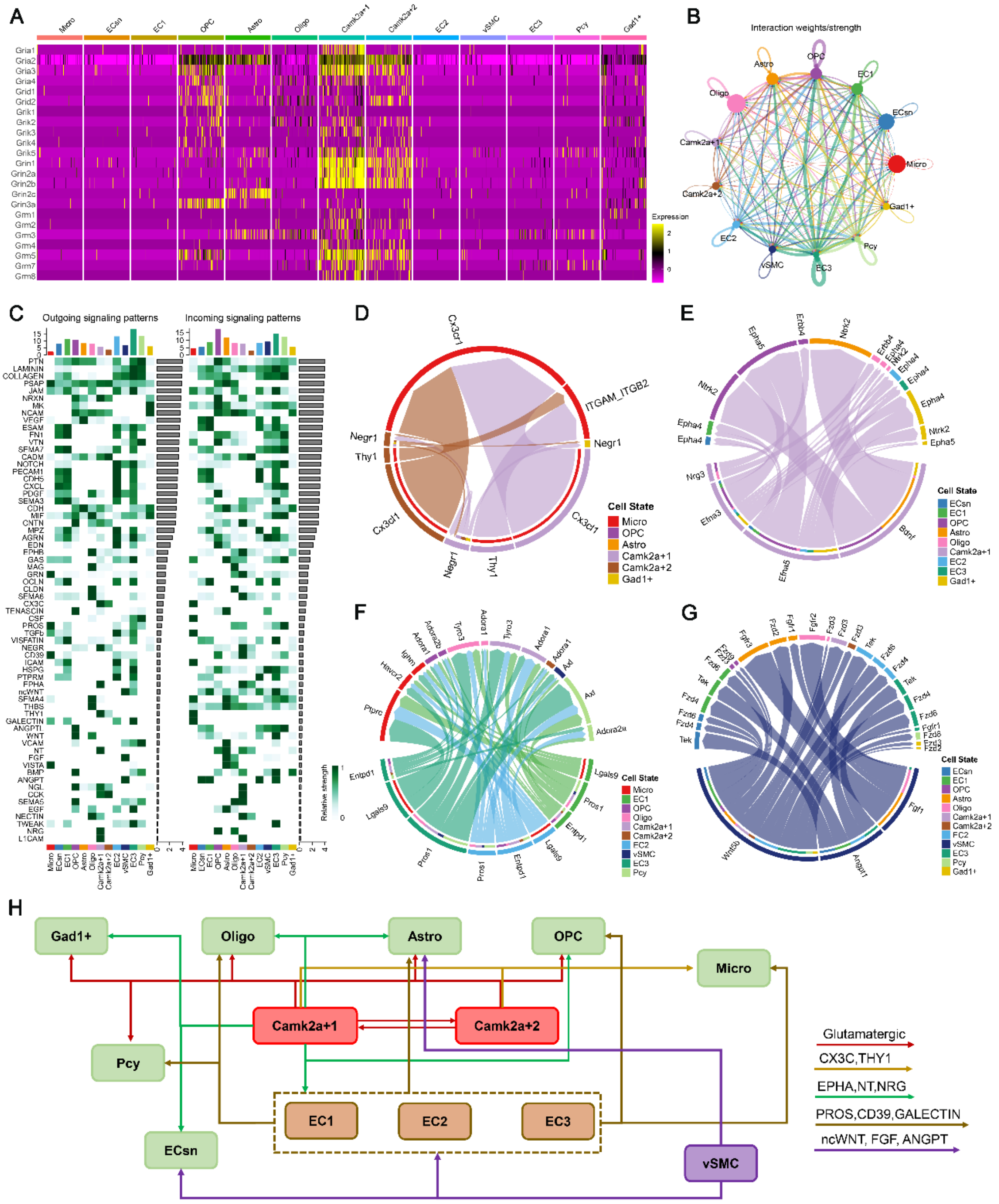

Figure 4.5 Potential communication pathways between tFUS-sensitive cells and other cells.

(A) The heat map exhibits the expression of ionic glutamate receptor subunits in different cell types, including AMPAR (α-amino-3-hydroxy-5-methyl-4-isoxazole-propionic acid receptor), NMDAR (N-methyl-D-aspartic acid receptor), kainate receptor and metabolic receptor.

(B) The network diagram shows the relative intensity of cell-to-cell communication between different cell types based on CellChat analysis.

(C) The heat maps display signal output and input patterns between different cell types in RSC. The colour represents the relative intensity of communication between cells.

(D) The chord diagram exhibits that *CaMKⅡα*$^{+}$*1* and *CaMKⅡα*$^{+}$*2* cells communicate with Micro by Cx3cl1 (C-x3-C motif chemokine ligand 1) and Thy1 (Thymus cell antigen 1 theta).

(E) The chord diagram shows that *CaMKⅡα*$^{+}$*1* cells are mediated by Nrg (Neuregulin), Efna5 (Ephrin A5), Efna3 (Ephrin A3) and Bdnf (brain-derived neurotrophic factor) to communicate with other cell types.

(F) EC1, EC2, and EC3 have similar signal output patterns and communicate with other cell types via PROS, CD39, and GALECTIN pathways.

(G) vSMC transmits signals through ncWNT, FGF, and ANGPT pathways.

(H) The schematic diagram presents the cell-cell communication pattern between tFUS-sensitive and tFUS-insensitive cells.

4.6 Discussion

To further explore the characteristics of tFUS responsive cells, we used scRNA-seq to map the single-cell transcriptome expression of RSC. scRNA-seq results showed that tFUS induced cell-specific transcriptome changes and cell type-dependent functional changes. Based on the nature of tFUS, our findings broaden the field for non-invasive and non-pharmacological approaches to mapping and regulating brain function. These advances may also provide a new, safe approach to clinically targeting brain activity.

4.6.1 Single-cell transcriptome atlas of tFUS-sensitive cells

The previous transcriptome changes related to tFUS were detected by second-generation RNA-seq to explore the molecular changes in the ultrasonic treatment of skin wounds and fracture healing (de Lucas et al., 2021; Shimizu et al., 2021). In addition to these studies, there have been no other RNA-seq studies of tFUS. We first mapped the single-cell transcriptome atlas of tFUS-sensitive cells. In our scRNA-seq results, nine main cell types were identified by scRNA-seq in RSC after tFUS, namely glutamate neurons, GABA interneurons, microglia, astrocytes, oligodendrocytes, oligodendrocyte precursor cells, endothelial cells, pericytes, and vascular smooth muscle cells. Our results showed that tFUS induced extensive transcriptional changes in the RSC, and *DEGs* were detected in all cell types. Approximately 23% of *DEGs* were expressed in at least two cell types, and these *DEGs* may affect lysosomal, mitochondrial, myelin, synaptic, and cytoskeletal functions.

Significantly up-regulated *Egr1* expression was also detected in the sequencing results, consistent with the expression results of Egr1 detected by qPCR and immunofluorescent staining. After tFUS, marked changes in *Egr1*$^{+}$ cell ratios were detected in 10 cell subpopulations. The proportion of *Egr1*$^{+}$ cells increased in 8 cell populations and decreased in 2 cell populations. Under ultrasonic stimulation, the percentage of *Egr1*$^{+}$ cells in glutamate neurons changed dramatically: in the Neu1 subtype, tFUS may play an excitatory role, increasing the percentage of *Egr1*$^+$ cells. At the same time, it was also found that the percentage of *Egr1*$^+$ cells in the Neu3 subtype expressing *GAD1* was increased, suggesting that tFUS activates GABAergic neurons and down-regulates the excitability of neural circuits. The results of multi-channel in vivo recording also found that tFUS had a higher rate of change in the firing activity of GABAergic interneurons than glutamate neurons, which suggests that tFUS co-regulates inhibitory and excitatory neurons, and there is a balance between inhibitory and excitatory neurons to determine the final effect. In our study, the integrated effect of tFUS inhibits the neuronal activity of RSC, thereby increasing PWT and prolonging TWL in mice. This result was consistent with reports that inhibition of excitatory neurons in the RSC can relieve pain (J.-H. Wang et al., 2021); we also provided a novel approach to regulate gene expression in tFUS-targeted brain regions. Our results also demonstrate unequivocally that gene expression changes in tFUS-sensitive cells are associated with a significantly elevated somatosensory threshold at the single-cell level.

In addition to *Egr1*, tFUS also caused other *IEG* expression changes, including *Jun*, *Junb*, *Fosb*, *Fosl2*, and *Nr4a1*. They might cooperate with *Egr1* or be independent of sensing the tFUS stimulation and modulating the transcriptome changes. In order to further address the potential role of the other *IEG*, we will first detect the expression of those candidate IEGs in transcriptomic and protein levels by qPCR and immunostaining after tFUS stimulation. Then, we will explore the relationship between those candidates and *Egr1*.

In addition, we find multiple cellular communication pathways between tFUS-sensitive cells and other cell types, highlighting the potential for tFUS-sensitive cells to communicate with other cell types to induce transcriptional changes. Among those potential cellular communication pathways, we are intrigued by Cx3cl1-Cx3cr1 because it plays a crucial role in pain regulation by mediating neuro-immune communication between neurons and microglia (Clark & Malcangio, 2014). Based on our scRNA-seq results, *CaMKⅡα*$^+$ neurons expressed chemokine receptors through the Cx3cl1-Cx3cr1 pathway communicated with microglia. In order to approach this experimentally, first, we will detect the correlation between Cx3cl1-Cx3cr1 with *CaMKⅡα*$^+$ neurons by RCP array to confirm whether this pathway tFUS modulation in *CaMKⅡα*$^+$ neurons; second, using qPCR and western blot confirms the changes in the pivotal factors of this pathway; then, we will try to clarify the causal relationship between the pivotal factors in the pathway and the *CaMKⅡα*$^+$ neurons modulated by tFUS, for example, knocking down the pivotal factors in *CaMKⅡα*$^+$ neurons to detect the tFUS-induced behavioral paradigms.

Our results also prove that tFUS is a feasible approach to regulating neuronal activity and hint that tFUS has the potential to treat epilepsy, chronic pain, and other brain diseases.

4.6.2 Limitations and future works

Several limitations exist in this study. First, we only detected cells in the RSC by scRNA-seq. Whether tFUS has the same effect on other brain regions needs further verification. Second, in our scRNA-seq system, neurons accounted for only about 10% of the total number of RSC cells, which led to the number of Trpc4 cells being few, and the analysis error toward Trpc4 would be immense. Then, we plan to optimize the cell sorting method, increase the proportion of neurons, and further analyze Trpc4 in different cell types.

Chapter 5 Summary

Our study discovered that stimulation of RSC by tFUS caused remarkable changes in neuronal activity and behaviourally altered pain threshold in mice, accompanied by changes in transcriptional and protein levels of Egr1. These Egr1$^+$ cells played an essential role in the analgesic effect of tFUS. Based on Egr1-GFP cells RNA-seq, we identified Trpc4, mainly expressed in neurons. Trpc4 also controlled the response of Egr1$^+$ cells to tFUS. Trpc4, as a critical factor in the neuronal regulation of tFUS, will provide a new strategy for the noninvasive treatment of chronic pain. To further explore the characteristics of tFUS-responsive cells, we used scRNA-seq to map the single-cell transcriptome expression of RSC. ScRNA-seq results showed that tFUS induced cell-specific transcriptome changes and cell type-dependent functional changes.

In summary, we have achieved spatially and temporally precise, non-invasive in vivo ultrasonic stimulation in the brain of the free-moving mouse. Different from traditional neuromodulation techniques, tFUS could penetrate the skull to focus energy on specific brain regions without injection of an exogenous genetic virus. The method of tFUS acting on RSC described here is likely to fulfill the long-sought goal of effective treatment of chronic pain, with potential applications ranging from neuroscience research to clinical therapeutics. In addition, tFUS can be used in different brain regions to achieve non-invasively neuromodulation and treatment of diseases. We envisage this technique could also be applied to deeper brain regions in rodents, non-human primates, and humans, which will promote the development and advancement of neuroscience.

Reference

Abdus-Saboor, I., & Luo, W. (2022). Measuring Mouse Somatosensory Reflexive Behaviors with High-speed Videography, Statistical Modeling, and Machine Learning. *Neuromethods*, *178*, 441–456. https://doi.org/10.1007/978-1-0716-2039-7_21

Abrahao, A., Meng, Y., Llinas, M., Huang, Y., Hamani, C., Mainprize, T., Aubert, I., Heyn, C., Black, S. E., Hynynen, K., Lipsman, N., & Zinman, L. (2019). First-in-human trial of blood-brain barrier opening in amyotrophic lateral sclerosis using MR-guided focused ultrasound. *Nature Communications*, *10*(1), 4373. https://doi.org/10.1038/s41467-019-12426-9

Airan, R. D., Meyer, R. A., Ellens, N. P. K., Rhodes, K. R., Farahani, K., Pomper, M. G., Kadam, S. D., & Green, J. J. (2017). Noninvasive Targeted Transcranial Neuromodulation via Focused Ultrasound Gated Drug Release from Nanoemulsions. *Nano Letters*, *17*(2), 652–659. https://doi.org/10.1021/acs.nanolett.6b03517

Apkarian, A. V., Bushnell, M. C., Treede, R.-D., & Zubieta, J.-K. (2005). Human brain mechanisms of pain perception and regulation in health and disease. *European Journal of Pain (London, England)*, *9*(4), 463–484. https://doi.org/10.1016/j.ejpain.2004.11.001

Bachtold, M. R., Rinaldi, P. C., Jones, J. P., Reines, F., & Price, L. R. (1998). Focused Ultrasound Modifications of Neural Circuit Activity in a Mammalian Brain. *Ultrasound in Medicine & Biology*, *24*(4), 557–565. https://doi.org/https://doi.org/10.1016/S0301-5629(98)00014-3

Badran, B. W., Caulfield, K. A., Stomberg-Firestein, S., Summers, P. M., Dowdle, L. T., Savoca, M., Li, X., Austelle, C. W., Short, E. B., Borckardt, J. J., Spivak, N., Bystritsky, A., & George, M. S. (2020). Sonication of the anterior thalamus with MRI-Guided transcranial focused ultrasound (tFUS) alters pain thresholds in healthy adults: A double-blind, sham-controlled study. *Brain Stimulation*, *13*(6), 1805–1812. https://doi.org/10.1016/j.brs.2020.10.007

Baek, H., Pahk, K. J., & Kim, H. (2017). A review of low-intensity focused ultrasound for neuromodulation. *Biomedical Engineering Letters*, *7*(2), 135–142. https://doi.org/10.1007/s13534-016-0007-y

Ballantine, H. T., Bell, E., & Manlapaz, J. (n.d.). Progress and Problems in the Neurological Applications of Focused Ultrasound. *Journal of Neurosurgery*, *17*(5), 858–876. https://doi.org/10.3171/jns.1960.17.5.0858

Basbaum, A. I., Bautista, D. M., Scherrer, G., & Julius, D. (2009). Cellular and

Molecular Mechanisms of Pain. *Cell*, *139*(2), 267–284. https://doi.org/https://doi.org/10.1016/j.cell.2009.09.028

Beech, D. J. (2012). Integration of transient receptor potential canonical channels with lipids. *Acta Physiologica (Oxford, England)*, *204*(2), 227–237. https://doi.org/10.1111/j.1748-1716.2011.02311.x

Blackmore, J., Shrivastava, S., Sallet, J., Butler, C. R., & Cleveland, R. O. (2019). Ultrasound Neuromodulation: A Review of Results, Mechanisms and Safety. *Ultrasound in Medicine & Biology*, *45*(7), 1509–1536. https://doi.org/https://doi.org/10.1016/j.ultrasmedbio.2018.12.015

Blicher, A., Wodzinska, K., Fidorra, M., Winterhalter, M., & Heimburg, T. (2009). The temperature dependence of lipid membrane permeability, its quantized nature, and the influence of anesthetics. *Biophysical Journal*, *96*(11), 4581–4591. https://doi.org/10.1016/j.bpj.2009.01.062

Brewer, G. J., & Torricelli, J. R. (2007). Isolation and culture of adult neurons and neurospheres. *Nature Protocols*, *2*(6), 1490–1498. https://doi.org/10.1038/nprot.2007.207

Brohawn, S. G. (2015). How ion channels sense mechanical force: insights from mechanosensitive K2P channels TRAAK, TREK1, and TREK2. *Annals of the New York Academy of Sciences*, *1352*(1), 20–32. https://doi.org/https://doi.org/10.1111/nyas.12874

Castillo Saavedra, L., Mendonca, M., & Fregni, F. (2014). Role of the primary motor cortex in the maintenance and treatment of pain in fibromyalgia. *Medical Hypotheses*, *83*(3), 332–336. https://doi.org/10.1016/j.mehy.2014.06.007

Chaplan, S. R., Bach, F. W., Pogrel, J. W., Chung, J. M., & Yaksh, T. L. (1994). Quantitative assessment of tactile allodynia in the rat paw. *Journal of Neuroscience Methods*, *53*(1), 55–63. https://doi.org/10.1016/0165-0270(94)90144-9

Chernov, M., & Roe, A. W. (2014). Infrared neural stimulation: a new stimulation tool for central nervous system applications. *Neurophotonics*, *1*(1), 11011. https://doi.org/10.1117/1.NPh.1.1.011011

Choi, J., Lim, S., Cho, K., Kim, D., Jang, D. P., & Kim, I. (2013). The effect of focused ultrasonic stimulation on the activity of hippocampal neurons in multi-channel electrode. In *International IEEE/EMBS Conference on Neural Engineering*. https://doi.org/10.1109/NER.2013.6696038

Choleris, E., Thomas, A. W., Kavaliers, M., & Prato, F. S. (2001). A detailed ethological analysis of the mouse open field test: effects of diazepam, chlordiazepoxide and an extremely low frequency pulsed magnetic field. *Neuroscience & Biobehavioral Reviews*, *25*(3), 235–260. https://doi.org/https://doi.org/10.1016/S0149-7634(01)00011-2

Christensen, A. P., & Corey, D. P. (2007). TRP channels in mechanosensation:

direct or indirect activation? *Nature Reviews Neuroscience*, *8*(7), 510–521. https://doi.org/10.1038/nrn2149

Chu, P.-C., Liu, H.-L., Lai, H.-Y., Lin, C.-Y., Tsai, H.-C., & Pei, Y.-C. (2015). Neuromodulation accompanying focused ultrasound-induced blood-brain barrier opening. In *Scientific reports* (Vol. 5, p. 15477). https://doi.org/10.1038/srep15477

Clark, A. K., & Malcangio, M. (2014). Fractalkine/CX3CR1 signaling during neuropathic pain . In *Frontiers in Cellular Neuroscience* (Vol. 8). https://www.frontiersin.org/articles/10.3389/fncel.2014.00121

Colvin, L., & Colvin, L. (2012). ABC of Pain. *Wiley John + Sons*.

Da Silva, J. T., & Seminowicz, D. A. (2019). Neuroimaging of pain in animal models: a review of recent literature. *Pain Reports*, *4*(4), e732. https://doi.org/10.1097/PR9.0000000000000732

Dahlhamer, J., Lucas, J., Zelaya, C., Nahin, R., Mackey, S., DeBar, L., Kerns, R., Von Korff, M., Porter, L., & Helmick, C. (2018). Prevalence of Chronic Pain and High-Impact Chronic Pain Among Adults - United States, 2016. *MMWR. Morbidity and Mortality Weekly Report*, *67*(36), 1001–1006. https://doi.org/10.15585/mmwr.mm6736a2

de Lucas, B., Pérez, L. M., Bernal, A., & Gálvez, B. G. (2021). Application of low-intensity pulsed therapeutic ultrasound on mesenchymal precursors does not affect their cell properties. *PloS One*, *16*(2), e0246261. https://doi.org/10.1371/journal.pone.0246261

de Melo Reis, R. A., Freitas, H. R., & de Mello, F. G. (2020). Cell Calcium Imaging as a Reliable Method to Study Neuron–Glial Circuits . In *Frontiers in Neuroscience* (Vol. 14). https://www.frontiersin.org/article/10.3389/fnins.2020.569361

Deffieux, T., Younan, Y., Wattiez, N., Tanter, M., Pouget, P., & Aubry, J.-F. (2013). Low-Intensity Focused Ultrasound Modulates Monkey Visuomotor Behavior. *Current Biology*, *23*(23), 2430–2433. https://doi.org/https://doi.org/10.1016/j.cub.2013.10.029

Deuis, J. R., Dvorakova, L. S., & Vetter, I. (2017). Methods Used to Evaluate Pain Behaviors in Rodents. *Frontiers in Molecular Neuroscience*, *10*, 284. https://doi.org/10.3389/fnmol.2017.00284

Dickey, T. C., Tych, R., Kliot, M., Loeser, J. D., Pederson, K., & Mourad, P. D. (2012). Intense focused ultrasound can reliably induce sensations in human test subjects in a manner correlated with the density of their mechanoreceptors. *Ultrasound in Medicine & Biology*, *38*(1), 85–90. https://doi.org/10.1016/j.ultrasmedbio.2011.09.020

Downs, M. E., Lee, S. A., Yang, G., Kim, S., Wang, Q., & Konofagou, E. E. (2018). Non-invasive peripheral nerve stimulation via focused ultrasoundin vivo. *Physics in Medicine & Biology*, *63*(3), 35011.

https://doi.org/10.1088/1361-6560/aa9fc2

Duque, M., Lee-Kubli, C. A., Tufail, Y., Magaram, U., Patel, J., Chakraborty, A., Mendoza Lopez, J., Edsinger, E., Vasan, A., Shiao, R., Weiss, C., Friend, J., & Chalasani, S. H. (2022). Sonogenetic control of mammalian cells using exogenous Transient Receptor Potential A1 channels. *Nature Communications*, *13*(1), 600. https://doi.org/10.1038/s41467-022-28205-y

El Hady, A., & Machta, B. (2014). Mechanical Surface Waves Accompany Action Potential Propagation. *ArXiv*.

Fichtl, B., Shrivastava, S., & Schneider, M. F. (2016). Protons at the speed of sound: Predicting specific biological signaling from physics. *Scientific Reports*, *6*(1), 22874. https://doi.org/10.1038/srep22874

Fini, M., & Tyler, W. J. (2017). Transcranial focused ultrasound: a new tool for non-invasive neuromodulation. *International Review of Psychiatry*, *29*(2), 168–177. https://doi.org/10.1080/09540261.2017.1302924

Finnerup, N. B., Attal, N., Haroutounian, S., McNicol, E., Baron, R., Dworkin, R. H., Gilron, I., Haanpää, M., Hansson, P., Jensen, T. S., Kamerman, P. R., Lund, K., Moore, A., Raja, S. N., Rice, A. S. C., Rowbotham, M., Sena, E., Siddall, P., Smith, B. H., & Wallace, M. (2015). Pharmacotherapy for neuropathic pain in adults: a systematic review and meta-analysis. *The Lancet. Neurology*, *14*(2), 162–173. https://doi.org/10.1016/S1474-4422(14)70251-0

Fisher, J. A. N., & Gumenchuk, I. (2018). Low-intensity focused ultrasound alters the latency and spatial patterns of sensory-evoked cortical responsesin vivo. *Journal of Neural Engineering*, *15*(3), 35004. https://doi.org/10.1088/1741-2552/aaaee1

Foley, J. L., Little, J. W., & Vaezy, S. (2008). Effects of high-intensity focused ultrasound on nerve conduction. *Muscle & Nerve*, *37*(2), 241–250. https://doi.org/https://doi.org/10.1002/mus.20932

Fouragnan, E. F., Chau, B. K. H., Folloni, D., Kolling, N., Verhagen, L., Klein-Flügge, M., Tankelevitch, L., Papageorgiou, G. K., Aubry, J.-F., Sallet, J., & Rushworth, M. F. S. (2019). The macaque anterior cingulate cortex translates counterfactual choice value into actual behavioral change. *Nature Neuroscience*, *22*(5), 797–808. https://doi.org/10.1038/s41593-019-0375-6

Frazee, A. C., Pertea, G., Jaffe, A. E., Langmead, B., Salzberg, S. L., & Leek, J. T. (2015). Ballgown bridges the gap between transcriptome assembly and expression analysis. In *Nature biotechnology* (Vol. 33, Issue 3, pp. 243–246). https://doi.org/10.1038/nbt.3172

FRY, F. J., ADES, H. W., & FRY, W. J. (1958). Production of Reversible Changes in the Central Nervous System by Ultrasound. *Science*, *127*(3289), 83 LP – 84. https://doi.org/10.1126/science.127.3289.83

FRY, W. J., FRY, F. J., BARNARD, J. W., KRUMINS, R. F., & BRENNAN, J. F. (1955). Ultrasonic Lesions in the Mammalian Central Nervous System. *Science*, *122*(3168), 517 LP – 518. https://doi.org/10.1126/science.122.3168.517

Fry, W. J., Wulff, V. J., Tucker, D., & Fry, F. J. (1950). Physical Factors Involved in Ultrasonically Induced Changes in Living Systems: I. Identification of Non‐Temperature Effects. *The Journal of the Acoustical Society of America*, *22*(6), 867–876. https://doi.org/10.1121/1.1906707

Gasca-Salas, C., Fernández-Rodríguez, B., Pineda-Pardo, J. A., Rodríguez-Rojas, R., Obeso, I., Hernández-Fernández, F., del Álamo, M., Mata, D., Guida, P., Ordás-Bandera, C., Montero-Roblas, J. I., Martínez-Fernández, R., Foffani, G., Rachmilevitch, I., & Obeso, J. A. (2021). Blood-brain barrier opening with focused ultrasound in Parkinson’s disease dementia. *Nature Communications*, *12*(1), 779. https://doi.org/10.1038/s41467-021-21022-9

Gavrilov, L. (2008). The possibility of generating focal regions of complex configurations in application to the problems of stimulation of human receptor structures by focused ultrasound. *Acoustical Physics*, *54*, 269–278. https://doi.org/10.1134/S1063771008020152

Gavrilov, L R, Tsirulnikov, E. M., & Davies, I. a. I. (1996). Application of focused ultrasound for the stimulation of neural structures. *Ultrasound in Medicine & Biology*, *22*(2), 179–192. https://doi.org/https://doi.org/10.1016/0301-5629(96)83782-3

Gavrilov, Leonid R, Gersuni, G. V, Ilyinsky, O. B., Tsirulnikov, E. M., & Shchekanov, E. E. (1977). A study of reception with the use of focused ultrasound. II. Effects on the animal receptor structures. *Brain Research*, *135*(2), 279–285. https://doi.org/https://doi.org/10.1016/0006-8993(77)91031-9

Guo, H., Hamilton II, M., Offutt, S. J., Gloeckner, C. D., Li, T., Kim, Y., Legon, W., Alford, J. K., & Lim, H. H. (2018). Ultrasound Produces Extensive Brain Activation via a Cochlear Pathway. *Neuron*, *98*(5), 1020-1030.e4. https://doi.org/10.1016/j.neuron.2018.04.036

Haar, G. ter. (2009). Ultrasound bioeffects and safety. *Proceedings of the Institution of Mechanical Engineers, Part H: Journal of Engineering in Medicine*, *224*(2), 363–373. https://doi.org/10.1243/09544119JEIM613

Hallett, M. (2000). Transcranial magnetic stimulation and the human brain. *Nature*, *406*(6792), 147–150. https://doi.org/10.1038/35018000

Hameroff, S., Trakas, M., Duffield, C., Annabi, E., Gerace, M. B., Boyle, P., Lucas, A., Amos, Q., Buadu, A., & Badal, J. J. (2013). Transcranial Ultrasound (TUS) Effects on Mental States: A Pilot Study. *Brain Stimulation*, *6*(3), 409–415.

https://doi.org/https://doi.org/10.1016/j.brs.2012.05.002

Han, F., Yu, H., Tian, C., Chen, H. E., Benedict-Alderfer, C., Zheng, Y., Wang, Q., Han, X., & Zheng, Q. Y. (2012). A new mouse mutant of the Cdh23 gene with early-onset hearing loss facilitates evaluation of otoprotection drugs. *The Pharmacogenomics Journal*, *12*(1), 30–44. https://doi.org/10.1038/tpj.2010.60

Han, S., Kim, M., Kim, H., Shin, H., & Youn, I. (2018). Ketamine Inhibits Ultrasound Stimulation-Induced Neuromodulation by Blocking Cortical Neuron Activity. *Ultrasound in Medicine & Biology*, *44*(3), 635–646. https://doi.org/https://doi.org/10.1016/j.ultrasmedbio.2017.11.008

Hargreaves, K., Dubner, R., Brown, F., Flores, C., & Joris, J. (1988). A new and sensitive method for measuring thermal nociception in cutaneous hyperalgesia. *Pain*, *32*(1), 77–88. https://doi.org/https://doi.org/10.1016/0304-3959(88)90026-7

Harvey, E. N. (1929). THE EFFECT OF HIGH FREQUENCY SOUND WAVES ON HEART MUSCLE AND OTHER IRRITABLE TISSUES. *American Journal of Physiology-Legacy Content*, *91*(1), 284–290. https://doi.org/10.1152/ajplegacy.1929.91.1.284

He, L., Vanlandewijck, M., Mäe, M. A., Andrae, J., Ando, K., Del Gaudio, F., Nahar, K., Lebouvier, T., Laviña, B., Gouveia, L., Sun, Y., Raschperger, E., Segerstolpe, Å., Liu, J., Gustafsson, S., Räsänen, M., Zarb, Y., Mochizuki, N., Keller, A., … Betsholtz, C. (2018). Single-cell RNA sequencing of mouse brain and lung vascular and vessel-associated cell types. *Scientific Data*, *5*(1), 180160. https://doi.org/10.1038/sdata.2018.160

Heimburg, T. (2012). The Capacitance and Electromechanical Coupling of Lipid Membranes Close to Transitions: The Effect of Electrostriction. *Biophysical Journal*, *103*(5), 918–929. https://doi.org/https://doi.org/10.1016/j.bpj.2012.07.010

Heinricher, M. M., & Ingram, S. L. (2008). *5.41 - The Brainstem and Nociceptive Modulation* (R. H. Masland, T. D. Albright, T. D. Albright, R. H. Masland, P. Dallos, D. Oertel, S. Firestein, G. K. Beauchamp, M. Catherine Bushnell, A. I. Basbaum, J. H. Kaas, & E. P. B. T.-T. S. A. C. R. Gardner (eds.); pp. 593–626). Academic Press. https://doi.org/https://doi.org/10.1016/B978-012370880-9.00183-3

Hellman, A., Maietta, T., Byraju, K., Linda Park, Y., Shao, M., Liss, A., Neubauer, P., Burdette, C., Ghoshal, G., Qian, J., Nalwalk, J., & Pilitsis, J. G. (2020). Low Intensity Focused Ultrasound Modulation of Vincristine Induced Neuropathy. *Neuroscience*, *430*, 82–93. https://doi.org/https://doi.org/10.1016/j.neuroscience.2020.01.021

Hellman, A., Maietta, T., Byraju, K., Park, Y. L., Liss, A., Prabhala, T., Neubauer, P., Williams, E., Burdette, C., Shin, D. S., Ghoshal, G., Nalwalk, J., Agrawal, A., Qian, J., & Pilitsis, J. (2020). Effects of external low intensity focused ultrasound on electrophysiological changes in vivo in a rodent model of common peroneal nerve injury. *Neuroscience*, *429*, 264–272. https://doi.org/https://doi.org/10.1016/j.neuroscience.2020.01.016

Hodgkin, A. L., & Huxley, A. F. (1952). A quantitative description of membrane current and its application to conduction and excitation in nerve. *The Journal of Physiology*, *117*(4), 500–544. https://doi.org/https://doi.org/10.1113/jphysiol.1952.sp004764

Hynynen, K., Mcdannold, N., Sheikov, N., Jolesz, F., & Vykhodtseva, N. (2005). Local and reversible blood-brain barrier disruption by noninvasive focused ultrasound at frequencies suitable for trans-skull sonications. *NeuroImage*, *24*, 12–20. https://doi.org/10.1016/j.neuroimage.2004.06.046

Ibsen, S., Tong, A., Schutt, C., Esener, S., & Chalasani, S. H. (2015). Sonogenetics is a non-invasive approach to activating neurons in Caenorhabditis elegans. *Nature Communications*, *6*(1), 8264. https://doi.org/10.1038/ncomms9264

Jäkel, S., & Dimou, L. (2017). Glial Cells and Their Function in the Adult Brain: A Journey through the History of Their Ablation. *Frontiers in Cellular Neuroscience*, *11*, 24. https://doi.org/10.3389/fncel.2017.00024

Jordão, J. F., Ayala-Grosso, C. A., Markham, K., Huang, Y., Chopra, R., McLaurin, J., Hynynen, K., & Aubert, I. (2010). Antibodies targeted to the brain with image-guided focused ultrasound reduces amyloid-beta plaque load in the TgCRND8 mouse model of Alzheimer's disease. *PloS One*, *5*(5), e10549. https://doi.org/10.1371/journal.pone.0010549

Kalucka, J., de Rooij, L. P. M. H., Goveia, J., Rohlenova, K., Dumas, S. J., Meta, E., Conchinha, N. V, Taverna, F., Teuwen, L.-A., Veys, K., García-Caballero, M., Khan, S., Geldhof, V., Sokol, L., Chen, R., Treps, L., Borri, M., de Zeeuw, P., Dubois, C., … Carmeliet, P. (2020). Single-Cell Transcriptome Atlas of Murine Endothelial Cells. *Cell*, *180*(4), 764-779.e20. https://doi.org/10.1016/j.cell.2020.01.015

Kamimura, H. A. S., Conti, A., Toschi, N., & Konofagou, E. E. (2020). Ultrasound neuromodulation: mechanisms and the potential of multimodal stimulation for neuronal function assessment. *Frontiers in Physics*, *8*, 150. https://doi.org/10.3389/fphy.2020.00150

Khraiche, M. L., Phillips, W. B., Jackson, N., & Muthuswamy, J. (2008). Ultrasound induced increase in excitability of single neurons. *Annual International Conference of the IEEE Engineering in Medicine and Biology Society. IEEE Engineering in Medicine and Biology Society. Annual International Conference*, *2008*, 4246–4249. https://doi.org/10.1109/iembs.2008.4650147

Kim, C. E., Kim, Y. K., Chung, G., Im, H. J., Lee, D. S., Kim, J., & Kim, S. J.

(2014). Identifying neuropathic pain using 18F-FDG micro-PET: A multivariate pattern analysis. *NeuroImage*, *86*, 311–316. https://doi.org/10.1016/j.neuroimage.2013.10.001

Kim, D., Langmead, B., & Salzberg, S. L. (2015). HISAT: a fast spliced aligner with low memory requirements. *Nature Methods*, *12*(4), 357–360. https://doi.org/10.1038/nmeth.3317

Kim, H.-B., Swanberg, K. M., Han, H.-S., Kim, J.-C., Kim, J.-W., Lee, S., Lee, C. J., Maeng, S., Kim, T.-S., & Park, J.-H. (2017). Prolonged stimulation with low-intensity ultrasound induces delayed increases in spontaneous hippocampal culture spiking activity. *Journal of Neuroscience Research*, *95*(3), 885–896. https://doi.org/https://doi.org/10.1002/jnr.23845

Kim, H., Park, M. Y., Lee, S. D., Lee, W., Chiu, A., & Yoo, S.-S. (2015). Suppression of EEG visual-evoked potentials in rats through neuromodulatory focused ultrasound. *Neuroreport*, *26*(4), 211–215. https://doi.org/10.1097/wnr.0000000000000330

King, R. L., Brown, J. R., Newsome, W. T., & Pauly, K. B. (2013). Effective Parameters for Ultrasound-Induced In Vivo Neurostimulation. *Ultrasound in Medicine & Biology*, *39*(2), 312–331. https://doi.org/https://doi.org/10.1016/j.ultrasmedbio.2012.09.009

Koroleva, V. I., Vykhodtseva, N. I., & Elagin, V. A. (1986). Cortical and subcortical spreading depression in rats produced by focused ultrasound. *Neurophysiology*, *18*(1), 43–48. https://doi.org/10.1007/BF01052490

Koynova, R., & Caffrey, M. (1995). Phases and phase transitions of the sphingolipids. *Biochimica et Biophysica Acta*, *1255*(3), 213–236. https://doi.org/10.1016/0005-2760(94)00202-a

Krasovitski, B., Frenkel, V., Shoham, S., & Kimmel, E. (2011). Intramembrane cavitation as a unifying mechanism for ultrasound-induced bioeffects. *Proceedings of the National Academy of Sciences of the United States of America*, *108*(8), 3258–3263. https://doi.org/10.1073/pnas.1015771108

Kubanek, J., Shi, J., Marsh, J., Chen, D., Deng, C., & Cui, J. (2016). Ultrasound modulates ion channel currents. *Scientific Reports*, *6*, 24170. https://doi.org/10.1038/srep24170

Kubanek, J., Shukla, P., Das, A., Baccus, S. A., & Goodman, M. B. (2018). Ultrasound Elicits Behavioral Responses through Mechanical Effects on Neurons and Ion Channels in a Simple Nervous System. *The Journal of Neuroscience : The Official Journal of the Society for Neuroscience*, *38*(12), 3081–3091. https://doi.org/10.1523/JNEUROSCI.1458-17.2018

Lee, W., Chung, Y. A., Jung, Y., Song, I.-U., & Yoo, S.-S. (2016). Simultaneous acoustic stimulation of human primary and secondary somatosensory cortices using transcranial focused ultrasound. *BMC Neuroscience*, *17*(1), 68. https://doi.org/10.1186/s12868-016-0303-6

Lee, W., Kim, H.-C., Jung, Y., Chung, Y. A., Song, I.-U., Lee, J.-H., & Yoo, S.-S. (2016). Transcranial focused ultrasound stimulation of human primary visual cortex. *Scientific Reports*, *6*(1), 34026. https://doi.org/10.1038/srep34026

Lee, W., Kim, H., Lee, S., Yoo, S.-S., & Chung, Y. A. (2014). Creation of various skin sensations using pulsed focused ultrasound: Evidence for functional neuromodulation. *International Journal of Imaging Systems and Technology*, *24*(2), 167–174. https://doi.org/https://doi.org/10.1002/ima.22091

Lee, W., Lee, S. D., Park, M. Y., Foley, L., Purcell-Estabrook, E., Kim, H., Fischer, K., Maeng, L.-S., & Yoo, S.-S. (2016). Image-Guided Focused Ultrasound-Mediated Regional Brain Stimulation in Sheep. *Ultrasound in Medicine & Biology*, *42*(2), 459–470. https://doi.org/https://doi.org/10.1016/j.ultrasmedbio.2015.10.001

Lee, Y.-F., Lin, C.-C., Cheng, J.-S., & Chen, G.-S. (2015). Nerve conduction block in diabetic rats using high-intensity focused ultrasound for analgesic applications. *British Journal of Anaesthesia*, *114*(5), 840–846. https://doi.org/10.1093/bja/aeu443

Leger, M., Quiedeville, A., Bouet, V., Haelewyn, B., Boulouard, M., Schumann-Bard, P., & Freret, T. (2013). Object recognition test in mice. *Nature Protocols*, *8*(12), 2531–2537. https://doi.org/10.1038/nprot.2013.155

Legon, W., Ai, L., Bansal, P., & Mueller, J. K. (2018). Neuromodulation with single-element transcranial focused ultrasound in human thalamus. *Human Brain Mapping*, *39*(5), 1995–2006. https://doi.org/https://doi.org/10.1002/hbm.23981

Legon, W., Bansal, P., Tyshynsky, R., Ai, L., & Mueller, J. K. (2018). Transcranial focused ultrasound neuromodulation of the human primary motor cortex. *Scientific Reports*, *8*(1), 10007. https://doi.org/10.1038/s41598-018-28320-1

Legon, W., Rowlands, A., Opitz, A., Sato, T. F., & Tyler, W. J. (2012). Pulsed ultrasound differentially stimulates somatosensory circuits in humans as indicated by EEG and FMRI. *PloS One*, *7*(12), e51177. https://doi.org/10.1371/journal.pone.0051177

Legon, W., Sato, T. F., Opitz, A., Mueller, J., Barbour, A., Williams, A., & Tyler, W. J. (2014). Transcranial focused ultrasound modulates the activity of primary somatosensory cortex in humans. *Nature Neuroscience*, *17*(2), 322–329. https://doi.org/10.1038/nn.3620

Lei, L. G., Zhang, Y. Q., & Zhao, Z. Q. (2004). Pain-related aversion and Fos expression in the central nervous system in rats. *NeuroReport*, *15*(1), 67–71. https://doi.org/10.1097/00001756-200401190-00014

Lele, P. P. (1963). Effects of focused ultrasonic radiation on peripheral nerve, with observations on local heating. *Experimental Neurology*, *8*(1), 47–83. https://doi.org/https://doi.org/10.1016/0014-4886(63)90008-6

Li, G.-F., Zhao, H.-X., Zhou, H., Yan, F., Wang, J.-Y., Xu, C.-X., Wang, C.-Z., Niu, L.-L., Meng, L., Wu, S., Zhang, H.-L., Qiu, W.-B., & Zheng, H.-R. (2016). Improved Anatomical Specificity of Non-invasive Neuro-stimulation by High Frequency (5 MHz) Ultrasound. *Scientific Reports*, *6*, 24738. https://doi.org/10.1038/srep24738

Li, G., Qiu, W., Zhang, Z., Jiang, Q., Su, M., Cai, R., Li, Y., Cai, F., Deng, Z., Xu, D., Zhang, H., & Zheng, H. (2019). Noninvasive Ultrasonic Neuromodulation in Freely Moving Mice. *IEEE Transactions on Bio-Medical Engineering*, *66*(1), 217–224. https://doi.org/10.1109/tbme.2018.2821201

Li, Q., Cheng, Z., Zhou, L., Darmanis, S., Neff, N. F., Okamoto, J., Gulati, G., Bennett, M. L., Sun, L. O., Clarke, L. E., Marschallinger, J., Yu, G., Quake, S. R., Wyss-Coray, T., & Barres, B. A. (2019). Developmental Heterogeneity of Microglia and Brain Myeloid Cells Revealed by Deep Single-Cell RNA Sequencing. *Neuron*, *101*(2), 207-223.e10. https://doi.org/10.1016/j.neuron.2018.12.006

Liao, D., Li, F., Lu, D., & Zhong, P. (2019). Activation of Piezo1 mechanosensitive ion channel in HEK293T cells by 30 MHz vertically deployed surface acoustic waves. *Biochemical and Biophysical Research Communications*, *518*(3), 541–547. https://doi.org/https://doi.org/10.1016/j.bbrc.2019.08.078

Lipsman, N., Meng, Y., Bethune, A. J., Huang, Y., Lam, B., Masellis, M., Herrmann, N., Heyn, C., Aubert, I., Boutet, A., Smith, G. S., Hynynen, K., & Black, S. E. (2018). Blood-brain barrier opening in Alzheimer's disease using MR-guided focused ultrasound. *Nature Communications*, *9*(1), 2336. https://doi.org/10.1038/s41467-018-04529-6

Liss, A., Hellman, A., Patel, V. J., Maietta, T., Byraju, K., Trowbridge, R., Acheta, J., Panse, D., Srikanthan, A., Neubauer, P., Burdette, C., Ghoshal, G., Williams, E., Qian, J., & Pilitsis, J. G. (2021). Low Intensity Focused Ultrasound Increases Duration of Anti-Nociceptive Responses in Female Common Peroneal Nerve Injury Rats. *Neuromodulation: Technology at the Neural Interface*, *n/a*(n/a). https://doi.org/https://doi.org/10.1111/ner.13531

Livak, K. J., & Schmittgen, T. D. (2001). Analysis of relative gene expression data using real-time quantitative PCR and the 2(-Delta Delta C(T)) Method. *Methods (San Diego, Calif.)*, *25*(4), 402–408. https://doi.org/10.1006/meth.2001.1262

Marques, S., Zeisel, A., Codeluppi, S., van Bruggen, D., Mendanha Falcão, A., Xiao, L., Li, H., Häring, M., Hochgerner, H., Romanov, R. A., Gyllborg, D., Muñoz-Manchado, A. B., La Manno, G., Lönnerberg, P., Floriddia, E. M., Rezayee, F., Ernfors, P., Arenas, E., Hjerling-Leffler, J., … Castelo-Branco,

G. (2016). Oligodendrocyte heterogeneity in the mouse juvenile and adult central nervous system. *Science*, *352*(6291), 1326 LP – 1329. https://doi.org/10.1126/science.aaf6463

Martin, E., Werner, B., Bauer, R., van Leyen, K., Coluccia, D., & Fandino, J. (2014). Clinical neurological HIFU applications: the Zurich experience. *Translational Cancer Research; Vol 3, No 5 (October 2014): Translational Cancer Research (High Intensity Focused Ultrasounds)*. https://tcr.amegroups.com/article/view/3156

MAZOUE, H., CHAUCHARD, P., & BUSNEL, R. G. (1953). [Nervous excitation with high frequency ultrasonics]. *Journal de physiologie*, *45*(1), 179–182. http://europepmc.org/abstract/MED/13062179

Meacham, K., Shepherd, A., Mohapatra, D. P., & Haroutounian, S. (2017). Neuropathic Pain: Central vs. Peripheral Mechanisms. *Current Pain and Headache Reports*, *21*(6), 28. https://doi.org/10.1007/s11916-017-0629-5

Meldrum, B. S., Akbar, M. T., & Chapman, A. G. (1999). Glutamate receptors and transporters in genetic and acquired models of epilepsy. *Epilepsy Research*, *36*(2), 189–204. https://doi.org/https://doi.org/10.1016/S0920-1211(99)00051-0

Meneghetti, N., Dedola, F., Gavryusev, V., Sancataldo, G., Turrini, L., de Vito, G., Tiso, N., Vanzi, F., Carpaneto, J., Cutrone, A., Pavone, F. S., Micera, S., & Mazzoni, A. (2020). Direct activation of zebrafish neurons by ultrasonic stimulation revealed by whole CNS calcium imaging. *Journal of Neural Engineering*, *17*(5), 56033. https://doi.org/10.1088/1741-2552/abae8b

Mihran, R. T., Barnes, F. S., & Wachtel, H. (1990). Temporally-specific modification of myelinated axon excitability in vitro following a single ultrasound pulse. *Ultrasound in Medicine & Biology*, *16*(3), 297–309. https://doi.org/https://doi.org/10.1016/0301-5629(90)90008-Z

Miller, M., Shi, J., Zhu, Y., Kustov, M., Tian, J., Stevens, A., Wu, M., Xu, J., Long, S., Yang, P., Zholos, A. V, Salovich, J. M., Weaver, C. D., Hopkins, C. R., Lindsley, C. W., McManus, O., Li, M., & Zhu, M. X. (2011). Identification of ML204, a novel potent antagonist that selectively modulates native TRPC4/C5 ion channels. *The Journal of Biological Chemistry*, *286*(38), 33436–33446. https://doi.org/10.1074/jbc.M111.274167

Mohammadjavadi, M., Ye, P. P., Xia, A., Brown, J., Popelka, G., & Pauly, K. B. (2019). Elimination of peripheral auditory pathway activation does not affect motor responses from ultrasound neuromodulation. *Brain Stimulation*, *12*(4), 901–910. https://doi.org/https://doi.org/10.1016/j.brs.2019.03.005

Moore, M. E., Loft, J. M., Clegern, W. C., & Wisor, J. P. (2015). Manipulating neuronal activity in the mouse brain with ultrasound: A comparison with optogenetic activation of the cerebral cortex. *Neuroscience Letters*, *604*, 183–187. https://doi.org/https://doi.org/10.1016/j.neulet.2015.07.024

Morris, C. E. (2011). Voltage-gated channel mechanosensitivity: fact or friction? *Frontiers in Physiology*, *2*, 25. https://doi.org/10.3389/fphys.2011.00025

Mosgaard, L. D., Zecchi, K. A., & Heimburg, T. (2015). Mechano-capacitive properties of polarized membranes. *Soft Matter*, *11*(40), 7899–7910. https://doi.org/10.1039/c5sm01519g

Mueller, J., Legon, W., Opitz, A., Sato, T. F., & Tyler, W. J. (2014). Transcranial Focused Ultrasound Modulates Intrinsic and Evoked EEG Dynamics. *Brain Stimulation*, *7*(6), 900–908. https://doi.org/https://doi.org/10.1016/j.brs.2014.08.008

Nitsche, M. A., Cohen, L. G., Wassermann, E. M., Priori, A., Lang, N., Antal, A., Paulus, W., Hummel, F., Boggio, P. S., Fregni, F., & Pascual-Leone, A. (2008). Transcranial direct current stimulation: State of the art 2008. *Brain Stimulation*, *1*(3), 206–223. https://doi.org/https://doi.org/10.1016/j.brs.2008.06.004

O’Brien, W. D. (2007). Ultrasound–biophysics mechanisms. *Progress in Biophysics and Molecular Biology*, *93*(1), 212–255. https://doi.org/https://doi.org/10.1016/j.pbiomolbio.2006.07.010

Oh, S.-J., Lee, J. M., Kim, H.-B., Lee, J., Han, S., Bae, J. Y., Hong, G.-S., Koh, W., Kwon, J., Hwang, E.-S., Woo, D. H., Youn, I., Cho, I.-J., Bae, Y. C., Lee, S., Shim, J. W., Park, J.-H., & Lee, C. J. (2019). Ultrasonic Neuromodulation via Astrocytic TRPA1. *Current Biology*, *29*(20), 3386-3401.e8. https://doi.org/https://doi.org/10.1016/j.cub.2019.08.021

Paulson, P. E., Morrow, T. J., & Casey, K. L. (2000). Bilateral behavioral and regional cerebral blood flow changes during painful peripheral mononeuropathy in the rat. *Pain*, *84*(2–3), 233–245. https://doi.org/10.1016/S0304-3959(99)00216-X

Perlmutter, J. S., & Mink, J. W. (2006). DEEP BRAIN STIMULATION. *Annual Review of Neuroscience*, *29*(1), 229–257. https://doi.org/10.1146/annurev.neuro.29.051605.112824

Perozo, E., Kloda, A., Cortes, D. M., & Martinac, B. (2002). Physical principles underlying the transduction of bilayer deformation forces during mechanosensitive channel gating. *Nature Structural Biology*, *9*(9), 696–703. https://doi.org/10.1038/nsb827

Pertea, M., Pertea, G. M., Antonescu, C. M., Chang, T.-C., Mendell, J. T., & Salzberg, S. L. (2015). StringTie enables improved reconstruction of a transcriptome from RNA-seq reads. *Nature Biotechnology*, *33*(3), 290–295. https://doi.org/10.1038/nbt.3122

Petrov, A. G. (2002). Flexoelectricity of model and living membranes. *Biochimica et Biophysica Acta (BBA) - Biomembranes*, *1561*(1), 1–25.

https://doi.org/https://doi.org/10.1016/S0304-4157(01)00007-7

Plaksin, M., Shoham, S., & Kimmel, E. (2014). Intramembrane Cavitation as a Predictive Bio-Piezoelectric Mechanism for Ultrasonic Brain Stimulation. *Physical Review X*, *4*(1), 11004. https://doi.org/10.1103/PhysRevX.4.011004

Prabhala, T., Hellman, A., Walling, I., Maietta, T., Qian, J., Burdette, C., Neubauer, P., Shao, M., Stapleton, A., Thibodeau, J., & Pilitsis, J. G. (2018). External focused ultrasound treatment for neuropathic pain induced by common peroneal nerve injury. *Neuroscience Letters*, *684*, 145–151. https://doi.org/10.1016/j.neulet.2018.07.037

Prieto, M. L., Firouzi, K., Khuri-Yakub, B. T., & Maduke, M. (2018). Activation of Piezo1 but Not Na(V)1.2 Channels by Ultrasound at 43 MHz. *Ultrasound in Medicine & Biology*, *44*(6), 1217–1232. https://doi.org/10.1016/j.ultrasmedbio.2017.12.020

Prieto, M. L., Ömer, O., Khuri-Yakub, B. T., & Maduke, M. C. (2013). Dynamic response of model lipid membranes to ultrasonic radiation force. *PloS One*, *8*(10), e77115. https://doi.org/10.1371/journal.pone.0077115

Qiu, W., Zhou, J., Chen, Y., Su, M., Li, G., Zhao, H., Gu, X., Meng, D., Wang, C., Xiao, Y., Lam, K. H., Dai, J., & Zheng, H. (2017). A Portable Ultrasound System for Non-Invasive Ultrasonic Neuro-Stimulation. *IEEE Transactions on Neural Systems and Rehabilitation Engineering*, *25*(12), 2509–2515. https://doi.org/10.1109/TNSRE.2017.2765001

Quintero, G. C. (2013). Advances in cortical modulation of pain. *Journal of Pain Research*, *6*, 713–725. https://doi.org/10.2147/JPR.S45958

Renier, N., Adams, E. L., Kirst, C., Wu, Z., Azevedo, R., Kohl, J., Autry, A. E., Kadiri, L., Umadevi Venkataraju, K., Zhou, Y., Wang, V. X., Tang, C. Y., Olsen, O., Dulac, C., Osten, P., & Tessier-Lavigne, M. (2016). Mapping of Brain Activity by Automated Volume Analysis of Immediate Early Genes. *Cell*, *165*(7), 1789–1802. https://doi.org/https://doi.org/10.1016/j.cell.2016.05.007

Rinaldi, P. C., Jones, J. P., Reines, F., & Price, L. R. (1991). Modification by focused ultrasound pulses of electrically evoked responses from an in vitro hippocampal preparation. *Brain Research*, *558*(1), 36–42. https://doi.org/https://doi.org/10.1016/0006-8993(91)90711-4

Robinson, M. D., McCarthy, D. J., & Smyth, G. K. (2010). edgeR: a Bioconductor package for differential expression analysis of digital gene expression data. *Bioinformatics (Oxford, England)*, *26*(1), 139–140. https://doi.org/10.1093/bioinformatics/btp616

Samiotaki, G., Acosta, C., Wang, S., & Konofagou, E. E. (2015). Enhanced delivery and bioactivity of the neurturin neurotrophic factor through focused ultrasound-mediated blood--brain barrier opening in vivo. *Journal* *of Cerebral Blood Flow and Metabolism : Official Journal of the International Society of Cerebral Blood Flow and Metabolism*, *35*(4), 611–622. https://doi.org/10.1038/jcbfm.2014.236

Sato, T., Shapiro, M. G., & Tsao, D. Y. (2018). Ultrasonic Neuromodulation Causes Widespread Cortical Activation via an Indirect Auditory Mechanism. *Neuron*, *98*(5), 1031-1041.e5. https://doi.org/https://doi.org/10.1016/j.neuron.2018.05.009

Scarcelli, T., Jordão, J. F., O'Reilly, M. A., Ellens, N., Hynynen, K., & Aubert, I. (2014). Stimulation of Hippocampal Neurogenesis by Transcranial Focused Ultrasound and Microbubbles in Adult Mice. *Brain Stimulation*, *7*(2), 304–307. https://doi.org/https://doi.org/10.1016/j.brs.2013.12.012

Seeger, H. M., Aldrovandi, L., Alessandrini, A., & Facci, P. (2010). Changes in single K(+) channel behavior induced by a lipid phase transition. *Biophysical Journal*, *99*(11), 3675–3683. https://doi.org/10.1016/j.bpj.2010.10.042

Shapiro, M. G., Homma, K., Villarreal, S., Richter, C.-P., & Bezanilla, F. (2012). Infrared light excites cells by changing their electrical capacitance. *Nature Communications*, *3*, 736. https://doi.org/10.1038/ncomms1742

Shapiro, M. G., Homma, K., Villarreal, S., Richter, C.-P., & Bezanilla, F. (2017). Correspondence: Reply to 'Revisiting the theoretical cell membrane thermal capacitance response.' *Nature Communications*, *8*(1), 1432. https://doi.org/10.1038/s41467-017-00436-4

Shimizu, T., Fujita, N., Tsuji-Tamura, K., Kitagawa, Y., Fujisawa, T., Tamura, M., & Sato, M. (2021). Osteocytes as main responders to low-intensity pulsed ultrasound treatment during fracture healing. *Scientific Reports*, *11*(1), 10298. https://doi.org/10.1038/s41598-021-89672-9

Sikes, R. W., Vogt, L. J., & Vogt, B. A. (2008). Distribution and properties of visceral nociceptive neurons in rabbit cingulate cortex. *PAIN®*, *135*(1), 160–174. https://doi.org/https://doi.org/10.1016/j.pain.2007.09.024

Subramanian, A., Tamayo, P., Mootha, V. K., Mukherjee, S., Ebert, B. L., Gillette, M. A., Paulovich, A., Pomeroy, S. L., Golub, T. R., Lander, E. S., & Mesirov, J. P. (2005). Gene set enrichment analysis: a knowledge-based approach for interpreting genome-wide expression profiles. *Proceedings of the National Academy of Sciences of the United States of America*, *102*(43), 15545–15550. https://doi.org/10.1073/pnas.0506580102

TAKAGI, S. F., HIGASHINO, S., SHIBUYA, T., & OSAWA, N. (1960). The actions of ultrasound on the myelinated nerve, the spinal cord and the brain. *The Japanese Journal of Physiology*, *10*, 183–193. https://doi.org/10.2170/jjphysiol.10.183

Tata, D. B., & Dunn, F. (1992). Interaction of ultrasound and model membrane systems: analyses and predictions. *The Journal of Physical Chemistry*, *96*(8), 3548–3555. https://doi.org/10.1021/j100187a067

Taylor, G. J., Heberle, F. A., Seinfeld, J. S., Katsaras, J., Collier, C. P., & Sarles, S. A. (2017). Capacitive Detection of Low-Enthalpy, Higher-Order Phase Transitions in Synthetic and Natural Composition Lipid Membranes. *Langmuir : The ACS Journal of Surfaces and Colloids*, *33*(38), 10016–10026. https://doi.org/10.1021/acs.langmuir.7b02022

Treat, L. H., McDannold, N., Vykhodtseva, N., Zhang, Y., Tam, K., & Hynynen, K. (2007). Targeted delivery of doxorubicin to the rat brain at therapeutic levels using MRI-guided focused ultrasound. *International Journal of Cancer*, *121*(4), 901–907. https://doi.org/https://doi.org/10.1002/ijc.22732

Tsui, P.-H., Wang, S.-H., & Huang, C.-C. (2005). In vitro effects of ultrasound with different energies on the conduction properties of neural tissue. *Ultrasonics*, *43*(7), 560–565. https://doi.org/https://doi.org/10.1016/j.ultras.2004.12.003

Tufail, Y., Matyushov, A., Baldwin, N., Tauchmann, M. L., Georges, J., Yoshihiro, A., Tillery, S. I. H., & Tyler, W. J. (2010). Transcranial pulsed ultrasound stimulates intact brain circuits. *Neuron*, *66*(5), 681–694. https://doi.org/10.1016/j.neuron.2010.05.008

Tyler, W. J., Tufail, Y., Finsterwald, M., Tauchmann, M. L., Olson, E. J., & Majestic, C. (2008). Remote Excitation of Neuronal Circuits Using Low-Intensity, Low-Frequency Ultrasound. *PLOS ONE*, *3*(10), e3511. https://doi.org/10.1371/journal.pone.0003511

Vadakkan, K. I., Jia, Y. H., & Zhuo, M. (2005). A Behavioral Model of Neuropathic Pain Induced by Ligation of the Common Peroneal Nerve in Mice. *The Journal of Pain*, *6*(11), 747–756. https://doi.org/https://doi.org/10.1016/j.jpain.2005.07.005

van Groen, T, & Wyss, J. M. (1990). Connections of the retrosplenial granular a cortex in the rat. *The Journal of Comparative Neurology*, *300*(4), 593–606. https://doi.org/10.1002/cne.903000412

van Groen, Thomas, & Wyss, J. M. (1992). Connections of the retrosplenial dysgranular cortex in the rat. *Journal of Comparative Neurology*, *315*(2), 200–216. https://doi.org/https://doi.org/10.1002/cne.903150207

Van Groen, Thomas, & Wyss, J. M. (2003). Connections of the retrosplenial granular b cortex in the rat. *Journal of Comparative Neurology*, *463*(3), 249–263. https://doi.org/https://doi.org/10.1002/cne.10757

Vanlandewijck, M., He, L., Mäe, M. A., Andrae, J., Ando, K., Del Gaudio, F., Nahar, K., Lebouvier, T., Laviña, B., Gouveia, L., Sun, Y., Raschperger, E., Räsänen, M., Zarb, Y., Mochizuki, N., Keller, A., Lendahl, U., & Betsholtz, C. (2018). A molecular atlas of cell types and zonation in the brain vasculature. *Nature*, *554*(7693), 475–480. https://doi.org/10.1038/nature25739

Vazquez, G., Wedel, B. J., Aziz, O., Trebak, M., & Putney, J. W. J. (2004). The mammalian TRPC cation channels. *Biochimica et Biophysica Acta*, *1742*(1–3), 21–36. https://doi.org/10.1016/j.bbamcr.2004.08.015

Vogt, B. A. (2019). The cingulate cortex in neurologic diseases: History, Structure, Overview. *Handbook of Clinical Neurology*, *166*, 3–21. https://doi.org/10.1016/B978-0-444-64196-0.00001-7

Wahab, R. A., Choi, M., Liu, Y., Krauthamer, V., Zderic, V., & Myers, M. R. (2012). Mechanical bioeffects of pulsed high intensity focused ultrasound on a simple neural model. *Medical Physics*, *39*(7Part1), 4274–4283. https://doi.org/https://doi.org/10.1118/1.4729712

Wang, J.-H., Wu, C., Lian, Y.-N., Liu, L., Chen, W., Chen, W., Zhang, Z., Zhuo, M., & Li, X.-Y. (2021). Single-cell RNA sequencing uncovers the excitatory/inhibitory synaptic unbalance in the retrosplenial cortex after peripheral nerve injury. *BioRxiv*, 2021.06.09.444962. https://doi.org/10.1101/2021.06.09.444962

Wang, T. R., Dallapiazza, R., & Elias, W. J. (2015). Neurological applications of transcranial high intensity focused ultrasound. *International Journal of Hyperthermia*, *31*(3), 285–291. https://doi.org/10.3109/02656736.2015.1007398

Wang, Y.-J., Liu, M.-G., Wang, J.-H., Cao, W., Wu, C., Wang, Z.-Y., Liu, L., Yang, F., Feng, Z.-H., Sun, L., Zhang, F., Shen, Y., Zhou, Y.-D., Zhuo, M., Luo, J.-H., Xu, T.-L., & Li, X.-Y. (2020). Restoration of Cingulate Long-Term Depression by Enhancing Non-apoptotic Caspase 3 Alleviates Peripheral Pain Hypersensitivity. *Cell Reports*, *33*(6), 108369. https://doi.org/https://doi.org/10.1016/j.celrep.2020.108369

Wattiez, N., Constans, C., Deffieux, T., Daye, P. M., Tanter, M., Aubry, J.-F., & Pouget, P. (2017). Transcranial ultrasonic stimulation modulates single-neuron discharge in macaques performing an antisaccade task. *Brain Stimulation*, *10*(6), 1024–1031. https://doi.org/https://doi.org/10.1016/j.brs.2017.07.007

Wells, J., Kao, C., Konrad, P., Milner, T., Kim, J., Mahadevan-Jansen, A., & Jansen, E. D. (2007). Biophysical mechanisms of transient optical stimulation of peripheral nerve. *Biophysical Journal*, *93*(7), 2567–2580. https://doi.org/10.1529/biophysj.107.104786

Wunderlich, B., Leirer, C., Idzko, A.-L., Keyser, U. F., Wixforth, A., Myles, V. M., Heimburg, T., & Schneider, M. F. (2009). Phase-state dependent current fluctuations in pure lipid membranes. *Biophysical Journal*, *96*(11), 4592–4597. https://doi.org/10.1016/j.bpj.2009.02.053

Ximerakis, M., Lipnick, S. L., Innes, B. T., Simmons, S. K., Adiconis, X., Dionne, D., Mayweather, B. A., Nguyen, L., Niziolek, Z., Ozek, C., Butty, V. L., Isserlin, R., Buchanan, S. M., Levine, S. S., Regev, A., Bader, G. D., Levin,

J. Z., & Rubin, L. L. (2019). Single-cell transcriptomic profiling of the aging mouse brain. *Nature Neuroscience*, *22*(10), 1696–1708. https://doi.org/10.1038/s41593-019-0491-3

Yang, L., & Kindt, J. T. (2015). Simulation study of the permeability of a model lipid membrane at the fluid-solid phase transition. *Langmuir : The ACS Journal of Surfaces and Colloids*, *31*(7), 2187–2195. https://doi.org/10.1021/la504269t

Yang, P.-F., Phipps, M. A., Newton, A. T., Chaplin, V., Gore, J. C., Caskey, C. F., & Chen, L. M. (2018). Neuromodulation of sensory networks in monkey brain by focused ultrasound with MRI guidance and detection. *Scientific Reports*, *8*(1), 7993. https://doi.org/10.1038/s41598-018-26287-7

Transcranial focused ultrasound to the thalamus is associated with reduced extracellular GABA levels in rats., 65 Neuropsychobiology 153 (2012). https://doi.org/10.1159/000336001

Ye, J., Tang, S., Meng, L., Li, X., Wen, X., Chen, S., Niu, L., Li, X., Qiu, W., Hu, H., Jiang, M., Shang, S., Shu, Q., Zheng, H., Duan, S., & Li, Y. (2018). Ultrasonic Control of Neural Activity through Activation of the Mechanosensitive Channel MscL. *Nano Letters*, *18*(7), 4148–4155. https://doi.org/10.1021/acs.nanolett.8b00935

Ye, P. P., Brown, J. R., & Pauly, K. B. (2016). Frequency Dependence of Ultrasound Neurostimulation in the Mouse Brain. *Ultrasound in Medicine & Biology*, *42*(7), 1512–1530. https://doi.org/10.1016/j.ultrasmedbio.2016.02.012

Yoo, S.-S., Bystritsky, A., Lee, J.-H., Zhang, Y., Fischer, K., Min, B.-K., McDannold, N. J., Pascual-Leone, A., & Jolesz, F. A. (2011). Focused ultrasound modulates region-specific brain activity. *NeuroImage*, *56*(3), 1267–1275. https://doi.org/10.1016/j.neuroimage.2011.02.058

Yoo, S., Mittelstein, D. R., Hurt, R. C., Lacroix, J., & Shapiro, M. G. (2022). Focused ultrasound excites cortical neurons via mechanosensitive calcium accumulation and ion channel amplification. *Nature Communications*, *13*(1), 493. https://doi.org/10.1038/s41467-022-28040-1

YOUNG, R. R., & HENNEMAN, E. (1961). Functional effects of focused ultrasound on mammalian nerves. *Science (New York, N.Y.)*, *134*(3489), 1521–1522. https://doi.org/10.1126/science.134.3489.1521

Zeisel, A., Hochgerner, H., Lönnerberg, P., Johnsson, A., Memic, F., van der Zwan, J., Häring, M., Braun, E., Borm, L. E., La Manno, G., Codeluppi, S., Furlan, A., Lee, K., Skene, N., Harris, K. D., Hjerling-Leffler, J., Arenas, E., Ernfors, P., Marklund, U., & Linnarsson, S. (2018). Molecular Architecture of the Mouse Nervous System. *Cell*, *174*(4), 999-1014.e22. https://doi.org/https://doi.org/10.1016/j.cell.2018.06.021

Zhou, W., Wang, X., Wang, K., Farooq, U., Kang, L., Niu, L., & Meng, L. (2022).

Ultrasound Activation of Mechanosensory Ion Channels in Caenorhabditis Elegans. *IEEE Transactions on Ultrasonics, Ferroelectrics, and Frequency Control*, *69*(2), 473–479. https://doi.org/10.1109/TUFFC.2021.3120750